Surface polarization profile and structural dynamics of ferroelectric thin films

Dissertation
zur Erlangung des Doktorgrades
der Mathematisch-Naturwissenschaftlichen Fakultät
der Christian-Albrechts-Universität zu Kiel

vorgelegt von

Le Phuong Hoang

aus Danang, Vietnam

Kiel

2024

Surface polarization profile and structural dynamics of ferroelectric thin films

Dissertation
zur Erlangung des Doktorgrades
der Mathematisch-Naturwissenschaftlichen Fakultät
der Christian-Albrechts-Universität zu Kiel

vorgelegt von

Le Phuong Hoang

aus Danang, Vietnam

Kiel

2024

Erster Gutachter:	Prof. Dr. Kai Rossnagel
Zweiter Gutachter:	Prof. Dr. Olaf Magnussen
Tag der mündlichen Prüfung:	29th October 2024

To my families

Declaration

I declare that the thesis entitled *"Surface polarization profile and structural dynamics of ferroelectric thin films"* is my original research work, conducted at the European XFEL, Max-Planck-Institute for the Structure and Dynamics of Matter, and the Institute of Experimental and Applied Physics at Kiel University, Germany, under the guidance and supervision of Prof. Dr. Kai Rossnagel, Dr. Andreas Scherz, and Dr. Giuseppe Mercurio.

I further affirm that this thesis has not been submitted, either in part or in full, by me for any degree or diploma at any other university. The thesis has neither been published nor submitted for publication. It has been prepared in accordance with the Rules of Good Scientific Practice established by the German Research Foundation. All sources and materials used have been acknowledged and specified. An academic degree has never been rescinded. The submitted electronic copy is identical to the print version.

Kiel, 2024 Le Phuong Hoang

Acknowledgements

Doctoral studies represent a significant journey in becoming a scientist. This journey involves not only solving scientific problems but also interacting with many people from diverse backgrounds. I am deeply grateful for the support and encouragement I received from so many individuals. Without their immense dedication, this work would not have been possible.

First and foremost, I want to express my profound gratitude to my direct supervisor, Dr. Giuseppe Mercurio, who provided me with the opportunity to work on this fascinating research topic. He introduced me to synchrotron and free-electron laser-based experiments and continuously encouraged me to question and critically evaluate my work. This has helped make my results more robust and convincing. Additionally, his insistence on presenting my work comprehensively has been invaluable for my development as a future lecturer. His support extended beyond academic guidance; he was also present during lab-based laser experiments and offered unwavering support both academically and personally. I will always remember his kindness in driving me home during freezing midnights after our experiments. I feel extraordinarily fortunate and grateful to have him as my doctoral supervisor.

I would like to thank Dr. Andreas Scherz for giving me the opportunity to be a member of SCS. The insightful discussions and suggestions during monthly and science meetings provided me with numerous creative ideas to overcome my challenges. The social gatherings he organized also helped me relax after stressful periods of work.

I am grateful to Prof. Dr. Kai Rossnagel for being my academic supervisor. His knowledge has expanded my horizons and enriched my scientific creativity. His constant support for my graduation and application recommendations has been invaluable.

My thanks go to my colleagues Dr. Robert Carley, Dr. Laurent Mercadier, and Dr. Martin Teichmann, as well as Laser Group members Dr. Man Jiang and Dr. Jinxiong Wang, for their essential assistance while I established my optical second harmonic generation setup from scratch, including optics and

controlling software.

I would also like to acknowledge the collaborators in Spain—Dr. Irena Spasojevic, Dr. David Pesquera, Dr. Saptam Ganguly, and Prof. Dr. Gustau Catalan—for providing excellent $BaTiO_3$ thin film samples, their sample characterization, and the fruitful discussions we had regarding our results.

My gratitude extends to the collaborators at the Diamond Light Source facility—Dr. Tien-Lin Lee and Dr. Jörg Zegenhagen—for their support during the beamtime at the Diamond Light Source and the European XFEL, as well as for the discussions of the results.

I also want to thank all collaborators from DESY, Prof. Dr. Ivan Vartanyants and Dr. Gerard Hinsley, for their focused efforts during our beamtime at the European XFEL and for participating in the discussions of the results. Your dedication was crucial for the success of the beamtime.

I would like to thank all my SCS colleagues who accompanied me throughout my Ph.D.: Nahid, Luigi, Sergii, Alexander, Jan Torben, Carsten, Justine, Natalia, Laurent, Ben, Löic, Giacomo, Teguh, Young Yong, and Zhong. It has been a great pleasure working with all of you. I would especially like to extend my deepest gratitude to Nahid, who not only supported my work but also provided invaluable guidance in child care, which has been immensely beneficial for my family life in a foreign country.

I have been fortunate to be associated with several prestigious institutions, including European XFEL, IMPRS-UFAST, DESY, and Kiel University. I firmly believe that the research facilities and support services at these institutions are among the best in the world. The talented colleagues across the field of ultrafast spectroscopy have provided invaluable experiences through PhD seminars, Science and Student days, and shared academic and daily life experiences. I would like to thank Ms. Neda Lotfiomran for her administrative support at IMPRS-UFAST and the members of the DESY international office for their assistance with accommodation, resident permit extensions, and other administrative procedures in Hamburg.

Finally, I extend my heartfelt thanks to my family. My parents, who have always trusted and supported me, provide me with endless love and encouragement. My younger brother's care and my parents-in-law's continuous encouragement have been a source of strength. My wife, who has been with me every day, has given me precious moments and the strength to overcome challenges in both research and life. My son, whom I love dearly, is my main source of positive energy. I am deeply grateful to my family for their love and

support, which has been essential to all my successes.

Abstract

Ferroelectric materials have attracted considerable scientific attention because of their switchable polarization, ferroelasticity, piezoelectricity, and pyroelectricity, which are crucial for numerous technological applications including ferroelectric transistors, photovoltaic cells, and photostrictive actuators. The prototypical ferroelectric material, $BaTiO_3$, exhibits a spontaneous polarization resulting from the relative displacement of cations and anions within its unit cell. The strain gradient in a ferroelectric thin film, resulting from the lattice mismatch with the substrate on which it is epitaxially grown, makes the interaction between lattice structure and spontaneous polarization a fascinating and important topic for both fundamental research and practical applications. This thesis is dedicated to employing spectroscopic techniques to probe the lattice structure and spontaneous polarization profile of strained ferroelectric thin films, both at equilibrium and under above-bandgap optical excitation.

At equilibrium, the ferroelectric polarization state can be stabilized through surface charge compensation, which can cause significant differences between the surface and bulk ferroelectric polarization in terms of amplitude and orientation. Understanding the mechanisms behind a stable surface polarization in ferroelectric thin films is crucial for actively controlling the surface polarization itself. X-ray standing waves and photoelectron spectroscopy are employed here to map the near-surface polarization profile of differently strained $BaTiO_3$ thin films. This information elucidates how bulk polarization, as well as the type, amount, and spatial distribution of surface adsorbates, affects the amplitude and orientation of local ferroelectric polarization near the surface.

We employ above-bandgap excitation to transiently modify both electronic and lattice structures in a $BaTiO_3$ thin film. Understanding how intense optical pulses perturb the electron distribution and the resulting lattice deformation provides a means of controlling at ultrafast timescales both strain and ferroelectric polarization. To achieve this, time-resolved X-ray diffraction, second harmonic generation, and optical reflectance are combined to investigate the dynamics of lattice structure and ferroelectric polarization upon absorption

of above-bandgap optical pulses. Time-resolved X-ray diffraction monitors transient lattice modifications and measures the average strain achieved at different laser fluences. To model our data, we combine two-temperature model and one-dimensional strain wave equation. We see that the maximum average strain of the ferroelectric thin film can be controlled by varying the incident laser fluence and the film thickness. In addition, by controlling the fluence, we can reach up to 30 % reversible change of the ferroelectric polarization, and fine tune the relaxation times of both photoexcited carriers and spontaneous polarization. The different dynamics observed in the nonlinear optical susceptibility tensor elements upon optical excitation suggests a non-thermal transient symmetry change in our sample. This is attributed to the highly directional light-induced polarization instability, predicted also by theory. Finally, our data show that the photoinduced variations of the ferroelectric polarization are the result of both lattice and electron dynamics.

Kurzfassung

Ferroelektrische Materialien haben aufgrund ihrer schaltbaren Polarisation, Ferroelastizität, Piezoelektrizität und Pyroelektrizität große wissenschaftliche Aufmerksamkeit auf sich gezogen. Diese Eigenschaften sind für zahlreiche technologische Anwendungen von entscheidender Bedeutung, darunter ferroelektrische Transistoren, photovoltaische Zellen und photostriktive Aktoren. Der Prototyp eines ferroelektrischen Materials, BaTiO3, zeigt eine spontane Polarisation, die aus der relativen Verschiebung von Kationen und Anionen innerhalb seiner Einheitszelle resultiert. Der Verzerrungsgradient in einem ferroelektrischen Dünnfilm, der aus der Gitteranpassung an das Substrat resultiert, auf dem er epitaktisch gewachsen ist, macht die Wechselwirkung zwischen Gitterstruktur und spontaner Polarisation zu einem faszinierenden und wichtigen Thema sowohl für die Grundlagenforschung als auch für praktische Anwendungen. Diese Dissertation befasst sich mit der Anwendung spektroskopischer Techniken zur Untersuchung der Gitterstruktur und des spontanen Polarisationsprofils von gespannten ferroelektrischen Dünnschichten, sowohl im Gleichgewicht als auch unter optischer Anregung oberhalb der Bandlücke.

Im Gleichgewicht kann der ferroelektrische Polarisationszustand durch Oberflächenladungsausgleich stabilisiert werden, was zu signifikanten Unterschieden in Amplitude und Orientierung zwischen der Oberflächen- und der Volumen-Ferroelektrik führen kann. Das Verständnis der Mechanismen, die einer stabilen Oberflächenpolarisation in ferroelektrischen Dünnschichten zugrunde liegen, ist entscheidend für die aktive Kontrolle der Oberflächenpolarisation selbst. Stehende Röntgenwellen und Photoelektronenspektroskopie werden verwendet, um das Oberflächenpolarisationsprofil von BaTiO3-Dünnfilmen mit unterschiedlichen Spannungen zu kartieren. Diese Informationen geben Aufschluss darüber, wie die Volumen-Polarisation sowie die Art, Menge und räumliche Verteilung von Oberflächenadsorbaten die Amplitude und Orientierung der lokalen ferroelektrischen Polarisation nahe der Oberfläche beeinflussen.

Wir nutzen die Anregung oberhalb der Bandlücke, um sowohl die elektronische als auch die Gitterstruktur in einem BaTiO3-Dünnfilm transient zu verändern. Das Verständnis, wie intensive optische Pulse die Elektronenverteilung und die daraus resultierende Gitterverzerrung stören, bietet die Möglichkeit, sowohl die Verzerrung als auch die ferroelektrische Polarisation auf ultrakurzen Zeitskalen zu kontrollieren. Dazu werden zeitaufgelöste Röntgenbeugung, Frequenzverdopplung und optische Reflexion kombiniert, um die Dynamik der Gitterstruktur und der ferroelektrischen Polarisation bei der Absorption optischer Pulse oberhalb der Bandlücke zu untersuchen. Mit zeitaufgelöster Röntgenbeugung werden transiente Gitteränderungen beobachtet und die mittlere Verzerrung bei verschiedenen Laserfluenzen gemessen. Um unsere Daten zu modellieren, kombinieren wir das Zwei-Temperatur-Modell mit der eindimensionalen Dehnungswellengleichung. Wir sehen, dass die maximale durchschnittliche Verzerrung des ferroelektrischen Dünnfilms durch Variation der einfallenden Laserfluenz und der Filmdicke kontrolliert werden kann. Darüber hinaus können wir durch die Kontrolle der Fluenz eine bis zu 30 % reversible Änderung der ferroelektrischen Polarisation erreichen und die Relaxationszeiten sowohl der photoangeregten Ladungsträger als auch der spontanen Polarisation fein abstimmen. Die unterschiedlichen Dynamiken, die in den nichtlinearen optischen Suszeptibilitätstensoren bei optischer Anregung beobachtet werden, deuten auf eine nicht-thermische transiente Symmetrieänderung in unserer Probe hin. Dies wird auf eine stark gerichtete lichtinduzierte Polarisationsinstabilität zurückgeführt, die auch theoretisch vorhergesagt wird. Schließlich zeigen unsere Daten, dass die photoinduzierten Variationen der ferroelektrischen Polarisation sowohl das Ergebnis von Gitter- als auch von Elektronendynamik sind.

List of publications

Part of this thesis

- **Le Phuong Hoang**, Irena Spasojevic, Tien-Lin Lee, David Pesquera, Kai Rossnagel, Jörg Zegenhagen, Gustau Catalan, Ivan A Vartanyants, Andreas Scherz, Giuseppe Mercurio. Surface Polarization Profile of Ferroelectric Thin Films Probed by X-Ray Standing Waves and Photoelectron Spectroscopy. *Scientific Reports* 14, 24250 (2024). DOI: 10.21203/rs.3.rs-4548401/v1

- **Le Phuong Hoang**, David Pesquera, Saptam Ganguly, Gerard Hinsley, Robert Carley, Teguh Citra Asmara, Laurent Mercadier, Giacomo Merzoni, Sergii Parchenko, Justine Schlappa, Martin Teichmann, Zhong Yin, Irena Spasojevic, Camille Carinan, Kai Rossnagel, Tien-Lin Lee , Jörg Zegenhagen, Gustau Catalan, Ivan A. Vartanyants, Andreas Scherz, Giuseppe Mercurio. Lattice and polarization dynamics in a ferroelectric thin film. *In preparation*

Contribution to other publications

- Justine Schlappa, Giacomo Ghiringhelli,Benjamin E. Van Kuiken, Martin Teichmann, Piter Miedema, Jan Torben Delitz, Natalia Gerasimova, Serguei Molodtsov, Luigi Adriano, Bernard Baranasic, Carsten Broers, Robert Carley, Patrick Gessler, Nahid Ghodrati, David Hickin, **Le Phuong Hoang**, Manuel Izquierdo, Laurent Mercadier, Giuseppe Mercurio, Sergii Parchenko, Marijan Stupar, Zhong Yin, Leonardo Martinelli, Giacomo Merzoni, Ying Ying Peng, Torben Reuss, Sreeju Sreekantan Nair Lalithambika, Simone Techert, Tim Laarmann, Simo Huotari, Christian Schroeter, Burkhard Langer, Tatjana Giessel, Robby Buechner, Jana Buchheim, Vinicius Vaz da Cruz, Sebastian Eckert, Grzegorz Gwalt, Chun-Yu Liu,

Frank Siewert, Christian Sohrt, Christian Weniger, Annette Pietzsch, Stefan Neppl, Friedmar Senf, Andreas Scherz, Alexander Foehlischi. The Heisenberg-RIXS instrument at the European XFEL. *Under review in Journal of Synchrotron Radiation*. DOI: 10.48550/arXiv.2403.08461

- A.P. Menushenkov, A. Ivanov, V. Neverov, A. Lukyanov, A. Krasavin, A.A. Yastrebtsev, I. Kovalev, Y. Zhumagulov, A. V. Kuznetsov, V. Popov, G. Tselikov, I. Shchetinin, O. Krymskaya, A.Yaroslavtsev, R. Carley, L. Mercadier, Z. Yin, S. Parchenko, **Le Phuong Hoang**, N. Ghodrati, Y.Y. Kim, J. Schlappa, M. Izquierdo, S. Molodtsov, A. Scherz. Direct evidence of real-space pairing in $BaBiO_3$. *Physical Review Research* 6, 023307 (2024). DOI: 10.1103/PhysRevResearch.6.023307

- Gyeongbo Kang, Gyusang Lee, Changhoo Lee, Ahhyun Seong, Sam Azadi, Robert Carley, Loïc Le Guyader, **Le Phuong Hoang**, Minju Kim, Laurent Mercadier, Giuseppe Mercurio, Sergii Parchenko, Martin Teichmann, Benjamin E. Van Kuiken, Zhong Yin, Sam M. Vinko, Andreas Scherz, Byoung Ick Cho. Nonequilibrium Electron-Phonon Coupling in Warm Dense Copper. *Under review in Physical Review Letters*.

- Lingjia Shen, Ryan Tumbleson, Rajan Plumley, Nathan Drucker, Zach Porter, Sathya R. Chitturi, Arnab Singh, Camille Carinan, **Le Phuong Hoang**, Martin Teichmann, Laurent Mercadier, Robert Carley, Loic Le Guyader, Giuseppe Mercurio, Andreas Scherz, Pablo Villanueva-Perez, Sergio A. Montoya, Sophie Morley, Sujoy Roy, Elizabeth Blackburn, Joshua J. Turner. Realization of measuring correlated spin fluctuations using information theory. *In preparation*.

- Douglas H. Fabini, Kedar Honasoge, Adi Cohen, Sebastian Bette, Kyle M. McCall, Constantinos C. Stoumpos, Steffen Klenner, Mirjam Zipkat, **Le Phuong Hoang**, Jürgen Nuss, Reinhard Kremer, Mercouri G. Kanatzidis, Rainer Pöttgen, Omer Yaffe, Stefan Kaiser, Bettina V. Lotsch. Noncollinear Electric Dipoles in a Polar Chiral Phase of $CsSnBr_3$ Perovskite. *J. Am. Chem. Soc.* 2024, 146, 23, 15701-15717. DOI: 10.1021/jacs.4c00679

- Hao Chu, Sergey Kovalev, Zi Xiao Wang, Lukas Schwarz, Tao Dong, Liwen Feng, Rafael Haenel, Min-Jae Kim, Parmida Shabestari, **Le Phuong Hoang**, Kedar Honasoge, Robert David Dawson, Daniel Putzky, Gideok Kim, Matteo Puviani, Min Chen, Nilesh Awari, Alexey N. Ponomaryov,

Igor Ilyakov, Martin Bluschke, Fabio Boschini, Marta Zonno, Sergey Zhdanovich, Mengxing Na, Georg Christiani, Gennady Logvenov, David J. Jones, Andrea Damascelli, Matteo Minola, Bernhard Keimer, Dirk Manske, Nanlin Wang, Jan-Christoph Deinert, Stefan Kaiser. Fano interference between collective modes in cuprate high-T_c superconductors. *Nat Commun* 14, 1343 (2023). DOI: 10.1038/s41467-023-36787-4

Contents

Acronyms

BBO Beta Barium Borate

BTO $BaTiO_3$

DSO $DyScO_3$

EAL effective attenuation length

FEL free electron laser

GSO $GdScO_3$

IMFP inelastic mean free path

NOPA non-colinear optical parametric amplifier

PE photoelectron

PFM piezoresponse force microscopy

PMT photomultiplier

RSM reciprocal space mapping

SHG optical second harmonic generation

SRO $SrRuO_3$

SSO $SmScO_3$

THG third harmonic generation

XPS X-ray photoelectron spectroscopy

XRD X-ray diffraction

XSW X-ray standing waves

1. Introduction

Ferroelectric thin films have garnered significant scientific interest due to their switchable polarization, ferroelasticity, piezoelectricity, and pyroelectricity, all of which are essential for various technological applications such as storage disks, ferroelectric transistors, photovoltaic cells, and photostrictive actuators [1–4]. Displacive ferroelectrics like $BaTiO_3$ possess an intrinsic spontaneous polarization arising from the relative displacement of cations and anions within the unit cell [5]. This polarization can be manipulated by altering the lattice parameters of the ferroelectric materials [6, 7]. To achieve this, ferroelectric thin films are often grown on substrates with different lattice constants, where the resulting lattice mismatch can induce uniform strain or strain gradients in the films [8].

At equilibrium, the distribution of ferroelectric polarization at the surface can differ from the bulk and has been investigated theoretically, exploring parameters such as surface termination and adsorbates [9, 10]. However, there is still a lack of experimental methods that can simultaneously probe both the surface ferroelectric polarization and the chemical composition of adsorbates at the film surface. Determining the surface polarization is significant for two main reasons. Firstly, from a fundamental perspective, uncompensated charges on the surface of a ferroelectric thin film can be screened through various mechanisms, such as external charges from adsorbates [11–15] or reconstruction of the top unit cells to minimize surface energy [16–18]. This can affect the polarization of deeper layers and, in very thin films, the one of the entire sample [19]. Thus, probing and understanding the stabilization mechanisms near the surface are crucial for controlling the ferroelectric polarization in thin films. Secondly, from an application standpoint, ferroelectrics are proposed as catalysts with switchable chemical activity, alternating between reducing and oxidizing surfaces depending on the polarization direction [20–25]. Therefore, determining the surface polarization is essential for developing efficient ferroelectric catalysts.

In addition to the equilibrium state, the non-equilibrium state of $BaTiO_3$ thin

films presents several intriguing aspects. Under above-bandgap optical excitation, recent time-dependent density functional theory (TD-DFT) calculations by Lian and coworkers [26] on $BaTiO_3$ indicate that an electronic transition occurs from O 2p to Ti 3d orbitals. This transition reduces the asymmetric electron distribution and displaces ions from their equilibrium positions, resulting in a switch of the ferroelectric polarization. In systems with broken inversion symmetry, the bulk photovoltaic and inverse piezoelectric effects are the primary mechanisms explaining lattice deformation and polarization dynamics under optical excitation [27–29]. However, thermal lattice deformation can also play a significant role. Choi and his colleagues [6] demonstrated that heating a strained $BaTiO_3$ thin film induces a phase transition from ferroelectric, at room temperature, to paraelectric, above the Curie temperature (T_c) at few 100s $^{\circ}C$, with the exact value depending on the strain of the film. In this work [6], it was also realized that the linear expansion coefficient of a strained $BaTiO_3$ thin film is positive at room temperature, it becomes negative near T_c, and then again positive above T_c. Despite these insights, experimental studies that simultaneously investigate photoinduced lattice deformation and polarization changes are still lacking. Various mechanisms could drive variations of ferroelectric polarization and lattice structure upon optical excitation, including bulk photovoltaic effects, inverse piezoelectric effect, photoexcited carrier separation at the Schottky interface, domain wall rearrangement, and heating effects [27–33]. To achieve controllable optomechanical deformation and light-induced control of the ferroelectric polarization, it is crucial to probe and understand these driving mechanisms. Moreover, gaining full control over light-induced mechanical and electronic processes holds great promise for wireless and remote optomechanical applications, such as photostrictive microsensors [29] and energy storage devices [34, 35]. Therefore, determining the transient changes in lattice deformation and ferroelectric polarization upon optical excitation is a vital step towards developing efficient optomechanical and optoelectronic devices.

Synchrotrons and free-electron lasers have proven highly effective in investigating the complex dynamics of various materials under different external conditions, owing to their exceptional time and energy resolution [36]. To study solid lattice structures, X-ray diffraction and X-ray standing waves techniques are employed. X-ray diffraction, which uses X-ray wavelengths comparable to the size of a single crystal unit cell, can detect minute changes in lattice parameters and atomic displacements on a picosecond timescale. The X-ray

standing waves synchrotron technique combines X-ray diffraction and X-ray spectroscopy, allowing for precise determination of atomic positions with picometer accuracy along a given direction and chemical specificity. This method has been extensively employed for accurately determining atomic positions in single crystals and adsorbates on crystal surfaces [37–41]. Additionally, the X-ray standing waves technique has been effectively used to measure the average polarity of non-centrosymmetric single crystals and thin films, including ferroelectric thin films [42–46]. However, combining X-ray standing waves with X-ray photoelectron spectroscopy to probe atomic positions and spontaneous polarization near the surface of ferroelectric thin films has not yet been realized.

In optics, the development of ultrashort monochromatic laser pulses, ranging from femtoseconds to picoseconds and with extremely high field strengths, represents a significant advancement in electromagnetic spectroscopy. These high field strengths are comparable to the electromagnetic forces that bind electrons and atoms, making the strong incident field a major driver of nonlinear processes in materials. These processes induce oscillations at the same frequency as the incident laser pulse, as well as at linear combinations of this frequency, leading to high harmonic generation [47]. In optical reflectance and second harmonic generation spectroscopy, the linear and second-order responses of a material to monochromatic light pulses are measured. Polarimetry measurements enable selective probing of different components of the nonlinear susceptibility tensor, allowing for characterization of the material's symmetry. Second-order nonlinear measurements can uncover more symmetries than linear measurements because they probe a greater number of symmetry tensor elements [48, 49]. However, time-resolved optical reflectance provides information about the electronic distribution near the Fermi level [50, 51], which cannot be disentangled by time-resolved second harmonic generation alone. Importantly, a detailed understanding of the dynamics of lattice structure, ferroelectric polarization, and electronic structure near the Fermi level, as well as their correlations upon optical excitation, has yet to be achieved by combining time-resolved X-ray diffraction, second harmonic generation, and optical reflectance techniques.

In this thesis, we present the integration of several spectroscopic techniques, based on synchrotrons, free-electron lasers, and optical lasers, to investigate the surface polarization profile and the transient changes in lattice structure, electronic structure, and ferroelectric polarization in $BaTiO_3$ ferroelectric thin films upon above-bandgap optical excitation. This research employs these

spectroscopic methods to study specific properties of a prototypical ferroelectric material, grounded in a comprehensive understanding of its fundamental properties and the operating principles of the methods applied. We hope that the findings of this thesis will not only enhance knowledge about the surface polarization and structural dynamics of ferroelectric thin films, but also serve as a template for future studies to combine different spectroscopic methods to resolve the complex dynamics of other materials relevant for technological applications, such as multiferroics.

Outline of the thesis

The thesis covers the following topics in 5 chapters:

1. **Understanding Spectroscopic Techniques and Ferroelectric $BaTiO_3$ Thin Films**: This includes the working principles of X-ray diffraction, X-ray photoelectron spectroscopy, X-ray standing waves, and optical second harmonic generation, along with the fundamental properties of ferroelectric $BaTiO_3$ thin films.
2. **Surface Polarization Profile in Ferroelectric $BaTiO_3$ Thin Films**: Investigating the surface polarization profile by combining X-ray standing waves and photoelectron spectroscopy.
3. **Light-Induced Lattice Deformation and Polarization Modification**: Examining lattice deformation and polarization changes upon above-bandgap excitation and their applications.

Chapter 2 discusses the theoretical principles of the experimental techniques, such as X-ray diffraction, X-ray photoelectron spectroscopy, X-ray standing waves, and optical second harmonic generation.

Chapter 3 provides an overview of material properties, details of sample growth, and characterization techniques for ferroelectric thin films. The characterization techniques include grazing X-ray reflectivity and lab-based X-ray diffraction for thickness determination, reciprocal lattice mapping for lattice constant determination, and piezoresponse force microscopy for measuring the average polarization of thin films.

Chapter 4 describes the experimental setups in detail. It begins with the X-ray standing waves setup at the Diamond Light Source facility, followed by the optical setup for static and time-resolved second harmonic generation at the SCS instrument of the European XFEL, and the experimental scheme for time-resolved X-ray diffraction at SCS.

Chapter 5 investigates the surface polarization profile in ferroelectric $BaTiO_3$ thin films using X-ray standing waves and photoelectron spectroscopy. The X-ray standing wave technique enables direct probing of the surface polarization profile, as opposed to the average film polarity, with picometer accuracy. It

determines the positions of Ti and Ba atoms near the surface of three differently strained $BaTiO_3$ thin films grown on scandate substrates, with a $SrRuO_3$ (SRO) bottom electrode. X-ray photoelectron spectroscopy provides detailed information on oxygen-containing species adsorbed on the surface under ambient conditions. Combining structural and spectroscopic data, the chapter concludes on the mechanisms stabilizing surface polarization in the studied samples, linking the local ferroelectric polarizations to surface charges from oxygen-containing adsorbates.

Chapter 6 explores the dynamics of lattice structure and ferroelectric polarization in a ferroelectric $BaTiO_3$ (001) thin film grown on a $GdScO_3$ substrate with a $SrRuO_3$ bottom electrode. The techniques employed are: time-resolved X-ray diffraction, optical second harmonic generation, and optical reflectance. This chapter discusses the manipulation of the strain profile by tuning the incident laser fluence and film thickness, revealing that photoinduced polarization modification is driven by both lattice and electronic changes. An analytical platform is established for calculating the strain profile within a thin film induced by intense optical excitation.

2. Experimental techniques

In this chapter, we provide the theoretical principles of the experimental techniques employed to study the lattice structure and polarization of ferroelectric thin films. The techniques we employed are: X-ray standing waves, X-ray diffraction, X-ray photoelectron spectroscopy, optical second harmonic generation polarimetry, and optical reflectance. In addition, we have performed X-ray diffraction, optical second harmonic generation polarimetry, and optical reflectance in a pump-probe scheme.

2.1. X-ray standing waves from thin films

The X-ray standing waves (XSW) technique is highly effective for identifying atomic positions within crystals, surfaces, and their adsorbates [37–41]. In a perfect crystal, the interference between incident and Bragg-diffracted X-ray plane waves generates an X-ray standing wave field, characterized by the following sinusoidal modulation of the X-ray intensity I_{XSW} (Figures 3.1a-b):

$$I_{\mathrm{XSW}}\left(E_\nu\right) \propto 1 + \left|\frac{\mathcal{E}_{\mathrm{h}}}{\mathcal{E}_0}\right|^2 + 2\left|\frac{\mathcal{E}_{\mathrm{h}}}{\mathcal{E}_0}\right| \cos\left(\alpha(E_\nu) + \boldsymbol{hr}\right), \tag{2.1}$$

where $\boldsymbol{h} = 2\pi\boldsymbol{H}$, and $\boldsymbol{H}$ represents the reciprocal lattice vector. In Equation (2.1), the three terms correspond to the incident, Bragg-diffracted, and interference X-ray waves, respectively. As the incident photon energy E_ν traverses the (hkl) Bragg reflection, the phase $\alpha(E_\nu)$ between the Bragg-diffracted $\mathcal{E}_{\mathrm{h}}$ and incident $\mathcal{E}_0$ electric field amplitudes shifts by π. This causes the XSW field to move along $\boldsymbol{H}$ by $d_{\mathrm{hkl}}/2$, where $d_{\mathrm{hkl}} = |\boldsymbol{H}|^{-1}$ is the distance between two adjacent (hkl) atomic planes (Figure 3.1b). Atoms located at different positions within the unit cell experience varying levels of X-ray absorption, resulting in different photoelectron (PE) yields as a function of the photon energy E_ν.

In ferroelectric thin films grown on substrates, lattice mismatches often result in strain gradients within the epitaxial layers [8]. As a result, these thin

films are described by a deformation field $\boldsymbol{u}(z)$, which indicates the actual displacement of atoms from their ideal positions in a perfect crystal, and a static Debye-Waller factor $\mathrm{e}^{-W(z)}$, accounting for random atomic displacements along the z direction. Unlike in a perfect crystal, the XSW in a thin film is influenced by the deformation phase $\varphi(z) = \boldsymbol{h} \cdot \boldsymbol{u}(z)$ due to the crystal deformation field. The intensity of the XSW in a typical ferroelectric thin film is expressed as follows:

$$\begin{aligned} I_{\mathrm{XSW}}\left(E_\nu, z\right) = 1 + R\left(E_\nu, z\right) + 2C\sqrt{R\left(E_\nu, z\right)}\mathrm{e}^{-W(z)} \\ \cos\left(\alpha(E_\nu, z) + \varphi\left(z\right) + 2\pi z/d_{\mathrm{hkl}}\right), \end{aligned} \tag{2.2}$$

where $R_0(E_\nu) = R(E_\nu, 0)$ represents the observable X-ray diffracted intensity at the sample surface ($z = 0$), with the parameter C being dependent on the X-ray polarization (Section 2.2). Analyzing the XSW generated in a ferroelectric thin film, the PE yield curve is expressed as follows:

$$\begin{aligned} \kappa_\gamma^s(E_\nu) = I_0^{-1}\int_0^{t_{L_0}} dz\rho_{\mathrm{yi}}\left(E_\nu, z, \gamma\right)\left|T\left(E_\nu, z\right)\right|^2\Big[1 + R\left(E_\nu, z\right) \\ +2C\sqrt{R\left(E_\nu, z\right)}\mathrm{e}^{-W_0}F_{c,\gamma}^s\cos\left(\alpha(E_\nu, z) + \varphi_0 + 2\pi P_{c,\gamma}^s\right)\Big]. \end{aligned} \tag{2.3}$$

From this analytical expression, we can determine the average position and distribution of atoms s, referred to as the coherent position $P_{c,\gamma}^s$ and coherent fraction $F_{c,\gamma}^s$, respectively. These parameters correspond to the phase and amplitude of the structure factor $\boldsymbol{S}_{\boldsymbol{h}}^s = \sum_j \exp(\mathrm{i}\boldsymbol{h}\boldsymbol{r}_j^s) = \left|\boldsymbol{S}_{\boldsymbol{h}}^s\right|\exp(\mathrm{i}\varphi_{\boldsymbol{h},\gamma}^s)$, with atoms located at positions $\boldsymbol{r}_j^s$. Specifically, $P_{c,\gamma}^s = \varphi_{\boldsymbol{h},\gamma}^s/(2\pi)$ and $F_{c,\gamma}^s = |\boldsymbol{S}_{\boldsymbol{h}}^s|\mathrm{e}^{-W_s}$, where e^{-W_s} accounts for thermal and static atomic displacements through the Debye-Waller factor. Thus, the absolute average position of atoms s within the unit cell along $\boldsymbol{H}$ is $z_\gamma^s = P_{c,\gamma}^s d_{\mathrm{hkl}}$, and their spatial distribution is represented by $F_{c,\gamma}^s$. The values range between $0 < P_{c,\gamma}^s < 1$ and $0 < F_{c,\gamma}^s < 1$, with $F_{c,\gamma}^s = 1$ indicating all atoms are at the same z position, and $F_{c,\gamma}^s = 0$ indicating a uniform distribution of two or more atomic positions within the unit cell.

In Equation (2.3), the PE yield function $\kappa_\gamma^s(E_\nu)$ represents the sum of yield contributions from atoms in the top layer L_0 at positions $0 < z < t_{L_0}$, weighted by $\rho_{\mathrm{yi}}(E_\nu, z, \gamma)$, the XSW transmission $T\left(E_\nu, z\right)$, and normalized by $I_0 = \int_0^{t_{L_0}} dz\rho_{\mathrm{yi}}(E_\nu, z, \gamma)$. The function $\rho_{\mathrm{yi}}(E_\nu, z, \gamma) = \exp\left(-z/\lambda_{l,\gamma}\right)$ provides the probability of detecting a PE from the atomic core level l at depth z, with

an exit angle γ from the sample surface. The parameter $\lambda_{l,\gamma} = \lambda_l(E_\nu)\sin\gamma$ represents the electron escape depth [52], and $\lambda_l(E_\nu)$ indicates the inelastic mean free path (IMFP), or more accurately, the effective attenuation length (EAL) that includes elastic scattering effects [53]. By adjusting γ, surface sensitivity can be varied, providing average atomic positions at different depths. To determine the average distribution of atoms s at a given exit angle γ, the measured PE yield curve is fitted with Equation (2.3) using $P^s_{c,\gamma}$ and $F^s_{c,\gamma}$ as fitting parameters. All other quantities in Equation (2.3) can be calculated from known sample properties (Section 2.2) or derived from fitting Bragg reflectivity data, such as the average amorphization e^{-W_0} of layer L_0 and the corresponding deformation phase φ_0.

An example of PE yields from a $BaTiO_3$ (BTO) thin film is given in Figure 2.1. The standing wave $I_{XSW}(E_\nu, z)$ is formed with the periodicity d_{hkl} equal to the distance between two consecutive Ba planes in (001) direction (Figures 2.1a-b). In the unit cell of BTO, the distance between Ti atom and Ba plane is around half of d_{hkl}. When Ti atoms are at the maxima of $I_{XSW}(E_\nu, z)$, Ba atoms are at the minima of $I_{XSW}(E_\nu, z)$. Therefore, the phase difference between the PE yields $\kappa^s_\gamma(E_\nu)$ of Ti and Ba is approximately 180° (Figure 2.1c). The phase sensitivity of the XSW allows the atomic positions to be determined with picometer spatial resolution by monitoring the corresponding PE yields.

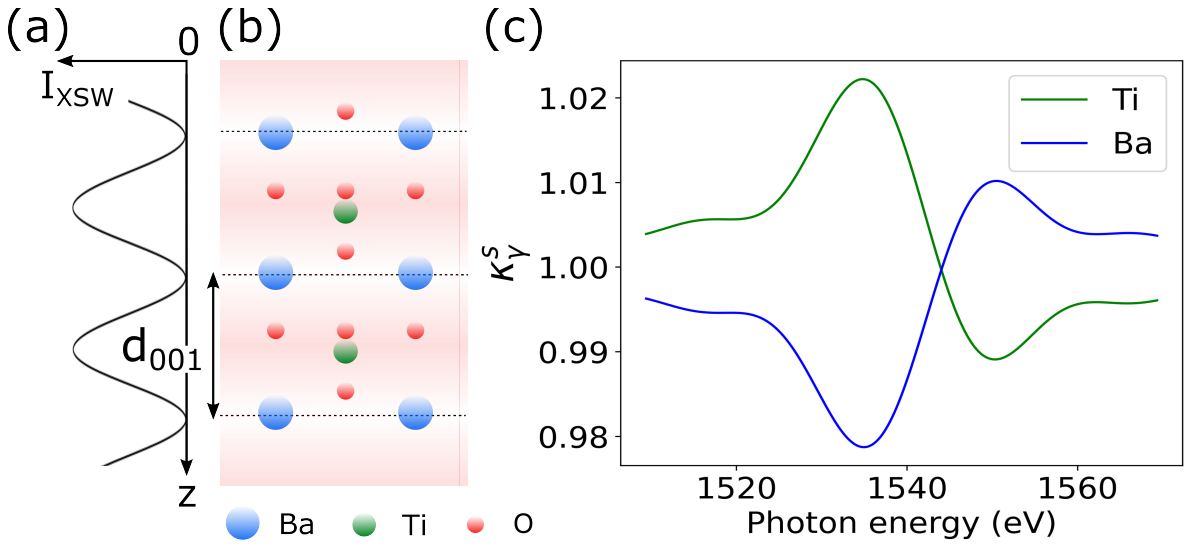

Figure 2.1.: Sketch of the XSW technique. (a) XSW intensity of BTO (001) Bragg reflection and z axis orientation, with z = 0 at the sample surface. (b) Side view of the top two BTO unit cells. (c) The PE yields from Ti (green) and Ba (blue).

2.2. X-ray diffraction from thin films

In general, the X-ray diffraction (XRD) is the technique used to characterize the lattice parameters of crystalline systems [54–56]. In Section 2.1, the XSW intensity is dependent of the X-ray diffracted intensity $R_0(E_\nu)$ at the sample surface ($z = 0$). In this section, we will derive the mathematical expression of $R(E_\nu, z)$ using the X-ray dynamical theory of diffraction. The X-ray dynamical theory of diffraction is based on the elastic scattering between the X-rays and electrons within the periodic lattice [37]. To begin with, the following Takagi-Taupin equation [57–59] is used to derive the reflection amplitude of X-rays $r(E_\nu, z)$ from a thin film:

$$-\mathrm{i}L_{ex}\frac{dr(E_\nu,z)}{dz} = 2[-y(E_\nu) - \mathrm{i}y_0 + y_\varphi(z)]r(E_\nu,z) + C_1[1 + r^2(E_\nu,z)], \quad (2.4)$$

where β is the geometry factor and Y is the parameter related to the crystal susceptibility. C_1 is a factor related to the incident polarization of X-rays. In Equation (2.4), the dimensionless parameter

$$y(E_\nu) = 2\sqrt{\beta}(\sin^2\theta_B)\frac{E_\nu - E_B}{E_B X_\mathrm{r}} + \chi_{0\mathrm{r}}\frac{1+\beta}{2\sqrt{\beta}X_\mathrm{r}} \quad (2.5)$$

indicates the energy deviation from the exact Bragg energy E_B over the incident photon energy scan. The parameter

$$y_0 = \frac{\chi_{0\mathrm{i}}(1+\beta)}{2\sqrt{\beta}X_\mathrm{r}} \quad (2.6)$$

represents the attenuation of X-ray intensity due to photoelectric absorption, and

$$y_\varphi(z) = \frac{L_{ex}}{2}\frac{d\varphi(z)}{dz} \quad (2.7)$$

indicates the shift of diffraction planes due to lattice deformation and the deformation phase $\varphi(z)$ (Section 2.1). Here, the extinction length L_{ex} represents the penetration depth of the XSW field and is defined as $L_{ex} = (\lambda_B\Gamma_\mathbf{0})/(\pi\sqrt{\beta}X_\mathrm{r})$ [60].

Now, we consider a thin film with total thickness t_{total} which is divided into n sublayers L_i (with $i = 0, ..., n-1$) of equal thickness t_i (Figure 2.2). The sublayers are numbered from the top to the bottom of the thin film.

Accordingly, the top sublayer is labeled as L_0 and the bottom L_{n-1}. The X-ray diffracted intensity at the depth z_i from the sample surface at photon energy E_ν is calculated as:

$$R(E_\nu, z_i) = \beta |Y|^2 |r(E_\nu, z_i)|^2, \tag{2.8}$$

where

$$r(E_\nu, z_i) = \frac{x_1 - x_2 x_3}{1 - x_3} \tag{2.9}$$

is the local reflection amplitude at the depth z_i from the sample surface at photon energy E_ν with

$$x_1 = -\left(b + \sqrt{b^2 - C_1^2}\right)/C_1, \tag{2.10}$$

$$x_2 = -\left(b - \sqrt{b^2 - C_1^2}\right)/C_1, \tag{2.11}$$

$$x_3 = (x_1 - r_{t_i}) \exp(\sigma t_i)/(x_2 - r_{t_i}), \tag{2.12}$$

and

$$\sigma = 2\mathrm{i}\sqrt{b^2 - C_1^2}/L_{ex}, \tag{2.13}$$

$$b = -y(E_\nu) - \mathrm{i}y_0 + y_\varphi(z). \tag{2.14}$$

The reflection amplitude at the bottom of L_i is defined as $r_{t_i} = r(E_\nu, z_i + t_i)$, and at the top of L_i is defined as $r_i = r(E_\nu, z_i)$, which is then treated as the reflection at the bottom of layer L_{i-1} ($r_i = r_{t_{i-1}}$) (Figure 2.2). The reflection amplitude at the top of L_i is a function of the reflection amplitude at the bottom of L_i (Equation (2.9) and (2.12)). Starting from the reflection amplitude $r_{t_{total}} = r(E_\nu, t_{total})$ at the bottom of the lowest layer, we can iteratively calculate the reflection $R_0(E_\nu)$ at the surface by means of Equations (2.8-2.12). In the case that the thickness of the sample is much larger than the penetration depth of X-rays, which is on the same order of magnitude as the extinction length L_{ex} ($t_{total} >> L_{ex}$), the boundary condition at the bottom of the sample of $r_{t_{total}} = 0$ is valid. Starting from this boundary condition, Equation (2.8) is employed recursively to calculate the diffracted intensity at the top of L_0 ($z_0 = 0$), i.e., $R(E_\nu, 0)$ (Section 2.1). The full analytical expression of $R(E_\nu, z)$ is given in Section A.1. This analytical solution of Takagi-Taupin equation will be used to model the experimental XRD data in Section 3.3.

We calculate the X-ray diffracted intensity from a multilayer system by applying the steps described above. For example, when we have a BTO thin

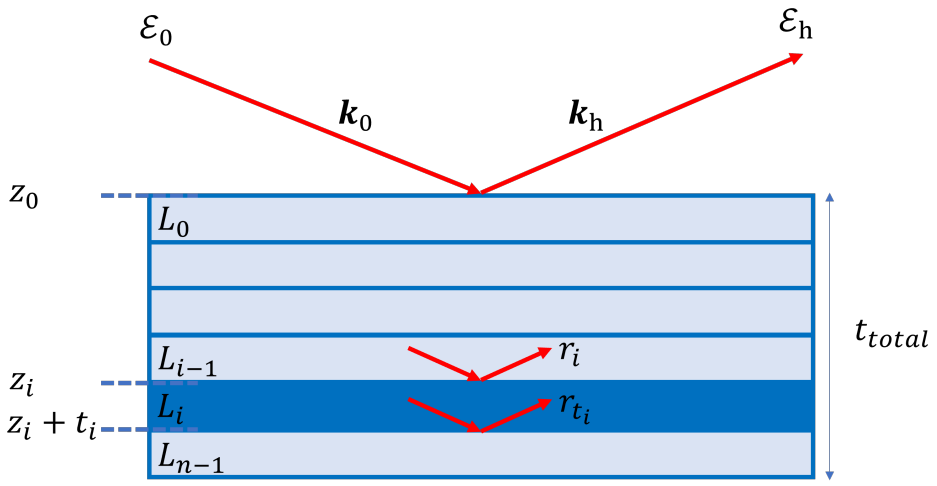

Figure 2.2.: Schematic illustration of the X-ray diffraction from a thin film. The illustrated thin film, with total thickness t_{total}, includes n sublayers L_i (with $i = 0, ..., n-1$) of equal thickness t_i. The depth z_i from the surface with $z_0 = 0$ is denoted. The local reflection amplitude at the interface between sublayers L_{i-1} and L_i is r_i. The local reflection amplitude at the bottom of the sublayer L_i is r_{t_i}. The Bragg-diffracted and incident electric field amplitudes are indicated as $\mathcal{E}_h$ and $\mathcal{E}_0$, respectively. The incident and Bragg-diffracted wave vectors are indicated as $\boldsymbol{k}_0$ and $\boldsymbol{k}_h$, respectively.

film grown on a $GdScO_3$ (GSO) substrate with SRO in between as a bottom electrode, the X-ray-diffracted intensity is computed from the bottom of the substrate to the top of the thin film (Figure 2.3a). In this example, we assume that the lattice parameters in each layer remain the same along the thickness (BTO: a = b = 3.967 Å, c = 4.083 Å, SRO: a = b = 3.967 Å, c = 3.943 Å, GSO: a = b = 3.967 Å, c = 3.973 Å). In this calculation, the thicknesses of BTO, SRO, and GSO are t_{BTO} = 34.5 nm, t_{SRO} = 47 nm, and t_{GSO} = 0.5 mm, respectively. In addition, the incident angle of X-ray beam is 86° relative to the sample surface. Because the thickness of GSO is 0.5 mm which is much larger than the extinction length (2 μm), the reflection amplitude at the bottom of the substrate is $r(E_v, t_{BTO} + t_{SRO} + t_{GSO}) = 0$. This value is utilized to calculate the amplitude $r(E_v, t_{BTO} + t_{SRO})$ at the interface between GSO and SRO layers with GSO parameters (x_{1GSO}, x_{2GSO}, x_{3GSO}, σ_{GSO}, b_{GSO}). Similarly, the reflection amplitude $r(E_v, t_{BTO} + t_{SRO})$ at the bottom of SRO electrode is used to calculate the reflection amplitude $r(E_v, t_{BTO})$ at the interface between SRO and BTO layers. Eventually, the reflection amplitude $r(E_v, t_{BTO})$ at the bottom of BTO thin film is employed to calculate the reflection amplitude

$r(E_\nu, 0)$ and intensity $R(E_\nu, 0)$ at the top of BTO thin film applying Equation (2.8). As a result, the simulated intensity $R(E_\nu, 0)$ around the BTO diffraction peak at (001) crystal orientation is calculated and shown in Figure 2.3b.

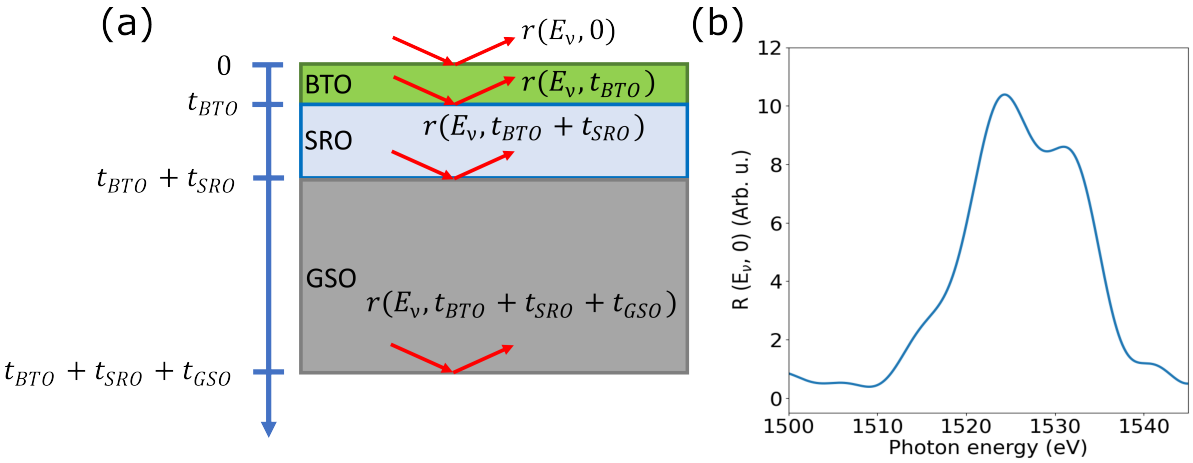

Figure 2.3.: X-ray diffraction from a multilayer: sketch and simulation. (a) Sketch of a multilayer sample. (b) Simulation of the (001) Bragg diffraction peak of a BTO thin film. The simulation is performed using the following thicknesses of BTO, SRO, and GSO: $t_{BTO} = 34.5$ nm, $t_{SRO} = 47$ nm, and $t_{GSO} = 0.5$ mm.

2.3. X-ray photoelectron spectroscopy

The X-ray photoelectron spectroscopy (XPS) is an analytical method with surface sensitivity and chemical specificity [61–65]. The physical principle of XPS is the photoelectric effect [66, 67] which is the energy transfer from X-ray photons to core level electrons when the sample surface is illuminated by X-rays photons. The result of X-ray absorption is the photoionization of atoms, which is described in Figure 2.4. In the photoionization process, the ejection of the core electron (primary electron) upon X-ray photon absorption leads to a core vacancy (Figure 2.4a). The vacancy is then occupied by an electron from an upper level. The energy released during this relaxation is converted to either photon emission (X-ray fluorescence, Figure 2.4b) [68] or the emission of an Auger electron (secondary electron, Figure 2.4c) [69].

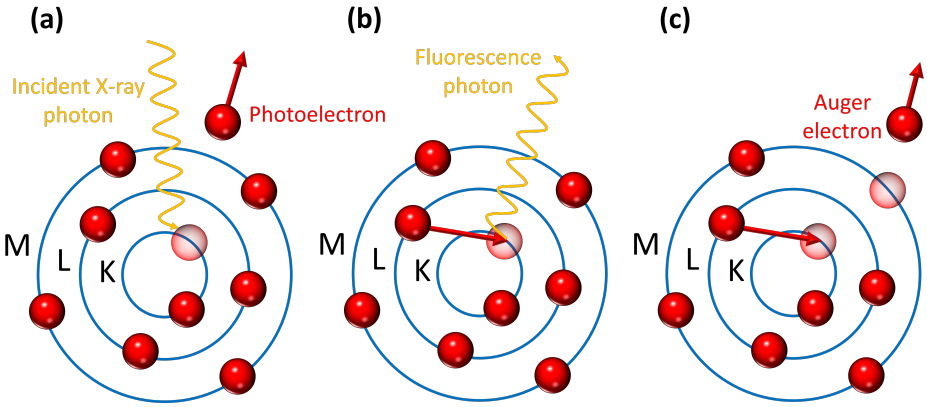

Figure 2.4.: Schematic illustration of photoelectrons, fluorescence photons and Auger electrons. (a) An electron from core level is ejected, leaving behind a vacancy. (b) An electron from outer shell fills up the vacancy, leading to X-ray fluorescence emission or (c) ejection of another electron in outer shell (Auger electron).

We focus here on the photoelectrons (Figure 2.4a). The basic formulation of photoelectric effect is the following:

$$BE = E_\nu - KE - \Phi_{spec}, \tag{2.15}$$

where $E_\nu = h\nu$ is the X-ray photon energy, BE is the binding energy of the electron tightly bound to the nucleus, KE is the kinetic energy of the emitted electron, which is measured by the spectrometer, and Φ_{spec} is the work function of the spectrometer. The energy level diagram of an XPS measurement is shown

in Figure 2.5. The binding energy of a photoelectron is independent of the X-ray photon energy. Only the kinetic energy will change with different X-ray photon energies (Equation (2.15)). Photoelectrons from atoms in different chemical states have different binding energies, thus XPS has chemical specificity.

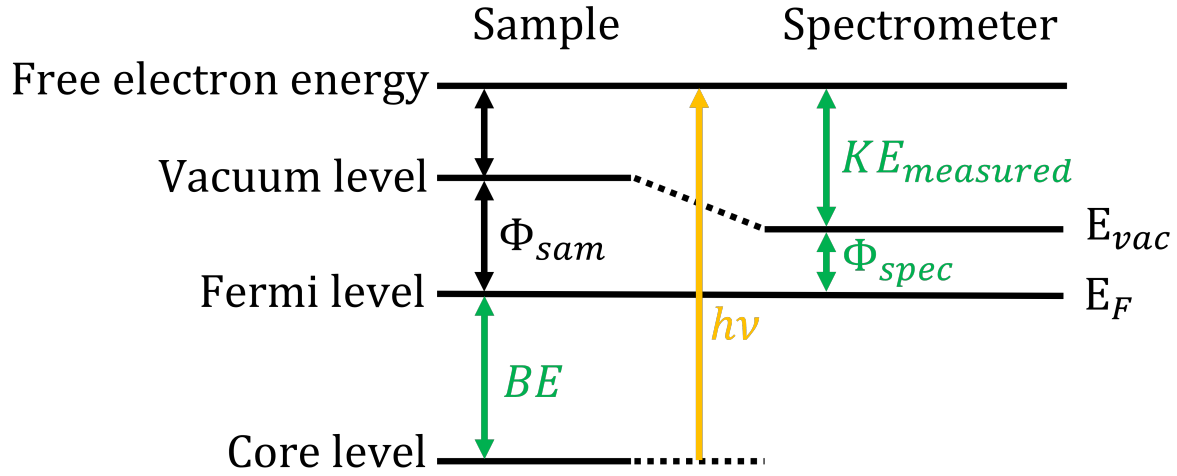

Figure 2.5.: Energy levels scheme of an XPS experiment. The work function Φ_{sam} of the sample varies according to different materials. In case of $\Phi_{sam} > \Phi_{spec}$, the X-ray photon energy needs to be larger than Φ_{sam} to eject the photoelectrons over the vacuum level E_{vac}. For $\Phi_{sam} < \Phi_{spec}$, the X-ray photon energy needs to be larger than Φ_{spec} for the photoelectrons to enter the spectrometer. The binding energy BE is defined by the atomic core level and the Fermi level E_F.

Another important property of XPS is the surface sensitivity, which results from the IMFP $\lambda_l(E_v)$, which is typically less than 1 nm. This parameter is defined as the mean distance that photoelectrons with a specified energy can travel along their paths between inelastic collisions within a material [52]. The IMFP mostly depends on the kinetic energy of the photoelectrons. The details of the IMFP calculation are given in Section A.3. Another relevant parameter to the surface sensitivity is the electron escape depth, which is $\lambda_{l,\gamma} = \lambda_l(E_v)\sin\gamma$, where γ is the exit angle of photoelectrons from the sample surface. Different γ provides the different electron escape depth and thus the depth selectivity of PE spectra. Analytically, the relative contribution of photoelectrons of atom s emitted from a region between the surface $z_0 = 0$ and the depth z_i, within the exit angle range (γ_l, γ_h) is

$$I^s_{(z_0,z_i),\gamma_j} = (I^s_{\infty,\gamma_j})^{-1} \int_{z_0}^{z_i} \int_{\gamma_l}^{\gamma_h} \rho_{\mathrm{yi}}(E_v, z, \gamma)\, d\gamma dz, \tag{2.16}$$

where γ_l and γ_h are the lower and upper limit of exit angle from the sample surface and I^s_{∞,γ_j} calculated as:

$$I^s_{\infty,\gamma_j} = \int_{z_0}^{\infty} \int_{\gamma_l}^{\gamma_h} \rho_{\mathrm{yi}}\left(E_\nu, z, \gamma\right) d\gamma dz, \tag{2.17}$$

and $\rho_{\mathrm{yi}}\left(E_\nu, z, \gamma\right) = \exp\left(-z/\lambda_{l,\gamma}\right)$ represents the probability of finding a photoelectron from the atomic core level l at depth z, with exit angle γ (Section 2.1). This formulation can be used to design a setup with the specific angle ranges of detection which provides the desired depth sensitivity.

2.4. Optical second harmonic generation polarimetry

The optical second harmonic generation (SHG) is a two-photon sum frequency process in which the absorption of two incident photons from the identical light field at the frequency ω leads to the emission of a photon at the double frequency 2ω [47, 70]. This technique is proposed to characterize the variation in the spontaneous polarization of ferroelectric thin films [6, 47, 70]. The basis of this method lies on the nonlinear interaction between a light wave and a crystal. When a light wave is traveling through a crystal, it gives rise to multipolar moments which can be classified as electric dipole moment, magnetic dipole moment, and quadrupolar moment [71, 72]. In general, the contribution of electric dipoles is significantly larger than that of magnetic dipoles and electric quadrupoles by a factor λ/a, with the wavelength λ of the incident light and the lattice parameter a of the crystal [48]. For example, the incident wavelength of 800 nm and the typical lattice parameter of BTO of 4 Å provide a contribution ratio of electric dipoles over magnetic dipoles and electric quadrupoles of 2000. In addition, the electric dipole mechanism is active only in a noncentrosymmetric materials (like ferroelectrics) [49] which is the material of interest in this thesis. The electric dipoles are oscillating at the integer number of frequencies of the incident light waves (ω, 2ω, 3ω,..., $n\omega$) and radiate the electromagnetic waves at the corresponding frequencies. In this optical measurement, we aim to probe the radiation at frequencies 2ω (SHG) and ω (optical reflectance).

The amplitude of the electric dipoles at 2ω can be written as a quadratic function of incident light field

$$P_i(2\omega) = \sum_{j,k} \chi_{ijk} E_j(\omega) E_k(\omega), \tag{2.18}$$

where $E_j(\omega)$ and $E_k(\omega)$ are the incident electromagnetic field components. The optical second-order susceptibility χ_{ijk} is the third-rank tensor which dictates the crystallographic symmetries of the crystal [47, 70]. The amplitude of this second-order susceptibility is generally around 12 orders of magnitude smaller than that of the first-order susceptibility, which represents the amplitude of optical reflectance at ω [47]. Conversely, it is approximately 12 orders of magnitude larger than the third-order susceptibility, which corresponds to the amplitude of third harmonic generation (THG) at 3ω [47]. Indices j and k represent the polarization of two incident photons, while i is the polarization

of the outgoing SHG photon. The amplitude of the tensor element χ_{ijk} can be written as [73]

$$\chi_{ijk} = \frac{mA\varepsilon_0^3}{N_{ed}^2 e^2}(n_i^2(2\omega) - 1)(n_j^2(\omega) - 1)(n_k^2(\omega) - 1), \tag{2.19}$$

where $n_i(2\omega)$, $n_j(\omega)$ and $n_k(\omega)$ are the refractive indices at the frequencies 2ω and ω corresponding to the light polarization i, j, and k. The constant A represents the strength of the nonlinearity, m is the electron mass, N_{ed} is the electric dipole density, e is the elementary charge, and ε_0 is the vacuum permittivity. This relation points out that the amplitude of the tensor element is determined by the refractive indices of a material, i.e., the electronic polarizability [47, 73].

In the Cartesian coordinate of the laboratory, the z axis is perpendicular to the sample surface while the yz plane lies on the incident plane, which is defined by the incident beam and the outgoing beam (Figure 2.6a). The angle of incidence θ is defined by the z axis and the incident beam direction. The rotation angle ϕ of incident polarization is the angle between the incident polarization vector and the yz incident plane. In a SHG polarimetry measurement, the SHG intensity is measured as a function of incident light polarization which is rotated by an angle ϕ about the optical axis, while the outgoing polarization is fixed either at 0° (P-out configuration) or 90° (S-out configuration) with respect to the yz incident plane (Figure 2.6). According to Equation (2.18), the incident polarization component along x is:

$$\begin{aligned} P_x(2\omega) = {} & \chi_{xxx}E_x(\omega)E_x(\omega) + \chi_{xxy}E_x(\omega)E_y(\omega) + \chi_{xxz}E_x(\omega)E_z(\omega) \\ & + \chi_{xyx}E_y(\omega)E_x(\omega) + \chi_{xyy}E_y(\omega)E_y(\omega) + \chi_{xyz}E_y(\omega)E_z(\omega) \\ & + \chi_{xzx}E_z(\omega)E_x(\omega) + \chi_{xzy}E_z(\omega)E_y(\omega) + \chi_{xzz}E_z(\omega)E_z(\omega). \end{aligned} \tag{2.20}$$

Because $E_x(\omega)E_y(\omega) = E_y(\omega)E_x(\omega)$, $E_y(\omega)E_z(\omega) = E_z(\omega)E_y(\omega)$, $E_x(\omega)E_z(\omega) = E_z(\omega)E_x(\omega)$, and $\chi_{ijk} = \chi_{ikj}$ (Kleinman symmetry condition [47]), Equation (2.20) becomes

$$\begin{aligned} P_x(2\omega) = {} & \chi_{xxx}E_x(\omega)E_x(\omega) + \chi_{xyy}E_y(\omega)E_y(\omega) + \chi_{xzz}E_z(\omega)E_z(\omega) \\ & + 2\chi_{xxy}E_x(\omega)E_y(\omega) + 2\chi_{xxz}E_x(\omega)E_z(\omega) + 2\chi_{xyz}E_y(\omega)E_z(\omega). \end{aligned} \tag{2.21}$$

Applying the equalities above also for polarization components along y and z, the SHG polarization components $P_i(2\omega)$ can be written in the following matrix form

$$\begin{pmatrix} P_x(2\omega) \\ P_y(2\omega) \\ P_z(2\omega) \end{pmatrix} = \begin{pmatrix} \chi_{xxx} & \chi_{xyy} & \chi_{xzz} & \chi_{xyz} & \chi_{xxz} & \chi_{xxy} \\ \chi_{yxx} & \chi_{yyy} & \chi_{yzz} & \chi_{yyz} & \chi_{yxz} & \chi_{yxy} \\ \chi_{zxx} & \chi_{zyy} & \chi_{zzz} & \chi_{zyz} & \chi_{zxz} & \chi_{zxy} \end{pmatrix} \begin{pmatrix} E_x^2(\omega) \\ E_y^2(\omega) \\ E_z^2(\omega) \\ 2E_yE_z(\omega) \\ 2E_xE_z(\omega) \\ 2E_xE_y(\omega) \end{pmatrix}. \quad (2.22)$$

In our measurement geometry, the incident light field components are $E_x(\omega)$, $E_y(\omega)$ and $E_z(\omega)$. The component E_x is the projection of the field vector $E(\omega)$ on x axis $E_x(\omega) = E(\omega)\sin\phi$. The component E_y is the projection of the field vector $E(\omega)$ on y axis $E_y(\omega) = E(\omega)\cos\phi\cos\theta$. The component E_z is the projection of the field vector $E(\omega)$ on z axis $E_z(\omega) = -E(\omega)\cos\phi\sin\theta$. Regarding the SHG polarization, the P-out polarization amplitude is the sum of the projections of components P_x, P_y, and P_z along p direction $P_p(2\omega) = P_y(2\omega)\cos\theta + P_z(2\omega)\sin\theta$. The S-out SHG polarization amplitude is the sum of the projections of components P_x, P_y, and P_z along s direction $P_s(2\omega) = P_x(2\omega)$. Assuming that the incident light ω has penetrated a distance l into the material, the SHG intensity is given as [73]

$$I(2\omega) = 2\left(\frac{\mu_0}{\varepsilon_0}\right)^{3/2} \frac{\omega^2\chi_{ijk}^2 l^2}{n_i(2\omega)n_j(\omega)n_k(\omega)} I(\omega)^2 \left(\frac{\sin\frac{1}{2}\Delta kl}{\frac{1}{2}\Delta kl}\right)^2, \quad (2.23)$$

where $\Delta k = k(2\omega) - k(\omega)$, with the wave vector $k(\omega) = \omega/c_{light}$, the light speed c_{light} and the vacuum permeability μ_0. Equation (2.23) points out that the SHG intensity is proportional to χ_{ijk}^2 as well as $I(\omega)^2$. In addition, since $P_p(2\omega)$ and $P_s(2\omega)$ are proportional to χ_{ijk} (Equation (2.18)), the SHG intensities at P-out $I_p(2\omega)$ and S-out $I_s(2\omega)$ configurations are proportional to $P_p^2(2\omega)$ and $P_s^2(2\omega)$, respectively.

In case of the tetragonal BTO, it is a ferroelectric system with broken inversion symmetry which has the symmetry point group of *4mm*. The electric dipole tensor χ_{ijk} for this point group is [74]

$$\chi_{ijk} = \begin{pmatrix} 0 & 0 & 0 & 0 & \chi_{xxz} & 0 \\ 0 & 0 & 0 & \chi_{xxz} & 0 & 0 \\ \chi_{zxx} & \chi_{zxx} & \chi_{zzz} & 0 & 0 & 0 \end{pmatrix}, \quad (2.24)$$

with 3 nonzero independent elements χ_{xxz}, χ_{zxx}, and χ_{zzz}. The mathematical expressions of the SHG intensity in P-out and S-out configuration coming from a BTO thin film in our measurement geometry (Figure 2.6a) are:

$$\begin{aligned} I_p(2\omega) \propto & (\chi_{zxx} \sin\theta \cos\phi^2 \\ & + (2\chi_{xxz} \cot\theta^2 + \chi_{zxx} \cot\theta^2 + \chi_{zzz}) \sin\theta^3 \sin\phi^2)^2, \end{aligned} \tag{2.25}$$

$$I_s(2\omega) \propto (2\chi_{xxz} \sin\theta \sin\phi \cos\phi)^2. \tag{2.26}$$

According to these analytical expressions, the SHG polar patterns of BTO in P-out and S-out configurations, at $\theta = 50^\circ$ shown in Figure 2.6b are calculated according to Equations (2.25) and (2.26).

In the measurement geometry shown in Figure 2.6, an additional optical beam can be introduced to perform pump-probe experiments (Section 3.2). In Chapter 6, a THG beam at the frequency of 3ω is used to pump our materials, allowing for the measurement of transient changes in the SHG and optical reflectance. This approach enables the investigation of the dynamics of ferroelectric polarization and the electronic structure near the Fermi level of the material of interest.

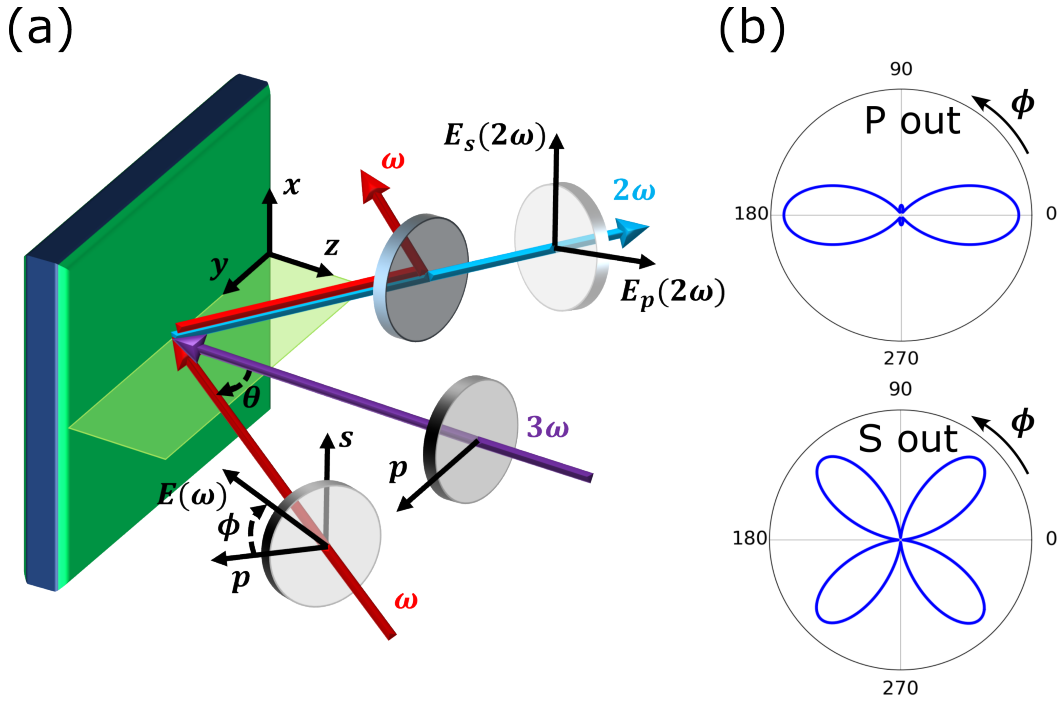

Figure 2.6.: Sketch of optical second harmonic generation polarimetry and simulated polar patterns. Schematic illustration of optical second harmonic generation polarimetry (a) and simulated SHG patterns in P-out and S-out configurations (b). The incident beam at ω and the SHG beam at 2ω are marked as red and blue, respectively. The sample surface and incident plane are indicated as green and light green, respectively. xyz is the Cartesian coordinates of the laboratory in which z is perpendicular to the sample surface and plane yz lies on the incident plane. The angle of incidence is θ defined by the z axis and the incident beam direction. The angular rotation ϕ of the incident polarization is with respect to the incident plane yz. $E(\omega)$ is the incident light field, $E_s(2\omega)$ is the projection of the outgoing SHG light field along the s direction, and $E_p(2\omega)$ is the projection of the outgoing SHG light field along the p direction. The SHG beam and the reflectance of the incident beam are separated by an dichroic mirror. A THG beam at 3ω (marked as violet), which is normally incident to the sample surface, plays a role of an above-bandgap optical excitation. This beam is used in the time-resolved SHG and optical reflectance measurements (Section 3.2).

3. Experimental setups

3.1. X-ray standing waves setup at Diamond Light Source

The static XSW measurement were conducted at the I09 beamline of the synchrotron Diamond Light Source. A soft X-ray beam of around 300 µm × 200 µm was delivered through a plane grating monochromator to the sample. During an XSW measurement, Bragg reflections and photoelectron spectra of the sample were collected simultaneously at a given incident photon energy E_ν. The incident angle of the X-ray beam was fixed at $\theta = 87^\circ$ (Figure 3.1). A Si photodiode with a central through hole was employed to measure the intensity of the diffracted X-ray beam (Figure 3.1). This measurement geometry allowed for recording the (001) Bragg diffractions of the BTO and SRO layers and the substrates in the range of incident photon energy E_ν from 1400 eV to 1700 eV. A Scienta EW4000 electron analyzer equipped with a microchannel plate (MCP) and a charged-coupled device (CCD) was utilized to measure XPS spectra. The overall spectral energy resolution, limited by the X-ray bandwidth, was approximately 400 meV.

As explained in Section 2.3, increasing the exit angle ranges provide increasing depth selectivity. In this XSW setup, the photoelectrons were collected over three different exit angle ranges: γ_1 ($7.8^\circ \pm 5.4^\circ$), γ_2 ($18.5^\circ \pm 5.4^\circ$) and γ_3 ($27.4^\circ \pm 3.6^\circ$). Applying the formulation given in Equation (2.16), we calculate the relative contribution of photoelectrons from Ba and Ti atom within the depth ranging from $\bar{c}_{BTO}$ to $3\bar{c}_{BTO}$ to the surface, where $\bar{c}_{BTO}$ is the average out-of-plane lattice constant. The result is given in Table 3.1. In each angle range, the relative contribution of photoelectrons within the specified depth is considerably larger than that within the remaining portion of the thin film. In addition, the ratios of PE contribution from the specified depth over that from the remaining portion of the thin film are nearly the same over three different exit angle ranges. For Ba atom, the specified PE contribution is in the range

between 64 and 66 %. These values are slightly smaller than those from Ti atom which has the PE contribution within the specified depth ranging from 72 to 73 %, since the IMFP of Ba atom is, in general, longer than that of Ti atom.

Table 3.1.: Relative contributions of Ba and Ti PE intensity at different exit angle ranges. Exit angle range γ_j, depth z range and corresponding relative contribution to the total Ba and Ti PE intensity.

j	$(\gamma_{i,l}, \gamma_{i,h})$ (°)	(z_0, z_i) $[(z_i, \infty)]$	$I^{\mathrm{Ba}}_{(z_0,z_i),\gamma_j}$ $\left[I^{\mathrm{Ba}}_{(z_i,\infty),\gamma_j}\right]$ (%)	$I^{\mathrm{Ti}}_{(z_0,z_i),\gamma_j}$ $\left[I^{\mathrm{Ti}}_{(z_i,\infty),\gamma_j}\right]$ (%)
1	(2.4, 13.1)	$(0, \bar{c}_{BTO})$ $[(\bar{c}_{BTO}, \infty)]$	66 [34]	73 [27]
2	(13.1, 23.9)	$(0, 2\bar{c}_{BTO})$ $[(2\bar{c}_{BTO}, \infty)]$	64 [36]	72 [28]
3	(23.8, 31)	$(0, 3\bar{c}_{BTO})$ $[(3\bar{c}_{BTO}, \infty)]$	65 [35]	73 [27]

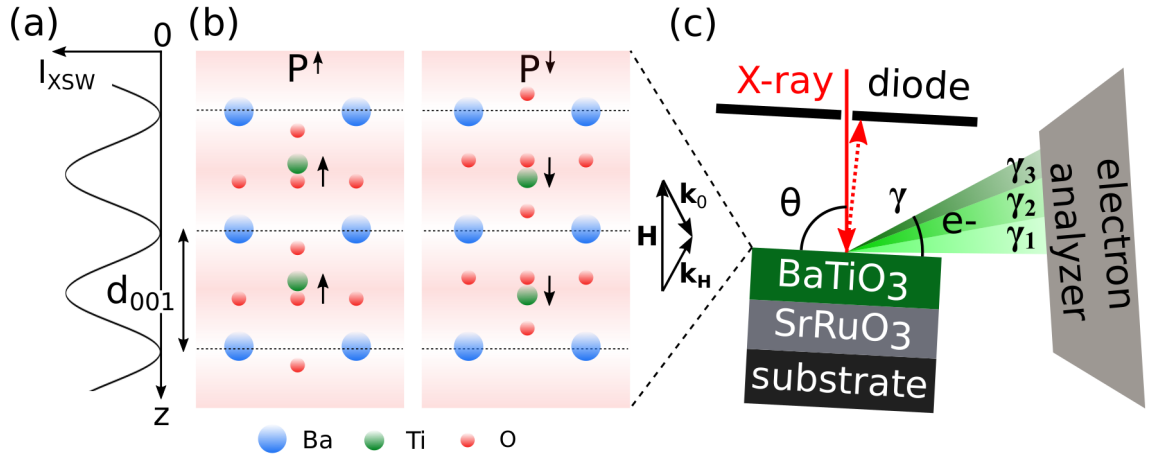

Figure 3.1.: Sketch of the XSW setup at the I09 beamline of the Diamond Light Source. (a) XSW intensity of the BTO (001) Bragg reflection along the z axis, where $z = 0$ represents the sample surface. (b) Side view of the top two BTO unit cells displaying ferroelectric polarizations $P^{\uparrow}$ and $P^{\downarrow}$, along with the Bragg spacing d_{001}. (c) Diagram of the experimental setup (top view) utilized at beamline I09 of the Diamond Light Source, showing the sample, electron analyzer, and photodiode. The photodiode, positioned 10 mm from the sample, featured an Al mask in front to reduce fluorescence background. The Bragg angle θ and the photoelectron exit angle γ are illustrated, along with the photoelectron exit angle ranges γ_1, γ_2, and γ_3, the incident X-ray wavevector $\boldsymbol{k}_0$, and the Bragg-diffracted X-ray wavevector $\boldsymbol{k}_{\boldsymbol{H}} = \boldsymbol{k}_0 + \boldsymbol{H}$.

3.2. Static and time-resolved second harmonic generation setup

A time-resolved SHG setup was developed to study the dynamical changes of the spontaneous polarization of our ferroelectric thin films. The schematic illustration of the time-resolved SHG setup in the SCS Instrument Laser Hutch is given in Figure 3.2. The laser source is a home-built non-colinear optical parametric amplifier (NOPA) with a central wavelength of 800 nm. We pump our samples with 266 nm optical pulses and probe them with 800 nm optical pulses.

In our setup, the beam is split into two parts by a beam splitter with a splitting ratio of 8:92 (Figure 3.2a). The probe arm accounts for 8 % and the pump arm for 92 % of the incoming laser intensity, respectively. The probe beam propagates through an attenuator which is used to adjust the beam intensity. The attenuator contains a half-wave plate which rotates the incident polarization and two thin-film polarizers which transmit *p*-polarized light and reflect *s*-polarized light. In our setup, the outgoing polarization from the attenuator is always *s*-polarized. In the next step, the beam is reflected by two mirrors on a linear translation stage that is used to adjust the time delay between pump and probe. In order to change the polarization of the probe, we use a 800 nm half-wave plate. The probe is finally focused onto the sample surface at oblique incidence with $\theta = 50^\circ$ using a focusing lens. After the sample, the reflectance at 800 nm and SHG at 400 nm are separated by a dichroic mirror which allows the simultaneous measurement of the two beams. Either *s* or *p* polarization component of the SHG signal is selected using an analyzing Glan polarizer (analyzer) corresponding to S-out and P-out configurations (Section 2.4). Next, the beam goes through a bandpass filter around 400 nm and reaches the photomultiplier (PMT), which measures the SHG intensity. Simultaneously, the probe reflectance is measured by a Si photodiode.

The pump beam is also sent through an attenuator to adjust its intensity. The outgoing polarization is *s*-polarized. The conversion from 800 nm to 266 nm is conducted inside a third harmonic generation setup which includes two Beta Barium Borate (BBO) crystals. The first BBO crystal (SHG BBO) is used to generate 400 nm beam from incident 800 nm. The input polarization to this SHG BBO should be *s* and the SHG BBO generates *p*-polarized SHG

which is later turned back to *s*-polarization by a 400 nm half wave plate. The second BBO crystal (THG BBO) is used to combine *s*-polarized 400 nm and *s*-polarized 800 nm to generate *p*-polarized 266 nm. A translational stage is utilized to temporally overlap 400 nm and 800 nm pulses at the THG BBO for the optimal THG conversion. A Si photodiode is installed to monitor the incident intensity of the pump beam. A 266 nm shutter is used to block the pump during static measurements, as well as mechanically chop the pump during pump-probe measurements, in order to halve the pump repetition rate and collect alternatevely pumped and unpumped data. The incident polarization of 266 nm beam is rotated by means of a half-wave plate and the beam is focused at normal incidence on the sample. The spatial overlap at the sample is done by steering a mirror to move the probe spot onto the pump one. A series of cameras are installed to monitor the beam alignment.

The thin film sample is mounted on the sample holder using silver paste. The sample holder can be moved in two orthogonal directions x and y of the Cartesian coordinates of the laboratory (Figure 2.6) by motorized linear stages. In addition, the sample holder can turn around the x axis. The multiple degrees of freedom of the sample holder support the alignment of the sample such that the SHG beam reaches the center of the PMT detector. The beam size is measured by knife-edge measurements at the sample position. The probe spot size at focus is 55 µm × 46 µm and the pump spot size is 165 µm × 311 µm, as measured by knife-edge scans (Section A.8). The spot size of both pump and probe on the sample surface can be adjusted by the translation of focusing lenses along beam axis by linear stages. The knowledge of the beam size is pivotal to determine the incident fluence of the pump (Section A.8) as well as adjust the relative ratio of the pump over probe beam size.

The setup allows us to perform the SHG polar scans in the static regime (without pump) and the pump-probe regime (with pump) at different time delay positions. The beam patterns are illustrated in Figure 3.2b. Laser pulse trains have a repetition rate of 10 Hz. Each train has 35 pulses. We use 113 kHz intratrain repetition rate for the SHG experiment. The pulse durations for the 800 nm probe and 266 nm pump beams are about 50 fs and 70 fs, respectively, resulting in a time resolution of approximately 86 fs. For data acquisition, the optical signals reaching the photodiodes and PMT are converted to voltage signals and digitized. An individual intensity value is calculated as the baseline-subtracted peak integration of all pulses in a train. All mentioned movements of optical apparatuses and sample are motorized using multiple linear stages

and rotation stages. All motors can be remotely controlled via a commercial Beckhoff system and Python-based Karabo framework. To verify the nonlinear characteristics of the signal detected by the PMT, the SHG intensity is measured as a function of the 800 nm probe pulse energy, and the data is well-represented by a quadratic function (Figure 3.3).

In static measurements, the 266 nm shutter is closed to block the 266 nm pump. The 800 nm half-wave plate is rotated with the speed of 2° per second, while the SHG intensity is measured continuously. For the S-out configuration, the Glan polarizer axis is set to 90° relative to the incident plane to measure the *s*-polarized SHG signal. For the P-out configuration, the Glan polarizer axis is set to 0° with respect to the incident plane to measure the *p*-polarized SHG signal. The typical duration of one static scan is 12 minutes.

In addition, simultaneous time-resolved measurement of SHG and optical reflectance can be performed with this setup. The pump-probe SHG measurement is employed to investigate the change in SHG intensity at a specific point of the polar patterns, as well as the change of the entire polar pattern over time upon the incidence of 266 nm pump. In the pump-probe reflectance measurement, the photoinduced change of 800 nm reflectance as a function of time is measured. In a pump-probe measurement, the 266 nm shutter operates at the frequency of 5 Hz. This allows a half of the probe trains to be pumped and another half to be unpumped (Figure 3.2b). The linear stage at the probe arm is translated at the speed of 0.02 mm/s to tune the time delay between the pump and probe pulse. During the translation of the linear stage, the SHG intensity and 800 nm reflectance are measured continuously.

The 400 nm light that is not converted to 266 nm at the THG BBO may contribute to the SHG background measured by the PMT. This background overlaps with the pure SHG signal. To overcome this limitation, we cover the area around the PMT and the Si photodiode with black fabric curtains and black coated aluminum sheets. Furthermore, the level of background SHG is measured after every pump-probe scan. In this background measurement, the 800 nm probe is blocked by the 800 nm shutter, while the 266 nm shutter operates at 5 Hz. The pumped and unpumped background is measured for 1 minute and their average values are calculated. The pure SHG intensity I_{SHG} from the sample is the subtraction between measured SHG intensity $I_{SHG}^{measured}$ during pump-probe measurement and the average background SHG $I_{SHG}^{background}$ during the background measurement, i.e., $I_{SHG} = I_{SHG}^{measured} - I_{SHG}^{background}$. Quick

static SHG polar patterns are measured before and after every pump-probe measurement to monitor the occurrence of possible sample damage (Section A.14). The fact that two polar patterns are overlapped indicates the absence of sample damage. These measurements typically last 3 minutes.

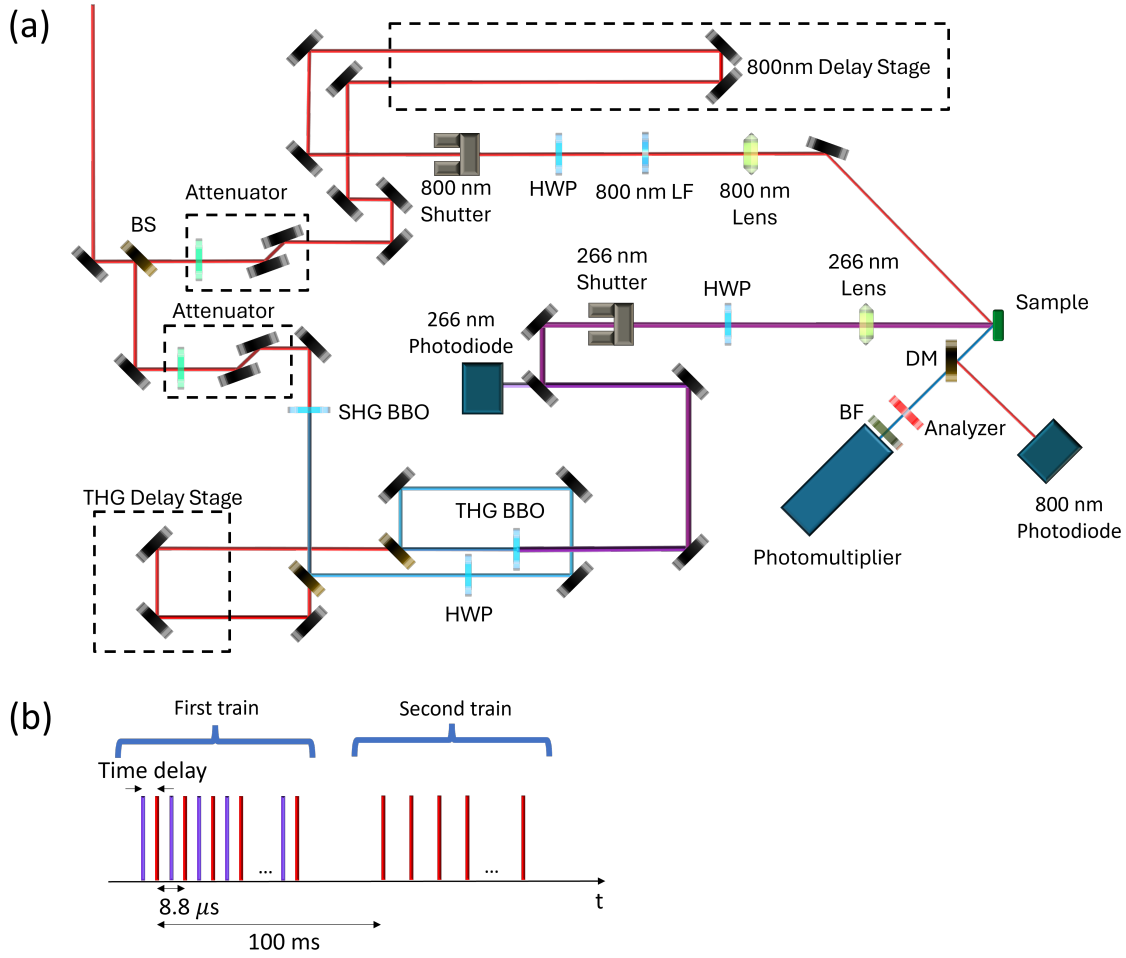

Figure 3.2.: Scheme of time-resolved SHG and optical reflectance setup. (a) Sketch of the experimental setup. BS: Beam splitter, HWP: Half-wave plate, LF: Longpass filter, DM: Dichroic mirror, BF: Bandpass filter. (b) Laser pulses sequence. The red lines indicate the probe pulses. The violet lines indicate the pump pulses. The intratrain repetition rate is 113 kHz, corresponding to the temporal interval of 8.8 µs between two consecutive pulses. The train repetition rate of the probe is 10 Hz, corresponding to the time interval of 100 ms between two consecutive trains. Because the train repetition rate of the pump is reduced to 5 Hz by the 266 nm shutter, only half of the probe pulses is pumped, while the other half is not pumped.

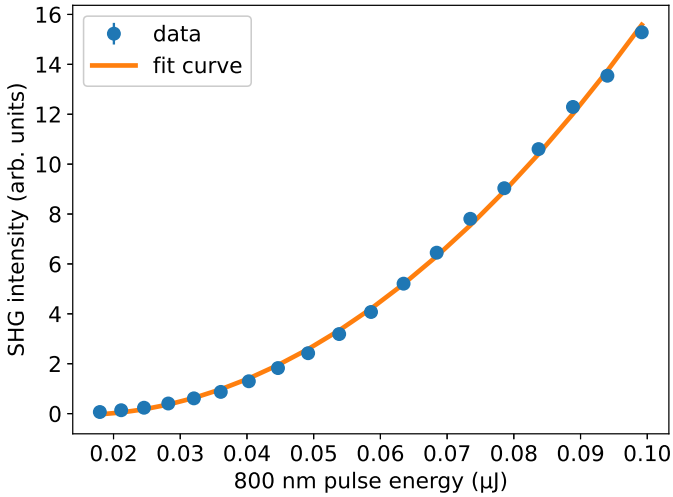

Figure 3.3.: Characterization of the SHG intensity. The SHG intensity measured as a function of the 800 nm probe pulse energy and its quadratic fit.

3.3. Time-resolved X-ray diffraction setup at SCS

Time-resolved X-ray diffraction measurements of ferroelectric thin films were performed at the Spectroscopy and Coherent Scattering instrument (SCS) of the European XFEL (EuXFEL). The experiments employ the same 266 nm optical laser mentioned in Section 3.2 as pump and the free electron laser (FEL) as probe. The FEL has the same pulse pattern as the optical pump (Figure 3.2b). The generation of the FEL radiation is achieved using the undulator in the self-amplified spontaneous emission (SASE) 3 tunnel. In this section, we describe how the FEL beam is transported to the sample from the source and how the experiment is performed.

The scheme of the FEL beam transport in the SASE3 tunnel and SCS instrument in monochromatic mode is given in Figure 3.4. The initial pulse energy is 1.5 mJ. The FEL pulses are attenuated by a nitrogen (N_2) gas volume with variable pressure (GATT). The transmission of the GATT is adjusted to be around 0.5%. Next, the beam transport is carried out by multiple X-ray optics at grazing incidence and under ultra-high vacuum conditions. The first two mirrors M1 and M2 are used to remove the spontaneous radiation and filter higher harmonics of FEL radiation by adjusting the grazing incident angle between 6 and 20 mrad depending on the photon energy. Specifically, M2 is a deformable mirror which can minimize the horizontal beam size at the horizontal slits (HS). The elliptic cylindrical pre-mirror M3 provides a vertical beam focus at the exit slits (ES). The monochromatization of the beam is performed using a variable line spacing grating (G) with 50 lines/mm in first diffraction order and the ES gap of 100 µm. The FEL beam is horizontally steered to the SCS hutch using the distribution mirror M5 with a grazing incident angle of 9 mrad. An X-ray gas monitor detector (XGM) after the ES is employed to measure the FEL pulse energy based on atomic photoionization processes. An electric field is used to accelerate the produced ions from the FEL induced ionization of rare gas atoms in the XGM chamber. The collision of these ions with a large Faraday cup electrode generates a current which is proportional to the FEL pulse energy [75]. These photo-ion currents are amplified and measured with avalanche multiplication using a huge aperture open multiplier (HAMP). In our experiment, the FEL pulse energy after the ES is 15 nJ, as measured by the XGM. The Kirkpatrick-Baez (KB) mirror system, which includes a horizontal (HFM) and a vertical (VFM) focusing mirror after the XGM, is utilized to adjust the beam size at the first interaction point (IP1),

where the target sample is located, in both horizontal and vertical directions independently [76]. A flat vertical deflecting mirror (VDM) is located between HFM and VFM to keep the beam horizontal after the KB mirrors.

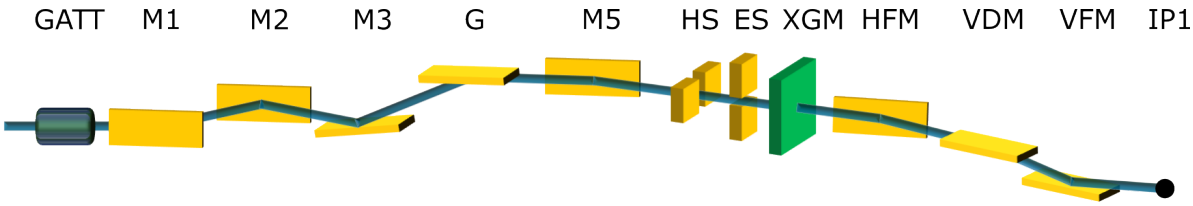

Figure 3.4.: Scheme of SASE3 and SCS beam transport. Schematic illustration (not in scale) of the optics in SASE3 tunnel and SCS Instrument in monochromatic mode, as well as gas attenuator (GATT) and X-ray gas monitor detector (XGM).

In the time-resolved X-ray diffraction experiment, the FEL beam is incident to the sample at around 86° and with a focal size of 140 µm × 100 µm (measured by knife-edge scans, Section A.8). The FEL beam has 25 fs nominal pulse duration and 650 meV energy resolution [77, 78]. The (001) Bragg diffraction of the FEL beam from the sample is collected in the energy range from 1.5 to 1.6 keV using a Si avalanche photodiode (APD, model SAR3000G1X, Laser Components). Experiments are performed in the X-ray resonant diffraction (XRD) endstation (Figure 3.5). The APD signal is converted to a voltage signal and digitized. Similar to the calculation of measured optical intensity in a train, the average diffracted intensity of the FEL is computed as the baseline-subtracted peak integration of all pulses per train. The APD is protected from the pump laser using a filter composed of 400 nm Ti, deposited on 200 nm polyimide. The above-bandgap optical excitation is provided by femtosecond 266 nm laser pulses which is generated by the THG from 800 nm that is used in the time-resolved SHG and optical reflectance measurement (Section 3.2). The incident laser beam is at the angle of 85° relative to the sample surface with p polarization. The incident pump fluences of 1.4 and 2.7 mJ/cm^2 at the sample are chosen. The optical beam size at the sample is 330 µm × 240 µm. The time delay between the FEL and the optical pump is corrected by the bunch arrival monitors (BAM) values (Section A.10). Two types of time-resolved X-ray diffraction experiment are conducted. The first one is the time delay scan at a fixed photon energy E_ν. The second one is the photon energy scan from 1.5 keV to 1.6 keV at a fixed pump-probe delay t. In the energy scan, the peak of the FEL spectrum remains at the desired photon energy by a simultaneous

movement of the monochromator grating and the undulators gap. The energy scans at different t measure the average out-of-plane lattice parameter c as the function of time which is calculated as the center-of-mass of BTO diffraction peak (Section A.4).

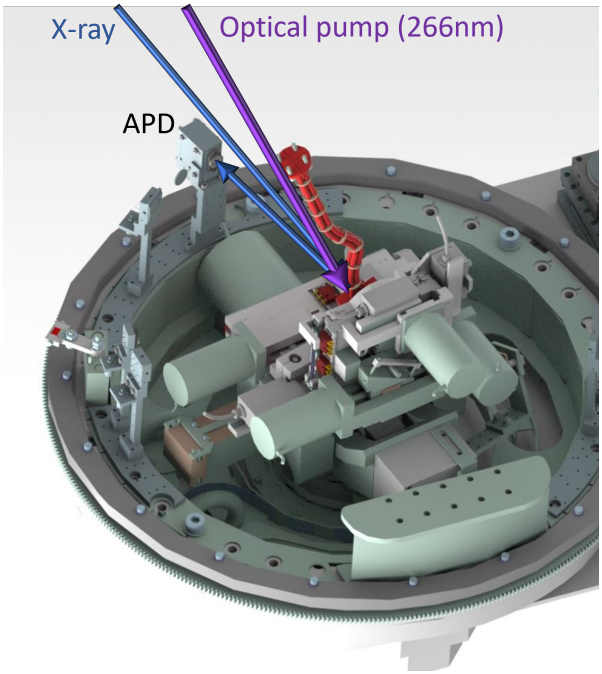

Figure 3.5.: Sketch of time-resolved XRD setup at the SCS Instrument. CAD representation of the inner experimental chamber used for tr-XRD experiments. The blue arrow indicates the FEL beam impinging on the sample and diffracted to the APD. The violet arrow indicates the optical pump beam.

4. $BaTiO_3$ thin films: Fundamentals and characterization

4.1. Ferroelectric $BaTiO_3$ - Basic properties

4.1.1. From dielectric to ferroelectric materials

Dielectrics are insulators with significantly low density of free charge carrier. In these materials, an external electric field can induce the spatial separation of the positive and negative charges. As a result, these materials can be polarized. This property of dielectrics plays an important role in charge storage devices [79, 80]. Dielectric materials can be piezoelectric, pyroelectric, and ferroelectric (Figure 4.1). Piezoelectric materials are dielectric materials where mechanical stress and electric polarization are coupled. In these materials, a mechanical deformation gives rise to an electric polarization and vice versa [81]. Piezoelectrics with the permanent polarization are pyroelectrics. If this permanent polarization is reversible under external electric field, the material is a ferroelectric [5, 82]. Thus, ferroelectrics have both switchable polarization as well as the coupling of mechanical deformation and electric polarization. From the symmetry point of view, all ferroelectrics have broken inversion symmetry, which is characterized by the non-centrosymmetric point groups [47, 70].

In ferroelectrics, the dependence of electric polarization and external electric field is characterized by a hysteresis loop (Figure 4.2). A ferroelectric material can reverse its polarization direction when the external electric field, applied in the antiparallel direction, overcomes a certain threshold. This threshold amplitude of applied electric field is called the coercive field E_c. The polarization does not go to zero when the applied electric field decreases to zero, but stays at a certain amplitude called remanent polarization P_r at zero field. The polarization only disappears when the external electric field decreases further to a certain negative values. The linear extrapolation to zero field of the polarization at high fields is governed by $P = P_s + \epsilon_0 \chi E$ where P_s is

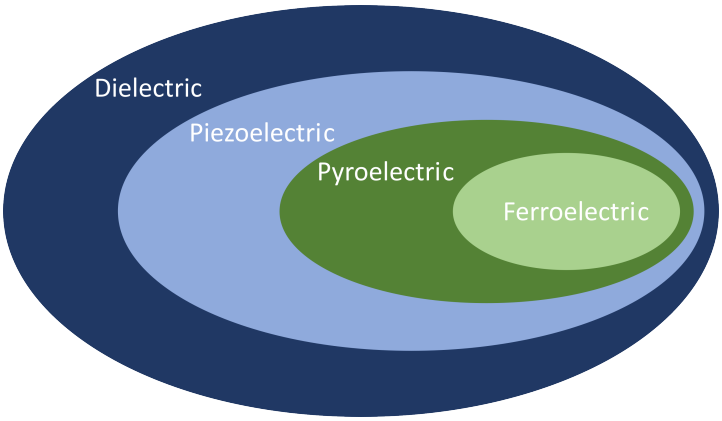

Figure 4.1.: Classification of dielectric materials. Dielectric materials are insulators that exhibit electrical polarizability. Piezoelectric materials are dielectrics that couple mechanical stress with electric polarization. Pyroelectric materials are piezoelectrics that possess permanent polarization. Ferroelectric materials are pyroelectrics with switchable polarization. While all ferroelectrics are dielectrics, not all dielectric materials are ferroelectric.

the spontaneous polarization, ϵ_0 is the permittivity of vacuum and χ is the dielectric susceptibility. The difference between P_r and P_s is large in polycrystals but negligible in single crystals. In addition, a typical characteristic of ferroelectric materials is the possible formation of domains [83]. These are the regions of the crystal where homogeneously oriented order parameter such as electric polarization and strain exists. These domains are separated from each other by a boundary called domain wall. They are labeled by the difference in polarization orientation between two adjacent domains. For instance, a 180° domain wall splits two domains with opposite polarization.

4.1.2. Structural and electronic properties of $BaTiO_3$ single crystal

$BaTiO_3$ (BTO) is a perovskite ferroelectric material with three structural phase transitions [5]. The first transition from cubic to tetragonal structure happens at 120°C (393K) which is known as the Curie point of the BTO single crystal. The second one from tetragonal to orthorhombic at 5°C (278K), and the last one from orthorhombic to rhombohedral at -90°C (183K) (Figure 4.3). In the unit cell of BTO, the position of each atom is defined by its coordinates with

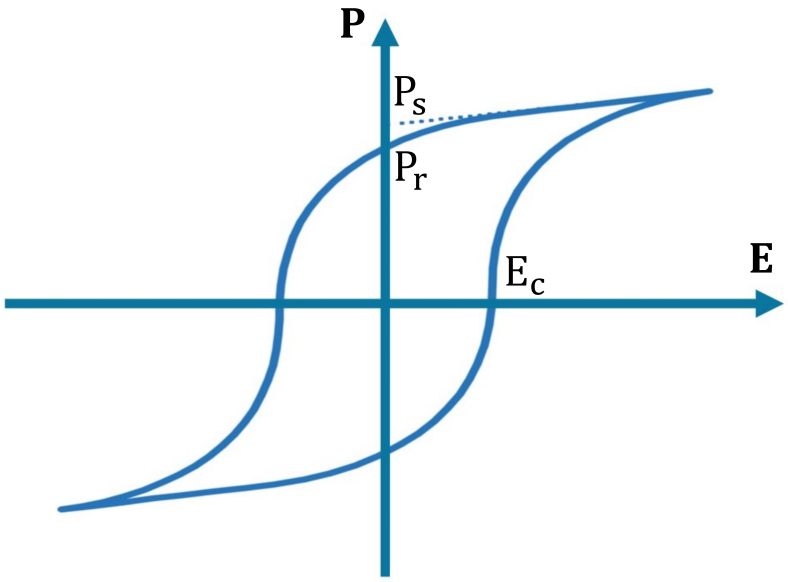

Figure 4.2.: Typical P-E hysteresis loop of ferroelectric materials. The external electric field amplitude is denoted as E. P is the induced polarization of the ferroelectric material exposed to the external field E. E_c is the coercive field defined by the intersection between the hysteresis loop and the E axis. P_r is the remnant polarization defined by the intersection between the hysteresis loop and the P axis. P_s is the spontaneous polarization determined by the linear extrapolation to $E = 0$ of P at high E.

respect to the origin of the unit cell. The origin of the unit cell (0, 0, 0) is typically chosen as a Ba atom. In the cubic phase, BTO is paraelectric with the simple cubic structure ($a = b = c \approx 4$ Å), which is centrosymmetric (space group Pm3m). In this phase, Ba atoms are located at the eight vertices of the unit cell, the Ti atom is located at the body center and O atoms are located at the six face centers of the unit cell. When the BTO single crystal transitions from the cubic phase to the tetragonal phase, the out-of-plane lattice parameter c is lengthened, while in-plane lattice parameters a and b are reduced. In the tetragonal phase, the structure is non-centrosymmetric (space group P4mm) with lattice parameters c = 4.036 Å and a = b = 3.992 Å (Figure 4.4b) [5]. In this phase, according to neutron scattering data, the displacements of individual atoms relative to the symmetrical positions z^{sym} in the cubic phase along the c-axis is given in Table 4.1 for the upward polarization state [5].

In this material, ferroelectricity originates from the hybridization between

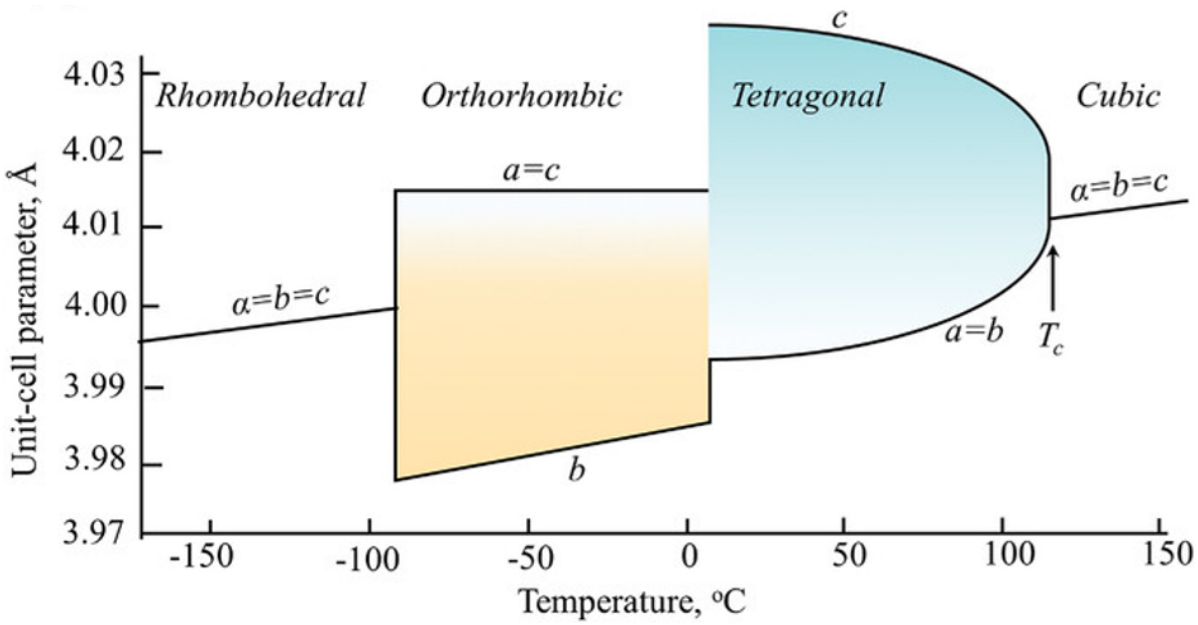

Figure 4.3.: Structural phase transitions of the BTO single crystal. The first transition from cubic to tetragonal structure occurs at 120°C (393K), which is known as the Curie temperature of the BTO single crystal. The second transition from tetragonal to orthorhombic occurs at 5°C (278K), and the final transition from orthorhombic to rhombohedral occurs at -90°C (183K). This figure is adapted from [84].

the empty 3d states of the Ti^{4+} cation and the occupied 2p states of the O^{2-} anion. In this case, the spontaneous polarization is associated with the displacement of Ti^{4+} atoms relative to the center of the oxygen octahedra. This atomic displacement leads to inversion symmetry breaking and asymmetric charge distribution, which stabilizes ferroelectric state according to the pseudo-Jahn-Teller effect [85]. Real-time time-dependent density functional theory (RT-TDDFT) predicts the band structure of BTO as a function of time upon above-bandgap optical excitation [26]. The difference in band structure between ground and excited state is illustrated in Figure 4.5. In the ground state, the valence band mainly consists of occupied O 2p levels, while the conduction band consists of unoccupied Ti 3d levels. Upon above-bandgap excitation, electrons are transferred from the valence band to the conduction band. This carrier excitation process introduces directional forces on the Ti and O atoms and forces them to move opposite to the original ferroelectric displacement [86]. This leads to the formation of opposite ferroelectric polarization within a few hundred femtoseconds, if a sufficient number of carriers are excited to the

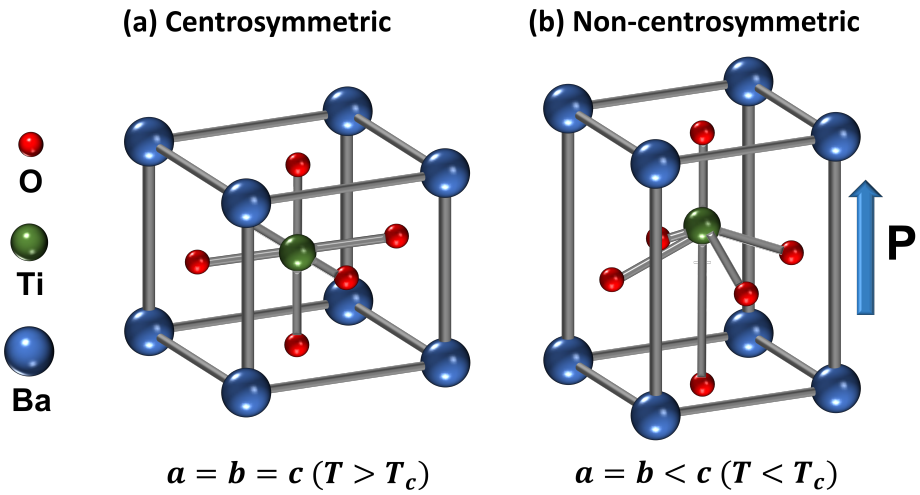

Figure 4.4.: The unit cells of a BTO single crystal in the cubic and tetragonal phase. Comparison between the centrosymmetric unit cell in the cubic (paraelectric) phase (a) and the non-centrosymmetric unit cell in the tetragonal (ferroelectric) phase (b). The atomic displacements are not in scale.

conduction band. This transient state of ferroelectric polarization eventually relaxes upon the recombination of the photoexcited carriers (electrons and holes) in much longer timescale (beyond the RT-TDDFT calculation time) [26].

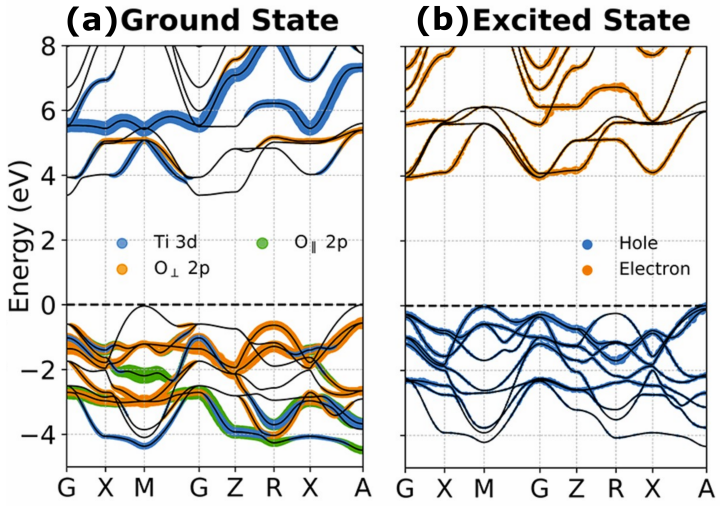

Figure 4.5.: DFT calculations of BTO band structure in the ground and excited state. (a): The blue solid dots indicate Ti 3d orbitals, the orange and green solid dots indicate O 2p orbitals in the ground state. The $O_\perp$ denotes the equatorial O atoms of the unit cell and the $O_\parallel$ denotes the O atoms lying along the *c* axis. (b): BTO band structure 150 fs after optical excitation. The blue solid dots indicate the excited holes and the orange solid dots indicate the excited electrons in the excited state. This figure is adapted from [26].

Table 4.1.: Atomic positions within the unit cell of a BTO single crystal in the tetragonal phase. The coordinates of atoms *i* (atomic positions) within the unit cell of tetragonal BTO single crystal with lattice parameters c = 4.036 Å and a = b = 3.992 Å [5]. The displacement of atoms relative to the symmetrical positions along the in-plane directions is 0 ($x_i = x_i^{sym}$ and $y_i = y_i^{sym}$)

Element *i*	x_i (Å)	y_i (Å)	z_i (Å)	z_i^{sym} (Å)	Δz_i (Å)
Ba	0.0	0.0	0.0	0.0	0.0
Ti	0.5a	0.5a	0.513c	0.5c	0.013c
O	0.0	0.5a	0.487c	0.5c	-0.013c
O	0.5a	0.0	0.487c	0.5c	-0.013c
O	0.5a	0.5a	-0.023c	0.0	-0.023c

4.1.3. $BaTiO_3$ epitaxial thin films

In Section 4.1.2, we provide an overview of the fundamental properties of BTO single crystals. Now, we move to the unique properties of BTO thin films. A thin film of BTO when epitaxially deposited on a specific substrate can exhibit a given strain due to the mismatch of the in-plane crystal lattice parameters. This in-plane strain is defined as the following

$$\epsilon_a = \frac{(a_\mathrm{f} - a_\mathrm{b})}{a_\mathrm{b}}, \tag{4.1}$$

where a_f is the in-plane lattice parameter of the strained thin film and a_b is the lattice parameter of the bulk crystal. A negative strain refers to in-plane compressive strain, whereas a positive strain indicates in-plane tensile strain. The strain induced by the substrate to the thin film provides unique properties that are not intrinsic to the corresponding bulk material. A negative strain increases the transition temperature between the ferroelectric and paraelectric phase (Curie temperature T_c), and the remanent polarization of BTO thin films [6]. The changes in the physical properties of strained BTO thin films around ferroelectric transition can be described by the phenomenological Landau theory [87]. This theory predicts the dependence of T_c on the in-plane strain ϵ_a

$$T_c = \vartheta + 2\varepsilon_0 C \frac{2Q_{12}}{s_{11} + s_{12}} \epsilon_a, \tag{4.2}$$

where ε_0 is the permittivity of vacuum, C is the Curie constant and ϑ is the Curie temperature of strain-free ferroelectric crystal. The second rank tensor elements Q_{ij} are the electrostrictive coefficients which stand for the mechanical deformation of materials along i direction under the application of an external electric field along j direction. The second rank tensor elements s_{ij} are the elastic compliances which are the strain along i direction induced in a unit of applied stress along j direction in piezoelectric materials. In Equation (4.2), $i = 1, 2, 3$ is representative of the three orthogonal directions x, y, z, thus, the plane 12 is parallel to the surface of the thin film. It can be seen that, the transition point is shifted to higher temperature as the absolute value of in-plane compressive strain ϵ_a increases. In the case of BTO, the coefficients in Equation (4.2) are: $Q_{12} = -0.034 m^4/C^2$ [88]; $s_{11} = 9.1 \times 10^{-12} m^2/N$, $s_{12} = -3.2 \times 10^{-12} m^2/N$ [87, 89]; $C = 1.37 \times 10^5$ [6]; $\vartheta = 120^\circ C$ [5].

Figure 4.6 shows the changes of out-of-plane and in-plane lattice parameters of BTO thin films grown on $DyScO_3$ (DSO) and GSO substrates as a function

of temperature [6]. The Curie temperature is different in the thin films grown on different substrates because of the different in-plane strain (Equation (4.2)). The thin film grown on DSO has $T_c \approx 680^\circ C$ and that grown on GSO has $T_c \approx 420^\circ C$. In the ferroelectric phase, as the temperature increases, the out-of-plane lattice parameter c initially shows a slight increase, followed by a rapid decrease near the Curie point, and finally a significant increase above the Curie point. In contrast, the in-plane parameters increase monotonically with rising temperature (Figure 4.6). The increase [decrease] of c with increasing temperature indicates a positive [negative] out-of-plane linear expansion coefficient. The concept also applies to the in-plane parameters and the corresponding in-plane linear expansion coefficients. The tetragonality c/a remains larger than 1 above the Curie temperature. Therefore, we do not have a perfect cubic phase ($a = b = c$) even above the Curie temperature.

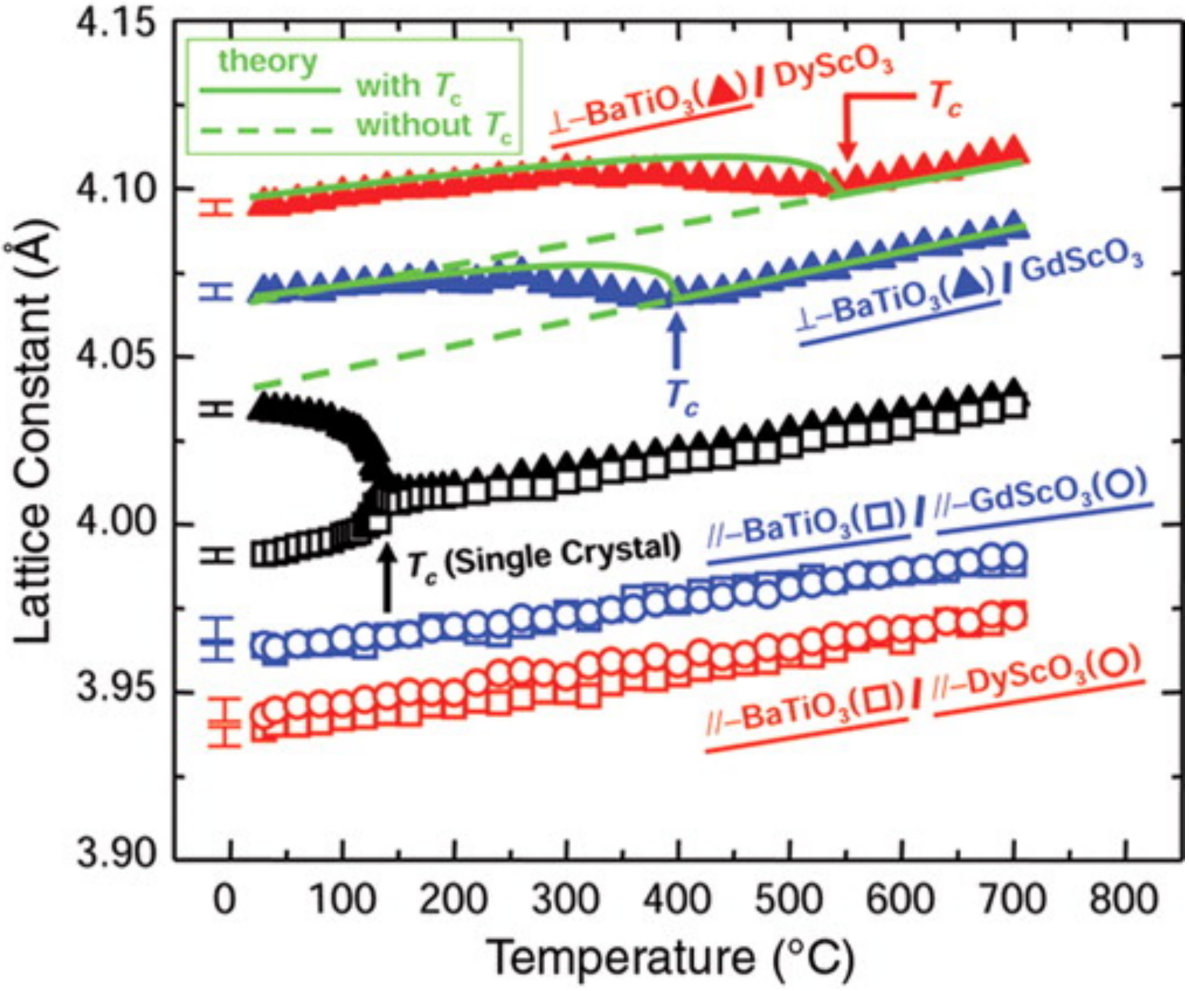

Figure 4.6.: Temperature dependence of the lattice parameters of BTO single crystal and differently strained BTO thin films. The red solid triangles indicate the out-of-plane lattice constant of BTO grown on DSO substrate, the blue solid triangles indicate the out-of-plane lattice constant of BTO grown on GSO substrate and black solid triangles indicate the out-of-plane lattice constant of BTO single crystals. The empty squares and circles indicates the in-plane parameters of BTO grown on DSO substrate (red) and BTO grown on GSO substrate (blue). The figure is adapted from [6].

4.2. Sample overview

Four different BTO ferroelectric thin films were grown on three different substrates DSO, GSO, and $SmScO_3$ (SSO) with (001) orientation according to the pseudocubic notation [90]. A SRO thin film is grown in between BTO and substrate serving as the bottom electrode. The BTO thin films grown on DSO and SSO substrates are named as BTO/SRO/DSO and BTO/SRO/SSO, respectively. In addition, there are two BTO thin films grown on GSO substrate which are labeled as BTO/SRO/GSO and BTO/SRO*/GSO. The summary of our thin film samples and their acronyms is given in Table 4.2. The thickness of BTO and SRO thin films in BTO/SRO/DSO, BTO/SRO/GSO, and BTO/SRO/SSO samples were measured using grazing x-ray reflectivity, while theta-2-theta diffraction measurement was used to determine the thickness of BTO and SRO thin films in the BTO/SRO*/GSO sample. The average in-plane strain of thin films was determined by reciprocal space mapping (RSM) around the (-103) substrate Bragg peak. The average polarization orientation of as-grown BTO thin films was determined by piezoresponse force microscopy (PFM). This technique was also employed to verify that all samples were electrically switchable. Lastly, the AFM image analysis reveals a root mean square surface roughness (S_{RMS}). In the next sections, the working principle of each technique and characterization results are presented.

Table 4.2.: Film thickness, surface rougness and polarization of the samples under study. Table of acronyms, thicknesses of BTO and SRO layers, the root mean square surface roughness, and the average polarization direction P of BTO thin film of all samples investigated in this work.

Acronym	Sample	t_{BTO} (nm)	S_{RMS} (nm)	t_{SRO} (nm)	P
BTO/SRO/DSO	$BaTiO_3/SrRuO_3/DyScO_3$	20	0.95	26	↓
BTO/SRO/GSO	$BaTiO_3$/24 nm $SrRuO_3/GdScO_3$	37	0.77	24	↑
BTO/SRO/SSO	$BaTiO_3/SrRuO_3/SmScO_3$	35.5	0.81	20	↑
BTO/SRO*/GSO	$BaTiO_3$/47 nm $SrRuO_3/GdScO_3$	34.5	1.57	47	↑

4.3. Sample growth

Epitaxial BTO thin films were synthesized using pulsed laser deposition. Ceramic targets of SRO and BTO, positioned 8 cm from the substrates, were ablated with a KrF excimer laser (λ = 248 nm, fluence 5.4 J cm^{-2}, 2 Hz repetition rate). The deposition occured in an O_2 atmosphere with an oxygen partial pressure of pO_2 = 100 mTorr, at temperatures of 908 K for SRO and 973 K for BTO. The samples were cooled at a rate of 3 K min^{-1} in an environment of saturated O_2 ($pO_2 = 10^4$ mTorr) to prevent oxygen vacancy formation.

Our rare earth (RE = Dy, Gd, Sm) scandate substrates ($REScO_3$) were not etched, leading to a mixed termination of REO and ScO_2 [91, 92]. Despite the substrate termination, the SRO layer is expected to terminate with SrO due to the high volatility of RuO_2 [92, 93]. The termination of the top BTO layer is influenced by the oxygen partial pressure during deposition [94, 95]. In our samples, deposited at 973 K and pO_2 = 100 mTorr, the BTO thin films exhibit a mixed termination of BaO and TiO_2 [94].

4.4. Thickness and roughness measurements

The thickness of the BTO and SRO thin films was determined by grazing X-ray reflectivity [96] and theta-2-theta diffraction measurement [60, 97, 98] using a PANalytical X'Pert Pro diffractometer.

The measured reflectivity $R_g(q)$, shown in Figure 4.7, can be expressed as

$$R_g(q) = R_F(q)\left|\frac{1}{\rho_s}\int_{-\infty}^{\infty}\frac{d\rho_e(z)}{dz}\exp\left(-\mathrm{i}qz\right)dz\right|^2, \tag{4.3}$$

where R_F and ρ_e are the Fresnel reflectivity and the electron density of the substrate, respectively [99]. In Equation (4.3) R_g is given as a function of the wavevector transfer $q = (4\pi \sin\theta)/\lambda$, where θ is the incident angle of X-ray and $\lambda = 1.54$ Å is the wavelength of Cu Kα incident radiation. In practice, thin film thicknesses are calculated as follows. First, R_F is computed using the Parratt formalism [96]. Second, the Fourier inversion of R_g/R_F offers the autocorrelation of the derivative of the electron density ρ_e' as a function of z. This function shows peaks in correspondence of the interfaces, where ρ_e' is largest, thereby offering the thicknesses of layers above the substrate. In the BTO/SRO/DSO, BTO/SRO/GSO and BTO/SRO/SSO samples, BTO has

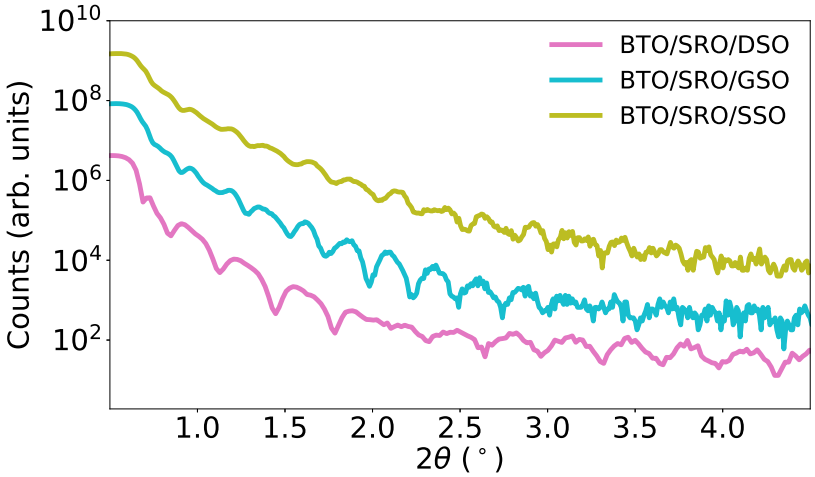

Figure 4.7.: Grazing X-ray reflectivity of BTO thin films. Grazing X-ray reflectivity data of as-grown samples employed to derive the thickness of the BTO and SRO thin films in BTO/SRO/DSO, BTO/SRO/GSO, and BTO/SRO/SSO samples.

thickness 20 nm, 37 nm, 35.5 nm and SRO has thickness 26 nm, 24 nm, 20 nm, respectively (Table 4.2). In addition, based on AFM images taken over an area of $3.9 \times 3.9\,\mu m^2$, the root mean square surface roughness (S_{RMS}) of the BTO/SRO/DSO, BTO/SRO/GSO, and BTO/SRO/SSO samples was on average 0.84(8) nm (Table 4.2). The S_{RMS} of the BTO/SRO*/GSO was measured to be around 1.57 nm (Table 4.2).

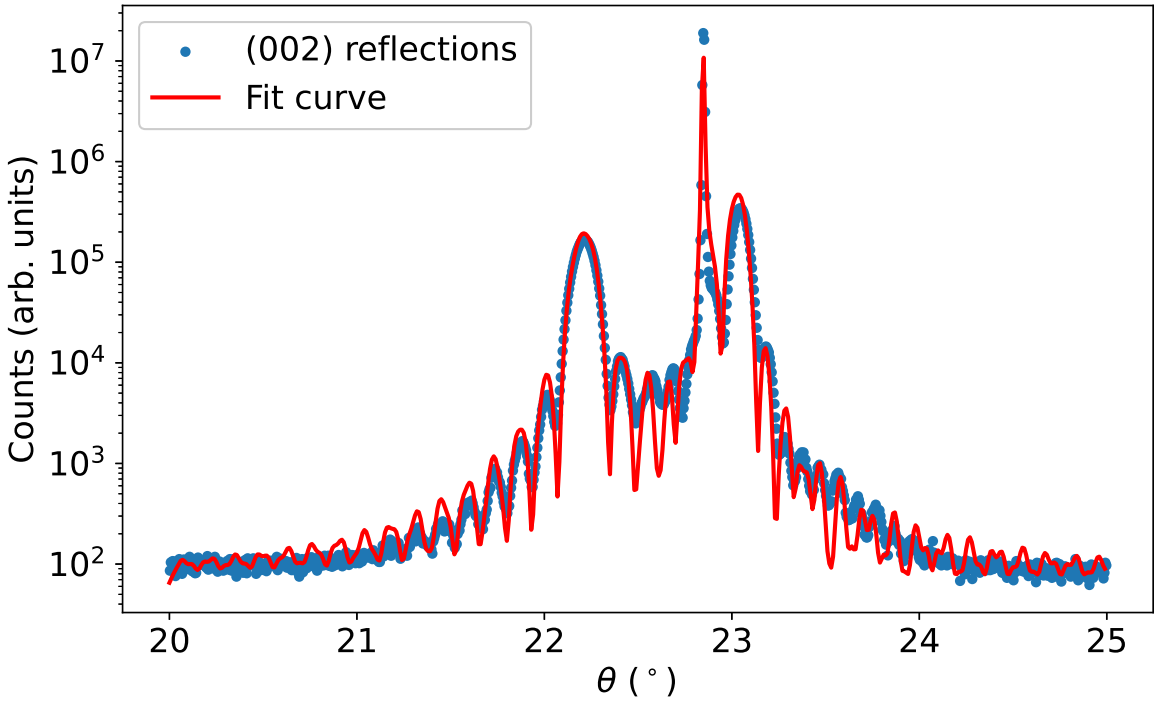

Figure 4.8.: (002) Bragg reflections of the BTO/SRO*/GSO sample. (002) Bragg reflections (blue points) and corresponding fit curves (red solid line) of as-grown samples used to determine the thickness of the BTO and SRO thin films in BTO/SRO*/GSO sample.

To determine the thickness of BTO/SRO*/GSO sample, theta-2-theta measurements, using PANalytical X'Pert Pro diffractometer, were performed. The (002) Bragg peaks of the BTO, SRO, and substrate are shown in Figure 4.8. The mathematical model of energy dependent X-ray intensity $R(E_\nu, z)$ given in Section 2.2 can be expressed as $R(\theta, z)$, as a function of the angle θ [100]. The resulting model can be used to fit the experimental diffraction peaks assuming that each layer has a unique out-of-plane lattice constant with the thicknesses of BTO and SRO as fit parameters. The reasonably good fit of the experimental Bragg peaks in Figure 4.8 provides the thickness of BTO and SRO to be 34.5 nm and 47 nm, respectively (Table 4.2).

4.5. Reciprocal lattice mapping

Reciprocal lattice mapping is an X-ray scattering method that provides information about both in-plane and out-of-plane lattice parameters of the thin films and their substrates [101–104]. The goal is to fully map the diffraction intensity in the reciprocal lattice space (Q space). The scheme of this technique is shown in Figure 4.9. The incident X-ray beam $\mathbf{k}_{\text{in}}$, making an angle ω with the sample surface, fulfills the Bragg condition corresponding to the aforementioned diffracting planes and leads to the outgoing X-ray beam $\mathbf{k}_{\text{out}}$ that makes an angle $\pi - 2\theta$ with the incident beam. The coincidence between Ewald sphere around the starting point of $\mathbf{k}_{\text{in}}$ and a reciprocal lattice point indicates the fulfillment of Bragg condition. In this measurement, the Bragg reflection is obtained in series of one dimensional radial scans. The $2\theta - \omega$ scans are performed such that only the amplitude of the momentum transfer vector $\Delta\mathbf{K} = \mathbf{k}_{\text{out}} - \mathbf{k}_{\text{in}}$ is varied, whereas its direction stays unchanged. Conversely, the ω scans are conducted such that only the direction is scanned, but the amplitude stays constant. Obviously, ω scans involve only the rotation of thin film, while $2\theta - \omega$ scans require the rotation of the thin film and the detector simultaneously in which the rotation of the detector doubles that of thin film. The combination of these scans provides the 2D map of X-ray reflection in the extended reciprocal space. The projection of the reciprocal lattice vector along the out-of-plane and in-plane directions are

$$Q_z = 2|\mathbf{k}_0| \cdot \sin(\theta) \cdot \cos(\omega - \theta), \tag{4.4}$$

$$Q_x = 2|\mathbf{k}_0| \cdot \sin(\theta) \cdot \sin(\omega - \theta), \tag{4.5}$$

with $|\mathbf{k}_0| = 2\pi/\lambda$, where λ is the wavelength of X-ray beam.

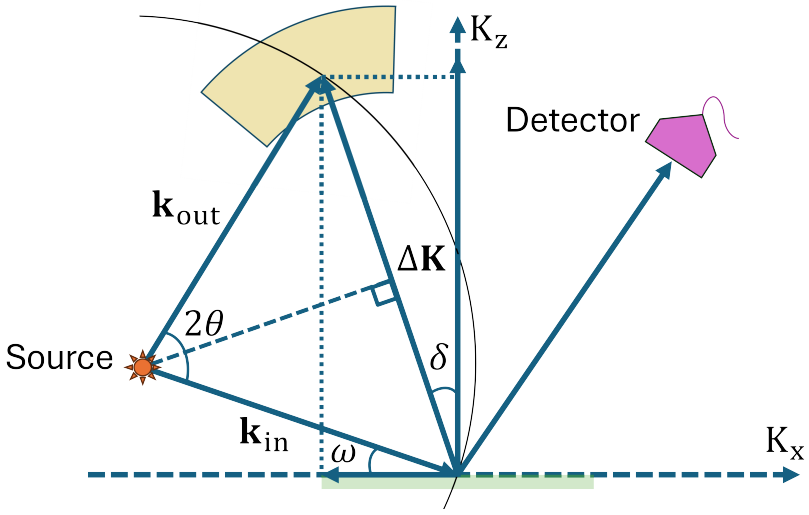

Figure 4.9.: Schematic illustration of reciprocal lattice mapping. 2θ is the angle between the incident wave vector $\mathbf{k}_{in}$ and the outgoing wave vector $\mathbf{k}_{out}$. ω is the angle between the incident wave vector $\mathbf{k}_{in}$ and the in-plane axis K_x. $\delta = \theta - \omega$ is the angle between the momentum transfer vector $\Delta\mathbf{K}$ and the normal axis K_z.

Figure 4.10 shows X-ray reciprocal lattice maps of the BTO thin films around the (-103) substrate Bragg peak, measured by a PANalytical X'Pert Pro diffractometer. The diffraction peaks of the substrates have narrow intensity distribution with high intensity peak, while the intensity distributions of BTO and SRO layers are weaker and broader. This is because the substrates have larger thickness and higher crystalinity than BTO and SRO layers. Reciprocal lattice parameters $\overline{Q}_x$ and $\overline{Q}_z$ of the intensity peaks are related to the real space in-plane and out-of-plane lattice parameters, a and c, by the following relations [103]:

$$a = -\lambda/(2\overline{Q}_x), \tag{4.6}$$

$$c = (3\lambda)/(2\overline{Q}_z). \tag{4.7}$$

The values $\overline{Q}_x$ and $\overline{Q}_z$ of each diffraction peak are obtained by fitting the intensity distribution with a pseudo-Voigt function [105]. Results reported in Figure 4.10 show that all BTO and SRO thin films are coherently strained to their underlying substrates, without any relaxation of the in-plane lattice parameter. The indication of this is that the peak positions share the same $\overline{Q}_x$ value. In addition, the absence of side peaks indicates the presence of mono-domain in the BTO thin film.

The measured values of in- and out-of-plane lattice parameters of each layer in all samples are shown in Table 4.3. The in-plane strain applied by a substrate to the BTO thin film is calculated as $\epsilon^a_{\mathrm{BTO}} = (a_{\mathrm{BTO}} - a_{\mathrm{b,BTO}})/a_{\mathrm{b,BTO}}$ (Section 4.1.3), by comparing the measured in-plane lattice parameter of the thin film a_{BTO} with the respective bulk value $a_{b,\mathrm{BTO}} = 3.992\,\text{Å}$ [5]. As a result, the in-plane compressive strain in our BTO thin films is the smallest on the SSO substrate (-0.38%, $a_{b,\mathrm{SSO}} = 3.977\,\text{Å}$ [106]), it increases on the GSO substrate (-0.63%, $a_{b,\mathrm{GSO}} = 3.967\,\text{Å}$ [106]) for both BTO/SRO/GSO and BTO/SRO*/GSO samples, and is the largest on the DSO substrate (-1.23%, $a_{b,\mathrm{DSO}} = 3.943\,\text{Å}$ [106]) (Table 4.3). Similar to the BTO thin film, the in-plane strain applied by a substrate to the SRO thin film is calculated as $\epsilon^a_{\mathrm{SRO}} = (a_{\mathrm{SRO}} - a_{\mathrm{b,SRO}})/a_{\mathrm{b,SRO}}$, by comparing the measured in-plane lattice parameter of the thin film a_{SRO} with the respective bulk value of the pseudocubic cell with parameter $a_{\mathrm{b,SRO}} \approx c_{\mathrm{b,SRO}} = 3.923\,\text{Å}$ [107]. As a result, the DSO, GSO, and SSO substrates impose an in-plane tensile strain on the SRO films of 0.51%, 1.12%, and 1.38%, respectively (Table 4.3).

Table 4.3.: In-plane lattice constants and in-plane strains of the samples under study. The in-plane lattice constants acquired from RSM and calculated compressive in-plane strain of each layer in all samples.

Sample	Layer	a (Å)	ϵ^a (%)
BTO/SRO/DSO	BTO	3.946	-1.23
	SRO	3.943	0.51
	DSO	3.943	
BTO/SRO/GSO	BTO	3.970	-0.63
	SRO	3.967	1.12
	GSO	3.967	
BTO/SRO/SSO	BTO	3.976	-0.38
	SRO	3.977	1.38
	SSO	3.977	
BTO/SRO*/GSO	BTO	3.967	-0.63
	SRO	3.967	1.12
	GSO	3.967	

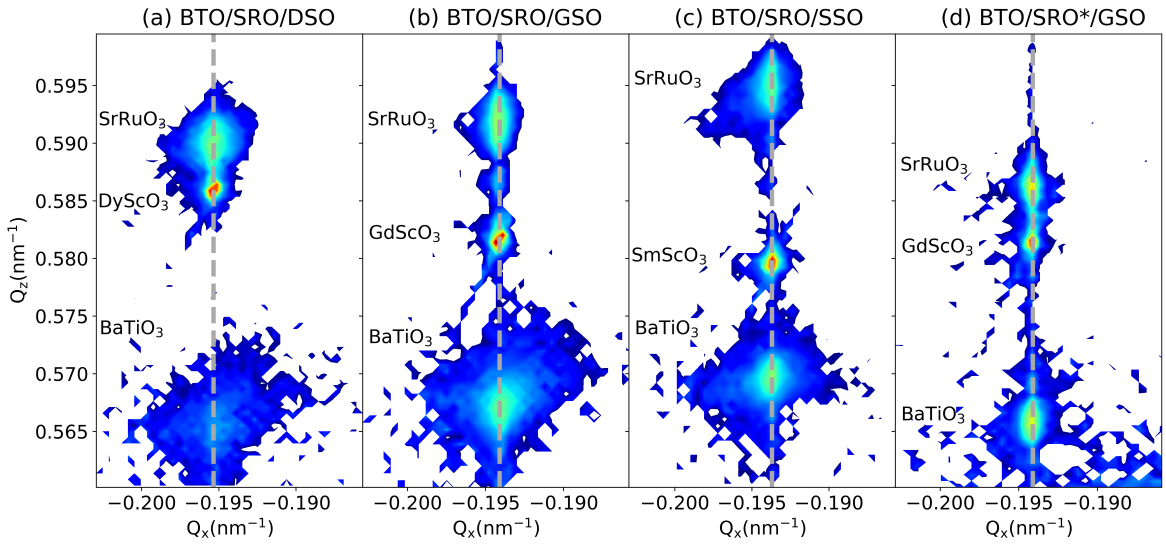

Figure 4.10.: Reciprocal space maps of the samples under study. Reciprocal space maps around the (-103) substrate Bragg peak for the BTO/SRO/DSO (a), BTO/SRO/GSO (b), BTO/SRO/SSO (c), and BTO/SRO*/GSO (d) samples. The gray vertical dashed lines denote the reciprocal lattice parameter $\overline{Q}_x$ common to the substrate, BTO, and SRO thin films in each sample.

4.6. Piezoresponse force microscopy

Piezoresponse force microscopy (PFM) is the technique that employs electromechanical contact between a tip mounted on one end of a cantilever and the sample [108, 109]. This technique is employed to characterize the orientation of the spontaneous polarization of BTO thin films. Because it is an electromechanical technique, both tip and cantilever need to be conductive. The cantilever is able to scan over the surface of the sample. In the normal setting of PFM, an AC voltage is applied to the cantilever through a lock-in amplifier and a DC voltage is applied to the sample. By doing this, an oscillating electrostatic force is induced between the tip and sample and it gives rise to an oscillation of the cantilever. The oscillation amplitude of cantilever is written as the following

$$\Delta z = d_{33} V_{AC} + 2\frac{Q_{333}}{t} V_{DC} V_{AC}, \tag{4.8}$$

where d_{33} is the piezoelectric coefficient, Q_{333} is the electrostrictive component of the sample, t is the thickness, V_{AC} is the applied AC voltage and V_{DC} is the applied DC voltage. To track this oscillation, a laser reflection from the cantilever is detected on a Photosensitive Detector (PSD). The detector converts the offset of the reflection spot from the detector center to a voltage signal. This signal acquired in the PSD is compared to the AC voltage input signal to extract the electromechanical signal including the phase and amplitude. Typically, if the spontaneous polarization of the sample is aligned with the applied DC field, driving voltage and electromechnical signal have zero phase difference. Conversely, if the spontaneous polarization and applied field are opposite, there is a phase difference of 180° (Figure 4.11).

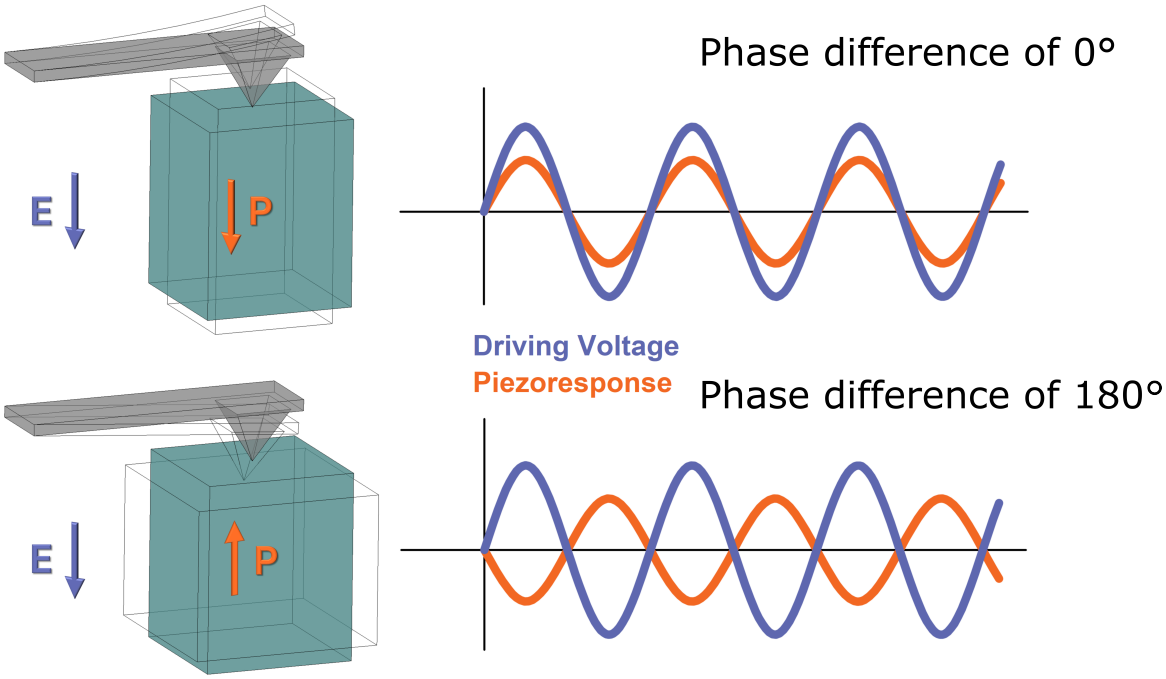

Figure 4.11.: Schematic illustration of piezoresponse force microscopy. The cantilever is oscillating on the same phase (phase difference of 0°) as its applied AC voltage when the spontaneous polarization of the sample is parallel to its applied DC voltage. Reversely, the phase difference between cantilever oscillation and applied AC voltage is 180° when the spontaneous polarization of the sample is opposite to the applied DC voltage.

PFM in Dual AC Resonance Tracking (DART) mode [110] was used to probe the polarization of as-grown samples and to prove that the ferroelectric polarization can be switched by the application of positive or negative voltage between the PFM tip and the SRO electrode. Figures 4.12a-c show the PFM phase image of each sample after the application of a voltage to switch the polarization inside the marked gray boxes. The polarization state of our samples is indicated by symbols $P^{\downarrow}$ and $P^{\uparrow}$. The symbol $P^{\downarrow}$ [$P^{\uparrow}$] indicates a polarization pointing toward [away from] the substrate, where the Ti atom is below [above] the oxygen octahedra. A positive [negative] voltage with the amplitude of 8 V forces the polarization to be $P^{\downarrow}$ [$P^{\uparrow}$], with the corresponding PFM phase 0° [180°]. The PFM phase outside the gray boxes indicates the polarization of the as-grown sample (Figure 4.12). Therefore, Figure 4.12a shows an average downward polarization $P^{\downarrow}$ in the BTO/SRO/DSO sample, while an average upward polarization $P^{\uparrow}$ in the BTO/SRO/GSO, BTO/SRO/SSO, and BTO/SRO*/GSO samples (Figures 4.12b-d). The average polarization direction of our samples is summarized in the Table 4.2. The different average polarization direction of the three BTO samples results from the complex interplay of the electronic structure and the chemistry of the surface and the interface to the bottom layer [9, 111, 112]. Finally, the fact that a homogeneous as-grown phase measured by PFM confirms the presence of a single domain in our samples ensures that atomic positions of the same structural phase are measured by XSW measurements.

We use switching spectroscopy PFM (SS-PFM) to measure hysteresis loops on the BTO/SRO/DSO, BTO/SRO/GSO, and BTO/SRO/SSO samples (Figure 4.13). In these measurements, the phase response loop of the sample is recorded while the tip voltage V_{AC} is changing and the sample is biased by a DC voltage V_b. Similar to the typical P-E loop of ferroelectrics, the threshold amplitude of the tip voltage, when the phase of the sample is reversed, is the coercive voltage V_c. The bias voltage V_b indicates the shift of the center of the hysteresis loop along the tip voltage axis. The results show that we measure a coercive voltage of $V_c = 1.1\,\mathrm{V}$, with a negative DC bias $V_b = -0.9\,\mathrm{V}$, in the BTO/SRO/DSO sample. In contrast, the coercive voltage of BTO/SRO/GSO sample is $V_c = 1.6\,\mathrm{V}$, with a positive DC bias $V_b = 0.7\,\mathrm{V}$. Finally, the unbiased hysteresis loop of the BTO/SRO/SSO sample ($V_b = 0\,\mathrm{V}$) has a coercive voltage $V_c = 1.1\,\mathrm{V}$.

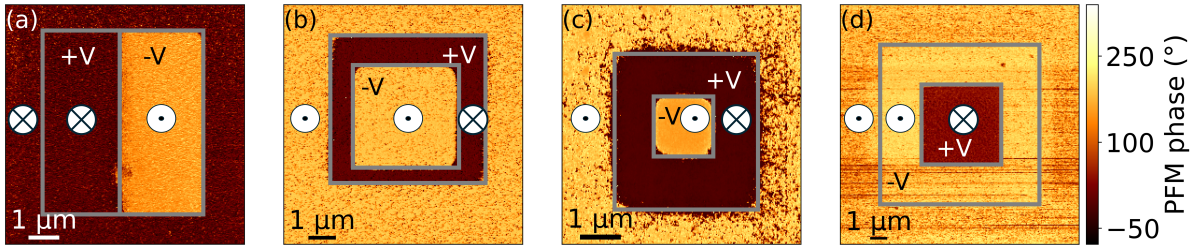

Figure 4.12.: PFM phase images of BTO thin films. PFM phase images of the BTO/SRO/DSO (a), BTO/SRO/GSO (b), BTO/SRO/SSO (c), and BTO/SRO*/GSO (d) samples. Each panel shows the sign of the applied tip voltage (±V) within the gray boxes and the resulting average polarization direction $P^{\uparrow}$ ($\odot$) or $P^{\downarrow}$ ($\otimes$) in the examined areas. The voltage applied was 8 V. The PFM phase outside the gray boxes reveals the average polarization direction of the as-grown samples.

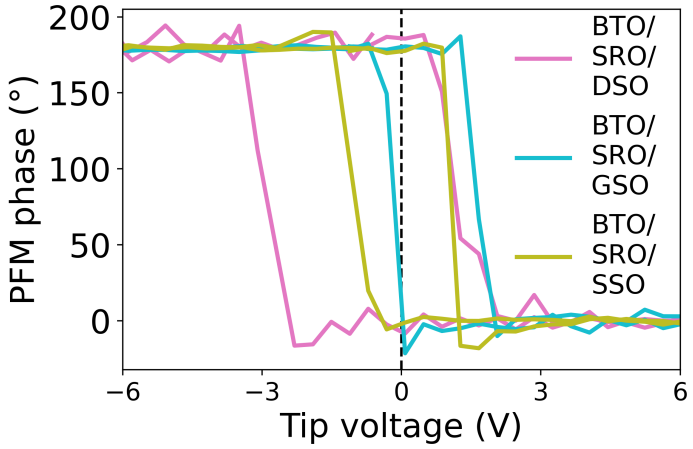

Figure 4.13.: Hysteresis loops of BTO thin films. The hysteresis loops measured by SS-PFM on the BTO/SRO/DSO, BTO/SRO/GSO, and BTO/SRO/SSO samples.

5. Surface polarization profile of ferroelectric thin films

Ferroelectric materials with mono-domain or uniform polarization tend to accumulate surface charges that create a depolarization field opposing the spontaneous polarization. This accumulation of uncompensated charges can destabilize the ferroelectric phase. Several mechanisms can mitigate the accumulation of surface charges. For instance, external charges provided by adsorbates can help compensate for these surface charges [11–15]. Additionally, surface charges can be neutralized through the reconstruction of the top unit cells [16–18]. Understanding these mechanisms is crucial for controlling surface polarization in ferroelectric thin films. In this chapter, we demonstrate that the XSW method can be used to directly investigate the surface polarization profile of ferroelectric thin films. Using XSW, we achieve picometer precision in determining the atomic positions of Ti and Ba near the surface of our BTO thin films along the out-of-plane direction. This technique offers direct insight into the local ferroelectric polarization at and below the surface by providing precise atomic positioning. Additionally, XPS enables us to acquire detailed information about the oxygen-containing species adsorbed on the surface after exposure to ambient conditions. By integrating structural and spectroscopic data, we identify the most likely mechanisms that stabilize the surface polarization in the three samples under examination. The surface charges, which depend on the type, quantity, and spatial distribution of the oxygen-containing adsorbates, are linked to variations in the amplitude and direction of the local ferroelectric polarizations.

5.1. Results

5.1.1. (001) Bragg reflections

As described by the theory of X-ray standing waves generated in thin films (Section 2.1), we need a model of X-ray diffracted intensity $R(E_\nu, z)$ to construct the mathematical formula for the PE yield fit function $\kappa_\gamma^s(E_\nu)$. This model is based on the fit of experimental X-ray diffraction curves to obtain the lattice parameter profile. The reflectivity curves around the (001) diffractions of the BTO, SRO, and substrates are shown in Figure 5.1. The diffraction intensities of the substrate are stronger than those of the thin layers by two orders of magnitude. In addition, the widths of substrate Bragg peaks are much narrower than those of thin layers peaks. The weak intensity and the broad width of the thin film diffraction peaks stem from two factors: the finite film thickness and the inhomogeneous strain. Particularly, the reflectivity in the range of $0.03\% - 0.05\%$ [$0.01\% - 0.02\%$] belongs to BTO [SRO] thin films, while reflectivity of up to 10% is meaured for the substrate. Owing to the decreasing trend of the bulk out-of-plane lattice parameters of the substrates (Figure 5.1), there is a gradual shift of the substrate diffraction peak to higher photon energies going from SSO, to GSO, and then to DSO. This trend implies that BTO films experience an in-plane compressive strain, while SRO films experience an in-plane tensile strain in the same substrate order. Consequently, the average c parameters of BTO (Section A.4) increase as $\bar{c}_{\mathrm{BTO}} = 4.055(22)$ Å, $4.063(23)$ Å, $4.070(45)$ Å from the SSO to the DSO sample. For the BTO thin films, an average out-of-plane strain $\bar{\epsilon}^c_{\mathrm{BTO}} = (\bar{c}_{\mathrm{BTO}} - c_{b,\mathrm{BTO}})\,/\,c_{b,\mathrm{BTO}}$ of 0.48%, 0.68% and 0.84% is calculated, corresponding to the measured $\bar{c}_{\mathrm{BTO}}$ parameters for SSO, GSO, and DSO, respectively, and given the bulk out-of-plane lattice parameter $c_{b,\mathrm{BTO}} = 4.036$ Å [5]. In terms of SRO films, the average c parameters decrease as $\bar{c}_{\mathrm{SRO}} = 3.885(19)$ Å, $3.876(24)$ Å, $3.866(23)$ Å from the DSO to the SSO sample. These measured $\bar{c}$ parameters correspond to an average out-of-plane compressive strain $\bar{\epsilon}^c_{\mathrm{SRO}} = (\bar{c}_{\mathrm{SRO}} - c_{b,\mathrm{SRO}})\,/\,c_{b,\mathrm{SRO}}$ of -0.96%, -1.20%, and -1.45%, respectively.

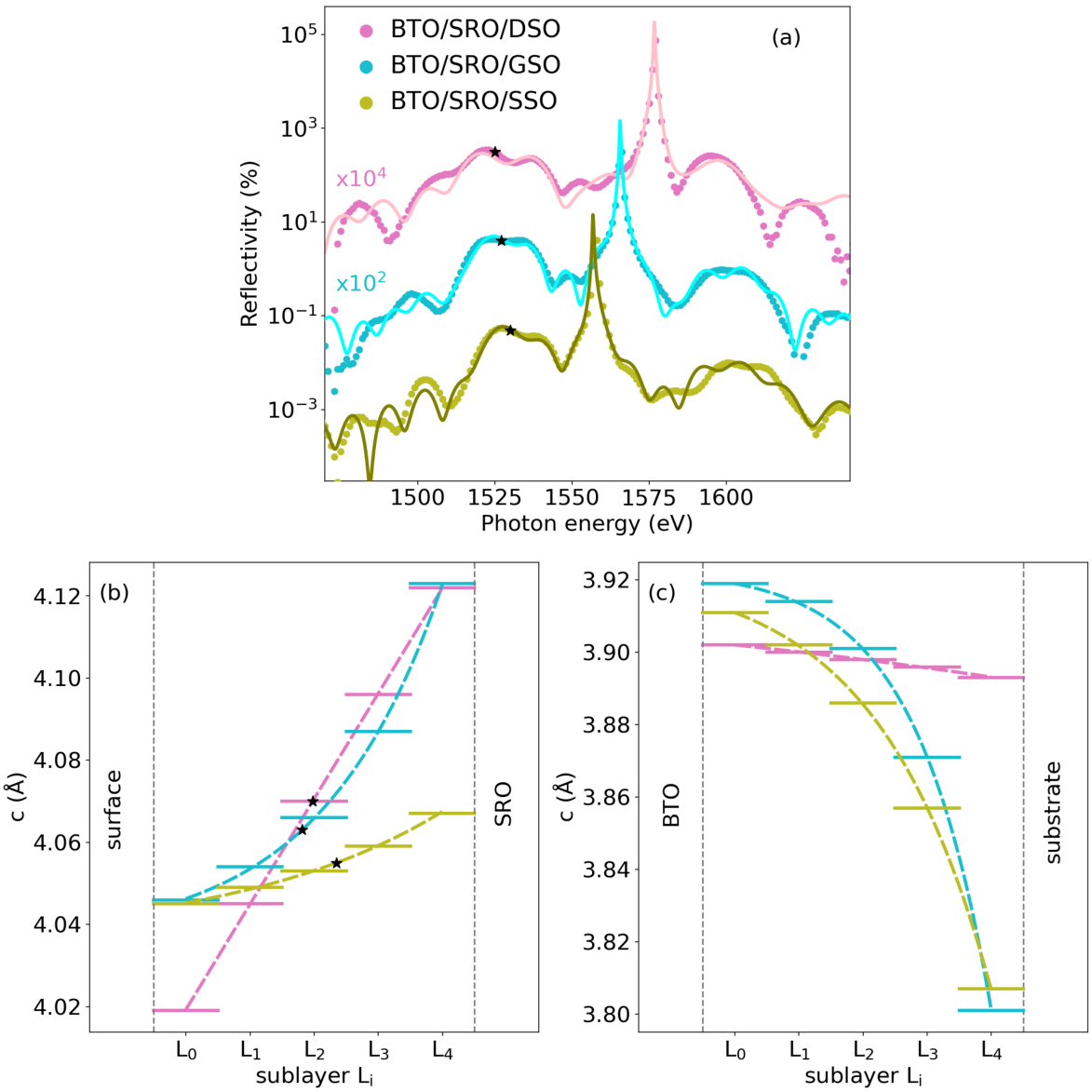

Figure 5.1.: (001) Bragg reflections: fit and out-of-plane lattice parameters. (a) (001) Bragg reflectivity $R_0(E_\nu)$ (dots) and corresponding fit curves (solid lines) of samples BTO/SRO/DSO (pink), BTO/SRO/GSO (cyan) and BTO/SRO/SSO (green). (b) BTO out-of-plane lattice parameter c_i (solid lines) in sublayers L_i and $c(z)$ (dotted lines) based on Equation (5.1). The average BTO out-of-plane lattice parameters $\bar{c}_{\mathrm{BTO}}$ are denoted by black stars. (c) SRO out-of-plane lattice parameters c_i (solid lines) in sublayers L_i and $c(z)$ (dotted lines) according to Equation (5.1).

As aforementioned, an epitaxial thin film can exhibit an inhomogeneous out-of-plane strain. Based on the general strain profile model outlined in previous studies [8, 13], the strain gradient is anticipated to be proportional to the strain, $\partial\epsilon^c/\partial z \propto \epsilon^c$, regardless of the specific relaxation mechanism. Accordingly, the distribution of the out-of-plane parameter c can be expressed as an exponential dependence on z:

$$c(z) = c_b \left(1 + \epsilon^c_{\text{int}} \mathrm{e}^{-(t-z)/\delta}\right), \tag{5.1}$$

where $\epsilon^c_{\text{int}} = (c_{\text{int}} - c_b)/c_b$ is the strain at the interface with the underlying layer (or substrate), and δ is the penetration depth of strain that is inversely proportional to the strain gradient. The validity of this model has been demonstrated in ferroelectric thin films of several hundreds nm [8, 113]. A recent study on 50 nm thick $PbTiO_3$ films, with high crystalline quality and no evidence of in-plane relaxation, reveals an exponential profile of c parameters which is later confirmed by TEM images [114, 115]. In this case [115], a compositional gradient of lead oxide dipolar vacancies leads to the strain gradient. The presence of strain gradients in our samples may also origin from a similar distribution of vacancies. In fact, the assumption of constant $\bar{c}$ in modelling BTO and SRO thin films fails to achieve satisfactory fit results. To fit the experimental reflectivity curves in Figure 5.1, BTO and SRO layers are divided in n sublayers L_i (with $i = 0, ..., n-1$) of equal thickness t_i with an out-of-plane lattice parameter c_i changing exponentially with i as depicted by Equation (5.1). In addition, different sublayers L_i have different Debye-Waller factors e^{-W_i} and deformation phases $\varphi_i = 2\pi(c_i - \bar{c})t_i/\bar{c}^2$. In our samples, $n = 5$ is the minimum common number of sublayers necessary to precisely describe them. Larger number of sublayers n does not improve the fit.

Furthermore, both the exponential c distribution of Equation (5.1) and the linear c distribution $c(z) = c_b\left(1 + \epsilon^c_{\text{int}}\delta_{lin}(t-z)\right)$ were utilized and compared in Section A.5 for the BTO thin film of the BTO/SRO/DSO sample. In the linear c distribution, the rate of strain change along z is denoted as δ_{lin}. It is observed that, for the 20 nm BTO layer in BTO/SRO/DSO, a linear c distribution can represent the experimental data more accurately than an exponential one. According to TEM research, a similar finding was documented for films with thickness $\leq$ 20 nm [116, 117]. It is also worth noting that applying the linear distribution to the bottom SRO layers or the thicker BTO layers did not result in a better fit. Experimental data in Figure 5.1a are fitted with the reflectivity

$R_0(E_v)$ using the fitting parameters e^{-W_i} ($i = 0, ..., 4$), ϵ^c_{int} and δ (or δ_{lin}) for the BTO and SRO layer (Table 5.1 and 5.2).

The reasonably good fit of the experimental data shown in Figure 5.1a validates the proposed assumption of strain gradient employed to model these samples, with deviations $< 5 \times 10^{-3}$%. Relatively simple strain models with only two fit structural factors (ϵ^c_{int} and δ or δ_{lin}), however, are unable to replicate some details of the strain distribution, as suggested by the slight differences between fit curves and experimental data. The obtained out-of-plane parameters c_i of BTO and SRO films in different sublayers L_i are indicated in Figures 5.1b-c. For BTO, c_i increases as a function of depth, corresponding to the increasing in-plane compressive strain. Meanwhile, for SRO, c_i decreases as we go further away from the interface between BTO and SRO, in agreement with the increasing in-plane tensile strain.

Table 5.1.: Debye-Waller factors. BTO and SRO Debye-Waller factors e^{-W_i} of sublayers L_i ($i = 0, ..., 4$) resulting from the fits of (001) Bragg reflection data in the three samples under study (Figure 5.1).

Layer	Sublayer	Fit parameters	BTO/SRO/DSO	BTO/SRO/GSO	BTO/SRO/SSO
BTO	L_0	e^{-W_0}	1	0.9	1
	L_1	e^{-W_1}	1	1	1
	L_2	e^{-W_2}	1	1	0.9
	L_3	e^{-W_3}	1	1	1
	L_4	e^{-W_4}	1	0.1	0.5
SRO	L_0	e^{-W_0}	0.5	0.7	0.9
	L_1	e^{-W_1}	1	0.7	1
	L_2	e^{-W_2}	1	0.9	0.6
	L_3	e^{-W_3}	0.01	1	0.5
	L_4	e^{-W_4}	0	0	0.7

The Debye-Waller factors e^{-W_i} of larger than 0.9 are obtained in almost all BTO sublayers except the sublayer at the interface to SRO. The Debye-Waller factors of SRO at the interface to BTO and GSO are small (less than 0.9) in

Table 5.2.: Interface strains and penetration depths of strain. BTO and SRO interface strain ϵ_{int} and penetration depth of strain δ resulting from the fits of (001) Bragg reflection data in the three samples under study (Figure 5.1).

Layer	fit parameters	BTO/SRO/DSO	BTO/SRO/GSO	BTO/SRO/SSO
BTO	ϵ_{int}	0.02	0.03	0.01
	δ	1.5×10^{-4}	139	237
SRO	ϵ_{int}	-0.01	-0.05	-0.04
	δ	124	57	78

general. The significant structural disorder of BTO at the interface to the layer underneath has been evidenced by other transmission electron microscopy (TEM) studies [116–118].

The fit parameters ϵ^c_{int} and δ of BTO, in the BTO/SRO/GSO and BTO/SRO/SSO samples, are directly and inversely proportional to the in-plane compressive strain ϵ^a_{BTO}, respectively (Table 5.2). The strain at the interface with the substrate ϵ^c_{int} of SRO, for the BTO/SRO/DSO sample with the least tensile strain (Table 4.3), is the smallest. In addition, a larger tensile strain leads to smaller obtained out-of-plane strain penetration depth δ for SRO.

In fact, for BTO, a larger in-plane compressive strain ϵ^a_{BTO} is associated with larger average out-of-plane strain $\overline{\epsilon}^c_{\text{BTO}}$ and thus, a larger strain gradient. TEM and CTR scattering measurements on BTO thin films [13, 116] and other ferroelectrics [115, 117, 118] provide comparable and even larger strain gradients, compared with $\partial\epsilon^c/\partial z = 1.5\times10^{-4}\,\text{nm}^{-1}$ in BTO/SRO/DSO. Surprisingly, the strain gradients cause similar out-of-plane lattice parameters c_0 at the top sublayer L_0: 4.02 Å, 4.046 Å, 4.045 Å, in spite of the different in-plane compressive strains in the three samples (Table 4.3). For SRO, a larger in-plane tensile strain ϵ^a_{SRO} (Table 4.3) leads to a larger out-of-plane strain gradient and to larger average out-of-plane compressive strain $\overline{\epsilon}^c_{\text{SRO}}$ (Figure 5.1c). For example, the BTO/SRO/GSO [BTO/SRO/DSO] sample with an in-plane tensile strain of SRO of 1.38 % [0.51 %] (Table 4.3) exhibits an out-of-plane strain gradient of $\partial\epsilon^c/\partial z = 1\times10^{-3}\,\text{nm}^{-1}$ [$1\times10^{-4}\,\text{nm}^{-1}$] and an average out-of-plane strain $\overline{\epsilon}^c_{\text{SRO}} = -1.45\%$ [-0.96%] (Figure 5.1c).

At this point, the fit of the experimental diffraction curves in Figure 5.1

provides the depth dependent distribution of c in both BTO and SRO. These c distributions help to construct the PE yield fit function $\kappa_\gamma^s(E_\nu)$ in Equation (2.3). We now move to determine the experimental PE yield from XPS spectra.

5.1.2. Ba, Ti, O and C XPS

The PE yield $\kappa_\gamma^s(E_\nu)$ of atomic species s, measured at exit angle range γ and photon energy E_ν, is calculated as the background-subtracted integral of the corresponding PE peak. Ba 4d and Ti 2p PE spectra were measured over the three exit angle ranges (γ_1, γ_2, and γ_3) in order to determine the PE yield of Ba and Ti atoms in the BTO thin films. The results are shown in Figure 5.2. The 2p doublet is visible in the Ti spectra in Figure 5.2a at 458.8 and 464.5 eV. The same spectral shape can be seen in spectra taken at various exit angles (Figure 5.2a). This suggests that the formation of the nominal Ti^{4+} state occurs both at Ti atoms below the surface, and also at surface Ti atoms attached to oxygen-containing adsorbates [12, 119, 120]. Furthermore, the lack of a peak at 1.7 eV beneath the primary Ti $2p_{3/2}$ peak indicates that there are no oxygen vacancies that would cause Ti^{3+} to form close to the BTO surface [12, 119].

On the other hand, Ba 4d spectra reveal at least two different types of atomic species (Figure 5.2b). The bulk component (Ba_{bulk}) is the result of the spin-orbit split levels Ba $4d_{5/2}$ and Ba $4d_{3/2}$ at 88.8 eV and at 91.4 eV, respectively, originating from the Ba atoms below the surface. With respect to the bulk component, the Ba_{surf} peaks show twice the FWHM and a binding energy shift $\Delta BE = +1.2\,eV$. According to earlier research [121, 122], the increase of Ba_{surf} in the most surface sensitive spectrum ($Ba(\gamma_1)$) demonstrates its relationship to Ba atoms at the BTO surface. The correlation with oxygen components suggests that the larger FWHM is consistent with a continuity of chemical environments surrounding Ba atoms at the surface [122]. These environments could be related to different species, like OH^-, at different adsorption sites [9, 10], and $O_2{}^-$ species [121]. Therefore, to include both Ba atoms at the surface and just below it, the PE yield with the largest contribution from the surface unit cell (γ_1) is given by the sum of the two components ($Ba_{surf} + Ba_{bulk}$). Meanwhile, the Ba PE yield of the deeper unit cells (at γ_2 and γ_3) is only provided by the Ba_{bulk} component. Conversely, for all exit angle ranges, the Ti PE yield is determined by the entire area of the Ti doublet. As demonstrated above, the XSW approach allows for the selective determination of the positions of distinct chemical species within the same element due to the ability of XPS to

distinguish between atoms in different chemical environments.

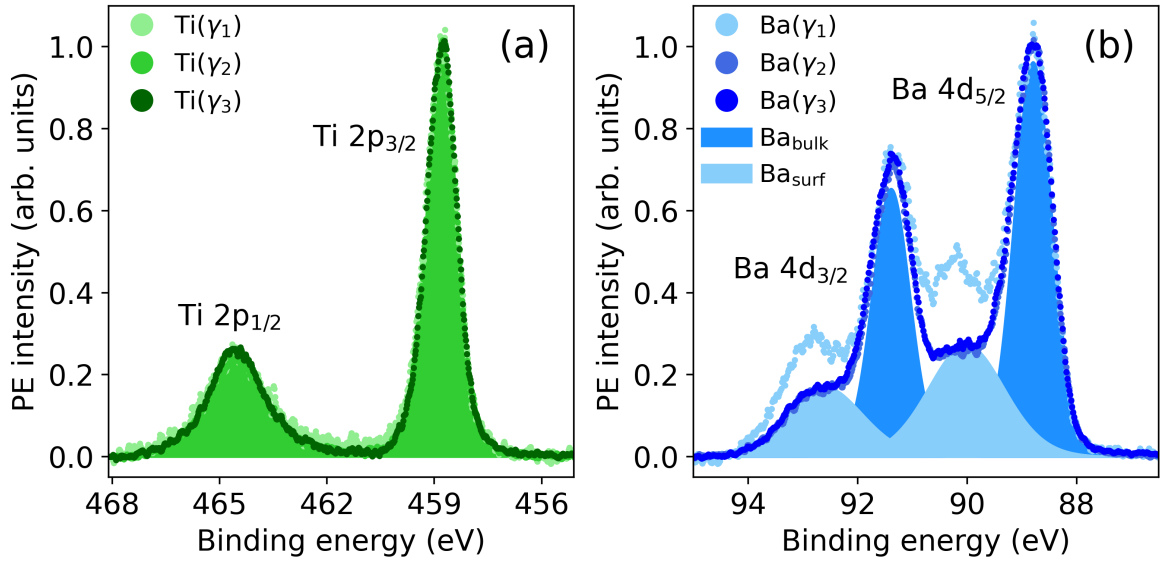

Figure 5.2.: PE spectra of the Ti 2p and Ba 4d core levels of the BTO/SRO/DSO sample. PE spectra of the Ti 2p (a) and Ba 4d (b) core levels on the BTO/SRO/DSO sample, measured at the exit angle ranges γ_1, γ_2, and γ_3 using $E_\nu = 1420\,\text{eV}$. Every spectrum is normalized to the corresponding maximal PE intensity. The spectra measured at the exit angle range γ_3 are indicated by the shaded component areas. The Ba atoms at [below] the top BaO atomic plane are denoted by the Ba_{surf} [Ba_{bulk}] component. Figure 5.3 gives similar PE spectra measured on the BTO/SRO/GSO and BTO/SRO/SSO samples.

Typical PE spectra Ti 2p, Ba 4d, and C 1s core levels of the BTO/SRO/GSO and BTO/SRO/SSO samples are displayed in Figure 5.3. The features of the Ti and Ba PE spectra are comparable to those in Figure 5.2. Because there are more C and O species on the BTO/SRO/SSO surface, the PE intensity is lower, which results in higher noise of the PE spectra in Figures 5.3d-e. As shown in Figure 5.3c, the corresponding C 1s spectrum is almost three times larger than the one from the BTO/SRO/GSO sample. Particularly, Figure 5.3f displays a typical C 1s spectrum that consists of four components. The adventitious carbon component $C(1)$ at 284.6 eV is attributed to hydrocarbons that adsorbed on the sample surface after being exposed to the ambient environment. With BE shifts of 1.5 eV and 3 eV, components $C(2)$ and $C(3)$ denote C atoms connected to an O atom by a single (C-O) or double (C=O) bond [121, 123]. With a BE shift of 4.4 eV, component $C(4)$ can be associated with C atoms in ester or carboxyl groups [C-(C=O)-O] or carbonate compounds [121, 123].

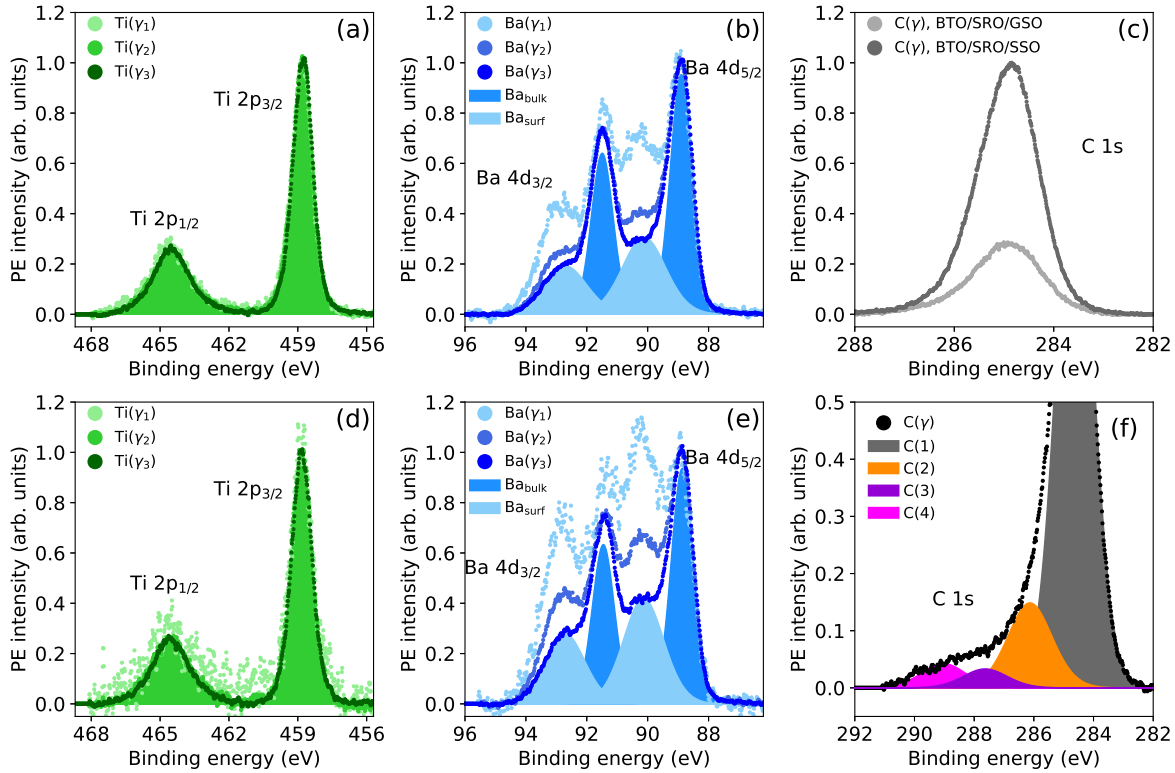

Figure 5.3.: Ti 2p, Ba 4d, and C 1s PE spectra of the BTO/SRO/GSO and BTO/SRO/SSO samples. The Ti 2p, Ba 4d, and C 1s PE spectra of the BTO/SRO/GSO sample (a, b, c) and the BTO/SRO/SSO sample (d, e, f), respectively. The Ti 2p and Ba 4d spectra are displayed at the γ_1, γ_2, and γ_3 exit angle ranges. The total of the C 1s spectra for the BTO/SRO/GSO and BTO/SRO/SSO samples over all measured exit angle ranges is displayed in Panel (c). It should be noted that to highlight the differences in the carbon species composition of the two samples, both C 1s spectra are normalized to the peak intensity of the C 1s spectrum of the BTO/SRO/SSO sample. A typical C 1s spectrum fitted with four components is displayed in Panel (f).

A comprehensive picture of oxygen-related species at the BTO surface is provided by O 1s PE spectra recorded at various exit angle ranges γ (Figures 5.4a-c). First, let us consider the most bulk sensitive $O(\gamma_3)$ spectra. In this instance, the most noticeable peak at 529.8 eV, $O(1)$, corresponds to O atoms within the BTO lattice (O_L). The remaining O components originate from CO_x species ($O(3)$) and H_2O dissociation ($O(2)$ and $O(4)$). In general, the molecular physisorption with $\Delta BE \approx 3.9$ eV may result from the adsorption of H_2O on BTO [120, 121]. The O 1s spectra presented in Figures 5.4a-c demonstrate the presence of physorbed water molecules exclusively in the more surface sensitive γ_1 and γ_2 exit angle ranges, and their contributions to the total spectral area are negligible (less than 3%). While both molecular and dissociated water may occur on the TiO_2 termination [10, 120], water on the BaO termination upon adsorption dissociates into OH^- and H^+ [10, 11, 124]. H^+ binds to O_L at the BTO surface or diffuses within the film to create O_LH^- [12–14, 119], whereas OH^- chemisorbs on top of cations (Ba or Ti) or at O vacancies $O(2)$ [10–13]. H^+ is assigned to component $O(2)$ with the binding energy shift $\Delta BE = 1$ eV, while OH^- is assigned to component $O(4)$ with larger binding energy shift $\Delta BE = 2.7$ eV. Furthermore, component $O(4)$ may be enhanced by other species that arise from O_2 adsorption, such as peroxo complexes (e.g., BaO_2, Ti-O-O-Ti, Ti=O_2^-) [120]. In this case, O_2^- is present at the surface as a result of oxidation of Ti-OH or BaO-terminated surfaces. Lastly, CO_x species, such as carbonates CO_3^{2-}, C = O bonds, ester (C-(C=O)-OR) or carboxylic acid (C-(C=O)-OH) compounds are assigned to component $O(3)$ at $\Delta BE = 1.8$ eV.

The contribution of component $O(3)$ to the γ-integrated spectral area is $\approx 0\%$, 3%, and 6% in the BTO/SRO/DSO, BTO/SRO/GSO, and BTO/SRO/SSO samples, respectively. Component $O(2)$ [$O(4)$] represents 15% [32%], 19% [30%], and 13% [53%] of the γ-integrated spectral area, assuming the same substrate order. A correlation between the PE area of the Ba_{surf} component and the total of the PE areas of the O(2) and O(4) components is depicted in Figure 5.5. The fact that the sample BTO/SRO/DSO has a Ba_{surf} component (Figure 5.2b), despite the O(3) component not being present in the corresponding O 1s PE spectrum (Figure 5.4a), indicates that component O(3) has a weaker correlation with Ba_{surf}.

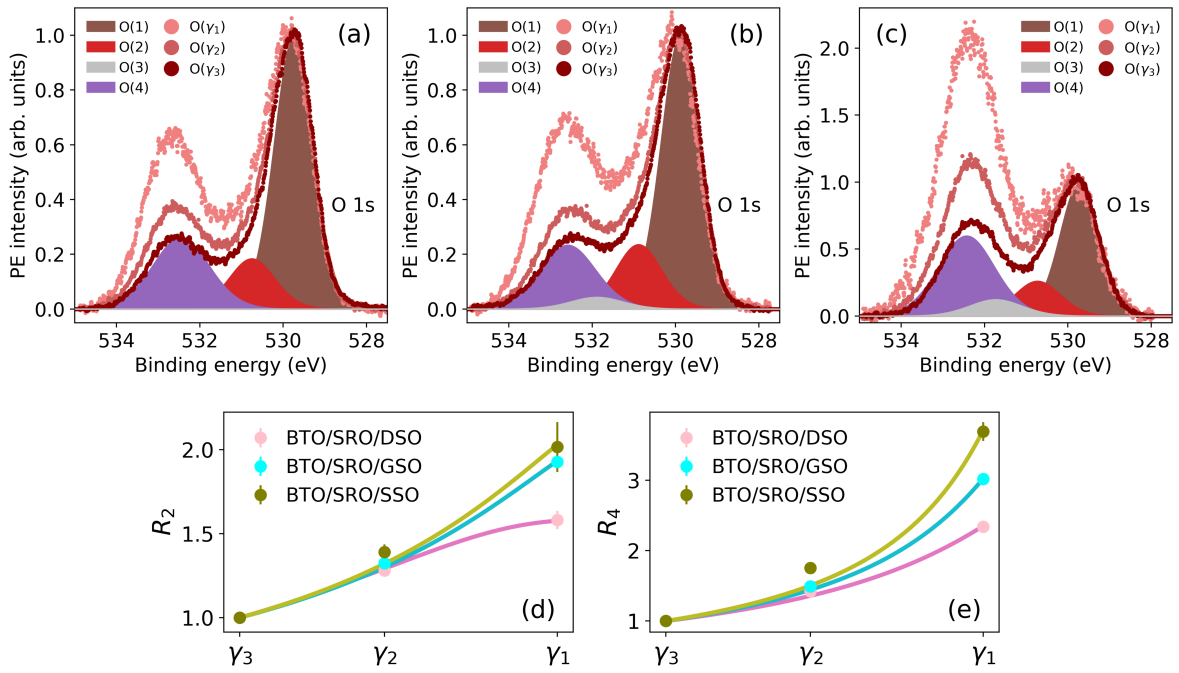

Figure 5.4.: O 1s PE spectra of the BTO/SRO/DSO, BTO/SRO/GSO, and BTO/SRO/SSO samples. The O 1s PE spectra of the BTO/SRO/DSO (a), BTO/SRO/GSO (b), and BTO/SRO/SSO (c) samples are O(γ_1), O(γ_2) and O(γ_3) integrated over the corresponding exit angle ranges. Every spectrum is normalized to the corresponding maximum intensity of PE. O(γ_3) spectra are indicated by the shaded component areas O(1), O(2), O(3), and O(4). O atoms in the lattice (O_L), O_LH^- species, CO_x species, and OH^- and/or O_2^- species are represented by components O(1), O(2), O(3), and O(4), respectively. Panel (d) [(e)] shows the ratio of component O(2)[O(4)] over component O(1) for the three samples as a function of exit angle range γ.

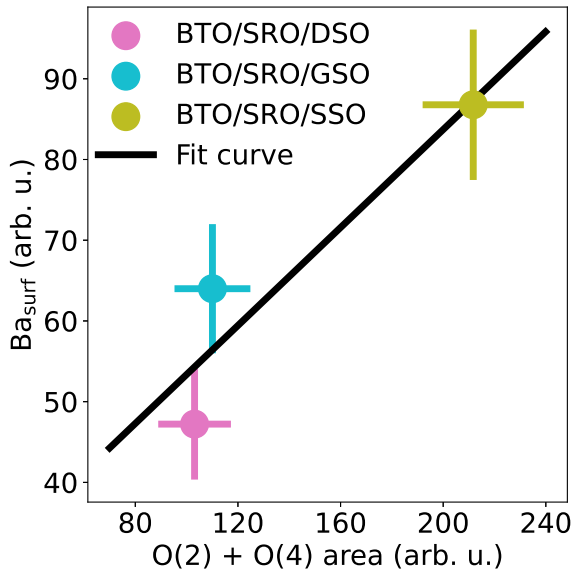

Figure 5.5.: Relation between the areas of Ba_{surf} and O(2)+O(4) components. PE area of Ba_{surf} component, with a linear fit curve, as a function of the sum of PE areas of O(2) and O(4) components.

A quantitative analysis of O(2) and O(4) relative spectral area as a function of exit angle range γ was carried out to obtain information on the depth distribution of the various oxygen species. The spectral area ratio of O(2) [O(4)] over O(1) is computed as $R_2 = A^{\gamma_j}_{\mathrm{O(2)}}/A^{\gamma_j}_{\mathrm{O(1)}}$ [$R_4 = A^{\gamma_j}_{\mathrm{O(4)}}/A^{\gamma_j}_{\mathrm{O(1)}}$], measured at the exit angle range γ_j ($j = 1, 2, 3$). R_2 and R_4 at various γ_j are displayed in Figures 5.4d-e with the corresponding fits. According to the model used to fit these data [125], adsorbates create a patched overlayer of thickness $t_{\mathrm{O(k)}}$ ($k = 2, 4$) and coverage Γ ($0 < \Gamma < 1$), which shows the fraction of surface covered by the overlayer. The fitting parameter Γ is applied to the R_2 and R_4 data in Figures 5.4d-e. The $t_{\mathrm{O(k)}}$ is changed in 1 Å steps to produce the best fit with $R^2 \approx 1$. A superficial layer with a thickness of ≈ 4 Å, corresponding to one monolayer [120], is formed by the adsorbates represented by component O(4) on all samples. On the other hand, component O(2) is concentrated near the surface with thickness ≈ 6 Å in the BTO/SRO/SSO and BTO/SRO/GSO samples, while it is distributed below the BTO surface with thickness ≈ 15 Å in the BTO/SRO/DSO sample. A thicker overlayer of O_LH^- species above the BTO surface cannot account for the increased thickness $t_{\mathrm{O(2)}}$ in the BTO/SRO/DSO sample since the molecules in the overlayer would appear at a different binding energy due to their different chemical environment. Alternatively, as previously suggested in other publications [13, 14], our experimental findings imply a situation where H^+ atoms are spread below the BTO surface to create O_LH^- species (Figure 5.7b).

5.1.3. Ba and Ti XSW

The normalized PE yields of Ti and Ba, denoted as $\kappa^{\mathrm{Ti}}_{\gamma}(E_\nu)$ and $\kappa^{\mathrm{Ba}}_{\gamma}(E_\nu)$, are displayed in Figure 5.6. These yields were measured over the exit angle ranges γ_1, γ_2, and γ_3, around the BTO (001) Bragg peak of the three samples under study. The average and standard deviation of N photoelectron yield profiles ($5 < N < 10$) taken under identical conditions provide each $\kappa^{s}_{\gamma}(E_\nu)$ and associated error bar σ_κ. The intensity of the incident X-ray beam and the corresponding photoionization cross section over the recorded photon energy range are used to normalize each PE yield curve in Figure 5.6 (Section A.6). The $\kappa^{\mathrm{Ti}}_{\gamma}(E_\nu)$ curves have a peak corresponding to the BTO reflectivity maximum, whereas $\kappa^{\mathrm{Ba}}_{\gamma}(E_\nu)$ profiles have a dip-like shape. This can be interpreted as the following. The Ba atomic planes [45, 126] (dashed lines in Figure 3.1b) are

close to the Bragg diffraction planes for the BTO (001) reflection. A sinusoidal modulation of the X-ray intensity I_{XSW} and period d_{001} along $\boldsymbol{H}$ results in the formation of the XSW when the incoming X-ray photon energy meets the Bragg condition ($E_\nu \approx E_B$) from the low-energy side. As shown in Figures 3.1a-b, the standing wave antinodes and nodes are located between and at the diffraction planes, respectively. As a result, Ba atoms, which are aligned with the nodes and near the diffraction planes, experience a decrease in I_{XSW} and thus have lower $\kappa_\gamma^{\mathrm{Ba}}(E_\nu)$, whereas Ti atoms, which are more aligned with the antinodes and almost halfway between two adjacent diffraction planes, exhibit an increase in $\kappa_\gamma^{\mathrm{Ti}}(E_\nu)$. The nodes and antinodes shift by $d_{001}/2$ along $\boldsymbol{H}$ as the photon energy is modulated through the Bragg condition ($E_\nu > E_B$), and the XSW intensity modulation disappears. The reflectivity maxima of our samples vary from 0.02% to 0.05% due to the thin film's weak diffraction of the incident X-ray wave. As a result, a low XSW intensity modulation with an amplitude of less than 4% is produced by the interference between the incoming and Bragg-diffracted X-ray waves. This modulation is proportional to $2\sqrt{R_0(E_\nu)}$. However, as illustrated below, this contrast is sufficient to determine the average atomic distribution within the unit cell with picometer spatial accuracy using the data encoded in the PE yield profiles.

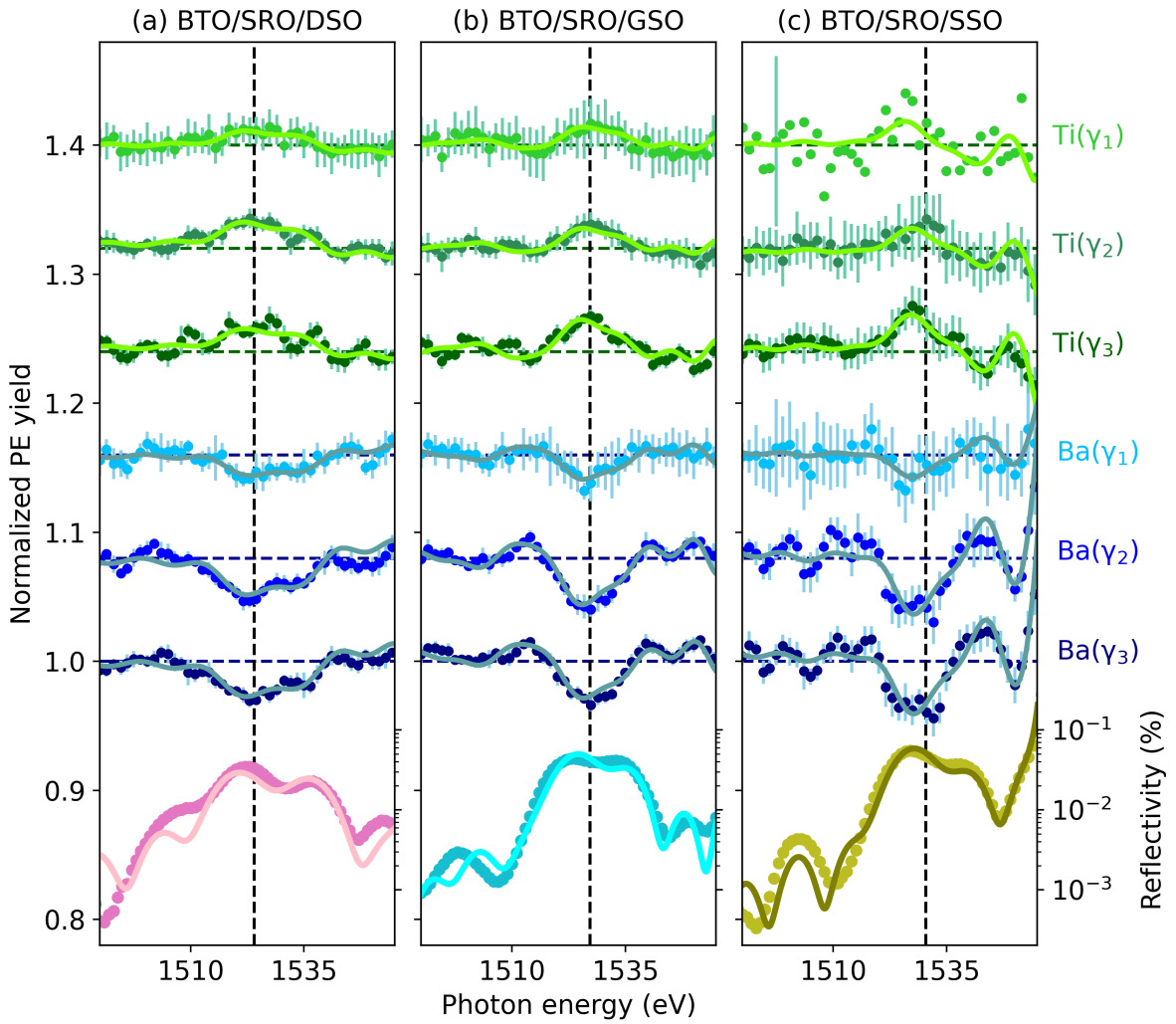

Figure 5.6.: Ti and Ba PE yield data and fits. Ti and Ba PE yield (green and blue points), and their corresponding fit curves (solid lines), obtained at the exit angle ranges γ_1, γ_2, and γ_3 on BTO/SRO/DSO (a), BTO/SRO/GSO (b), and BTO/SRO/SSO (c). At the bottom of each panel: reflectivities $R_0(E\nu)$ and their fit curves around the (001) BTO Bragg energies $E_B = 1524\,\text{eV}$ (a), 1527.2 eV (b), 1530.4 eV (c) (indicated by vertical dashed lines). There is only one error bar displayed for $\kappa^{\text{Ti}}_{\gamma_1}(E_\nu)$ of BTO/SRO/SSO. This error bar represents the average error bar of all the $\kappa^{\text{Ti}}_{\gamma_1}(E_\nu)$ data points. The curves above Ba(γ_3) are vertically displaced from the one below by 0.08. All PE yield curves are normalized (Section A.6).

Table 5.3.: Fit results of coherent position $P^s_{c,\gamma}$ and coherent fraction $F^s_{c,\gamma}$. Coherent position $P^s_{c,\gamma}$ and coherent fraction $F^s_{c,\gamma}$ of Ba and Ti PE yield fits (Figure 5.6) at the exit angle ranges γ_1, γ_2, and γ_3, in the three samples under study. Coherent position offset of Ti atoms from the center of the unit cell defined by Ba atoms, $\Delta P^{\mathrm{Ti}}_{c,\gamma} = P^{\mathrm{Ti}}_{c,\gamma} - \left(P^{\mathrm{Ba}}_{c,\gamma} - 0.5\right)$, and absolute off-center displacement of Ti atoms, $\Delta z^{\mathrm{Ti}}_{\gamma} = c_0 \Delta P^{\mathrm{Ti}}_{c,\gamma}$, expressed in picometer.

Sample	Angle range	$P^{\mathrm{Ba}}_{c,\gamma}$	$F^{\mathrm{Ba}}_{c,\gamma}$	$P^{\mathrm{Ti}}_{c,\gamma}$	$F^{\mathrm{Ti}}_{c,\gamma}$	$\Delta P^{\mathrm{Ti}}_{c,\gamma}$	$\Delta z^{\mathrm{Ti}}_{\gamma}$ (pm)
BTO/SRO/DSO	γ_1	1.10(1)	0.50(7)	0.64(3)	0.35(9)	0.04(4)	16
	γ_2	1.11(1)	0.88(6)	0.64(2)	0.56(7)	0.03(3)	12
	γ_3	1.11(1)	0.87(8)	0.63(2)	0.48(8)	0.02(3)	8
BTO/SRO/GSO	γ_1	1.05(1)	0.46(4)	0.54(3)	0.29(6)	-0.01(4)	-4
	γ_2	1.06(1)	0.88(3)	0.55(2)	0.32(5)	-0.01(3)	-4
	γ_3	1.04(1)	0.78(3)	0.56(1)	0.54(5)	0.02(2)	8
BTO/SRO/SSO	γ_1	1.08(2)	0.42(7)	0.63(6)	0.44(19)	0.05(8)	20
	γ_2	1.02(1)	1.00(3)	0.55(4)	0.41(12)	0.03(5)	12
	γ_3	1.02(1)	0.99(7)	0.56(2)	0.58(9)	0.04(3)	16

The XSW analysis presented here employs the computation of the reflectivity $R_0(E_\nu)$ with the assumption of either upward or downward average polarization of the BTO film, which is derived from PFM data (Section 4.6 and Table 4.2). For the reflectivity calculations, the positions of the Ba, Ti, and O atoms in the unit cell are taken from the known BTO bulk values [5]. The validity of the used model is demonstrated by the fact that both the reflectivity and yield data are well fitted. Indeed, Equation (2.3) provides a good fit for the experimental PE yields displayed in Figure 5.6, yielding $P^s_{c,\gamma}$ and $F^s_{c,\gamma}$, which are summarized in Table 5.3. $P^{\mathrm{Ba}}_{c,\gamma} \approx 1$ for Ba atoms and $P^{\mathrm{Ti}}_{c,\gamma} \approx 0.5$ for Ti atoms are obtained, as predicted from the atomic coordinates used to build the structural model in the XSW analysis. Their precise atomic positions change with sample and depth by nearly few tens of picometer with an error bar (averaged over γ) of 4 pm for Ba and 12 pm for Ti (Section A.7). The key physical quantity, for a displacive ferroelectric like BTO [127], is the displacement of Ti atoms from the center of the unit cell, denoted by $P^{\mathrm{Ba}}_{c,\gamma}$. This displacement is directly related to the ferroelectric polarization [128]. As a result, we compute $\Delta P^{\mathrm{Ti}}_{c,\gamma} = P^{\mathrm{Ti}}_{c,\gamma} - \left(P^{\mathrm{Ba}}_{c,\gamma} - 0.5\right)$ and the corresponding absolute central offset (in picometer) of Ti atoms $\Delta z^{\mathrm{Ti}}_{\gamma} = c_0 \Delta P^{\mathrm{Ti}}_{c,\gamma}$.

The Ti atomic displacements at various depths z from the BTO surface are obtained from XSW data at different exit angle ranges γ. The escape depths, for γ_1, γ_2, and γ_3, are $\lambda_{l,\gamma} = 3.4$ Å, 8.0 Å, 11.6 Å [2.7 Å, 6.4 Å, 9.2 Å] for Ba 4d [Ti 2p] photoelectrons at the (001) BTO Bragg energy E_B, respectively (Section 2.3). The corresponding probability yield functions $\rho_{\mathrm{yi}}(z)$ (Section 3.1), which are integrated over the three exit angle ranges γ_1, γ_2 and γ_3 (Figure 5.7a), show that $\Delta z^{\mathrm{Ti}}_{\gamma_1}$ relates primarily ($\approx 70\%$) to atoms within the first unit cell, while $\Delta z^{\mathrm{Ti}}_{\gamma_2}$ [$\Delta z^{\mathrm{Ti}}_{\gamma_3}$] mostly comes from $\rho_{\mathrm{yi}}(z)$-weighted average of atomic positions within the top 2 [3] unit cells. The remaining ($\approx 30\%$) contribution is accounted for the $\rho_{\mathrm{yi}}(z)$-weighted average of atomic positions from lower unit cells (Section 2.3). The depth-dependence of Ti atomic displacements $\Delta z^{\mathrm{Ti}}_{\gamma}$ (Table 5.3) is illustrated in Figures 5.7b-d by mapping them to the top three BTO unit cells. Particularly, the XSW fit outcomes of the BTO/SRO/DSO sample show positive $\Delta z^{\mathrm{Ti}}_{\gamma}$ values which decrease as γ increases. This is consistent with an upward ferroelectric polarization $\mathrm{P}^{\uparrow}$ with a decreasing amplitude from the surface to the bulk. On the other hand, the minimal offsets of $\Delta z^{\mathrm{Ti}}_{\gamma} < 0$ for γ_1 and γ_2, and $\Delta z^{\mathrm{Ti}}_{\gamma_3} > 0$, are revealed for the BTO/SRO/GSO sample. This suggests an upward polarization $\mathrm{P}^{\uparrow}$ at larger depths, which almost disappears with a gentle flip just below the

surface. Lastly, $\Delta z_{\gamma}^{\mathrm{Ti}} > 0$, corresponding to an upward polarization ($\mathrm{P}^{\uparrow}$), is found for every γ in the BTO/SRO/SSO sample.

We now turn our attention to the atomic coherent fractions. In all samples, the coherent fraction for Ba in the exit angle ranges of γ_2 and γ_3 is quite high ($F_{c,\gamma}^{\mathrm{Ba}} > 0.8$), suggesting a good structural order. Particularly, $F_{c,\gamma_2}^{\mathrm{Ba}}$ and $F_{c,\gamma_3}^{\mathrm{Ba}}$ are 1 in BTO/SRO/SSO, where no flip of ferroelectric polarization with depth is detected. The latter values are overestimated because, even in a perfectly ordered atomic layer, atomic vibrations at ambient temperature result in $F_c < 1$. There are two reasons why F_c can be overestimated. First, greater F_c are predicted without accounting for non-dipole effects because our XSW analysis does not include non-dipolar parameters, which are not available for p, d, and f initial states at this time [129]. Second, the count rate, XSW modulation amplitude, and resulting F_c may be overestimated as a result of the MCP's nonlinear behavior. On the other hand, depending on sample and γ, $F_{c,\gamma_2}^{\mathrm{Ba}}$ and $F_{c,\gamma_3}^{\mathrm{Ba}}$ values in BTO/SRO/DSO and BTO/SRO/GSO are around 0.88 and 0.78, respectively. The generally smaller coherent fraction of Ti atoms in the range of $0.3 - 0.6$ is also a result of the averaging over atoms in unit cells with varying polarizations. Moreover, both Ba and Ti atoms have a smaller coherent fraction of 0.3 to 0.5 for the most surface sensitive measurements at γ_1. The increased structural disorder caused by the interactions of atoms at the uppermost oxide plane with adsorbates is responsible for the generally lower $F_{c,\gamma}^{s}$ at the surface. In addition, we realize that the X-ray standing wave, that forms in the thin film, is the source of the structural accuracy of the XSW method and the small surface roughness of $\approx 0.84(8)$nm, which accounts for around 2 - 4 % of the film thickness has no impact on it. Greater surface roughness generally offers a wider surface area for different species to adsorb on compared to an atomically flat surface. The surface roughness cannot be the origin of differences in atomic positions in our samples because S_{RMS} is roughly constant across all samples (Table 4.2).

In addition, we tried applying the XSW analysis on O 1s components as well (data not shown), but, given the short time available for the experiments, only on the BTO/SRO/DSO sample. The lower photoionization cross section [130, 131] and the low statistics, however, caused a low signal level and large error bars in the PE yield profiles, which made it impossible to determine the corresponding structural parameters ($P_{c,\gamma}^{s}$, $F_{c,\gamma}^{s}$) with any degree of reliability.

Finally, the overall trend of the experimental yield profiles can be well described by the XSW yield fit curves, given the structural model that is

derived from the fit of the reflectivity data. Upon carefully examining the yield curves, oscillations with a periodicity of approximately 10 eV are detected (Figure 5.6). In the Ti(γ_3) data of the BTO/SRO/DSO and BTO/SRO/GSO samples, they are relatively evident. The potential origin of these features is now discussed. First, as explained in Section A.6, each data point is normalized by the corresponding X-ray intensity I_0, so oscillations of the incident X-ray intensity can be ruled out. Furthermore, Figure A.2b shows a few typical I_0 profiles without any oscillations. Second, intensity oscillations as a function of photon energy are typically observed in photoelectron diffraction and extended X-ray absorption fine structure (EXAFS). Nonetheless, it is reasonable to rule out these effects at this point because the oscillation period of about 10 eV would lead to unphysically large bond lengths [132]. Third, the reflectivity and yield curve oscillations that arise from beam interferences caused by a thin sample have the same periodicity. Therefore, the additional minor periodicity shown in part of our data cannot be explained by this. Fourth, oscillations in the reflectivity and yield curves are known to occur as a result of the deformation field in a crystal [100]. This is true when the deformation permeates the entire sample, as it happens, for example, when a sample bends [133]. On the other hand, the reflectivity is unaffected if the deformation field only affects a small part of the sample. However, the photoelectron yield can probe the deformed near-surface region with oscillations at a higher frequency than the ones of the reflectivity. As a result, we attribute the effect of a deformation field near the surface to the evident oscillations in the yield curves, which do not appear in the reflectivity. This is probably the result of a more intricate strain distribution, which is outside the scope of our basic structural models that only fully capture the major feature of the diffraction data. Furthermore, since the current models are based on reflectivity data, which obscures the higher frequency oscillations, it is not surprising that such minute oscillations in the yield curves are not replicated by them.

5.2. Discussion

The XSW data show that the absolute displacements of Ti atoms from the unit cell center ($\Delta z^{\mathrm{Ti}}_{\gamma_i}$) decrease from BTO/SRO/SSO, through BTO/SRO/DSO, to BTO/SRO/GSO. This trend does not correspond with the in-plane compressive strain $\epsilon^{a}_{\mathrm{BTO}}$. Alternatively, we interpret the observed off-center displacements

of Ti atoms in terms of oxygen-containing adsorbates near the surface. Water adsorbs on the BTO surface upon exposure to ambient conditions and splits into OH^- and H^+. H^+ binds to a lattice oxygen atom (O_L) at or below the surface to form O_LH^- [12–14, 119], while OH^- chemisorbs on top of cations (Ba or Ti) or at O vacancies [10–13]. To summarize, the depth-dependent O 1s XPS spectra (Section 5.1.2) indicate the presence of: (i) negatively charged chemisorbed O species, such as OH^- (hydroxyl groups) or $O_2{}^-$ (peroxo groups), represented by the component O(4); and (ii) O_LH^- species, which originate from a H^+ ion bound to a O_L, or a hydroxyl group adsorbed at an oxygen-vacancy site, represented by the component O(2). According to DFT calculations on the similar ferroelectric $PbTiO_3$ [9], positively charged H^+ atoms of O_LH^- species favor the downward polarization $P^\downarrow$, whereas negatively charged OH^- or $O_2{}^-$ molecules favor the upward polarization $P^\uparrow$, regardless of the surface termination.

The BTO film in the BTO/SRO/DSO sample displays upward polarization $P^\uparrow$ in the uppermost unit cells (Figure 5.7b) and downward average polarization $P^\downarrow$ (Section 4.6). As seen by component O(4) in Figure 5.4a, the upward polarization $P^\uparrow$ in the topmost unit cells is favored by negatively charged OH^- or $O_2{}^-$ molecules adsorbed on the surface. Specifically, the off-center displacement of Ti atoms decreases as they go from the surface into the bulk. This trend is consistent with a flip of the ferroelectric polarization below the top three unit cells, though it is beyond our XSW depth sensitivity. We conclude that there must be a concentration of positive charges at the polarization reversal interface for this configuration to be stable. Crucially, the depth dependence of component O(2) in this sample is in agreement with a distribution of O_LH^- species over approximately 4 unit cells (≈ 15 Å) below the surface (Figure 5.4d). This suggests that H^+ atoms are accumulating as a potential charge compensation mechanism for the polarization flip below the surface (Figure 5.7b). A similar scenario has been proposed by Lee and colleagues [13]. Their work utilized synchrotron X-ray crystal truncation rod experiments to determine the atomic positions throughout the BTO thin film. The existence of H^+ or defects was attributed to the rise in component O(2) upon water adsorption. Combining depth-dependent XSW, XPS, and PFM, we present the additional experimental evidence for the existence of a H^+-mediated polarization switching below the BTO surface in our investigation.

The BTO film in the BTO/SRO/GSO sample, in the most bulk-sensitive data ($\Delta z^{\mathrm{Ti}}_{\gamma_3} > 0$), shows an upward average polarization $P^\uparrow$ (Section 4.6), which is

consistent with a positive displacement of Ti atoms. On the other hand, a small polarization flip at the upper unit cells is indicated by the slightly negative displacement of Ti atomic positions observed in the more surface-sensitive data (Figure 5.7c). Figures 5.4b-d illustrate that, in contrast to the previous sample, O 1s XPS data in the BTO/SRO/GSO sample reveal that $O_L H^-$ species are restricted at the surface with concentrations comparable to those of OH^- or $O_2{}^-$ species. The interplay between positively charged H^+ atoms of $O_L H^-$ species that favor downward polarization $P^\downarrow$ and negatively charged OH^- or $O_2{}^-$ molecules that favor upward polarization $P^\uparrow$ is responsible for the small displacement of Ti atoms from the center of the unit cells at the surface, which results in a diminishing net polarization.

The BTO film in the BTO/SRO/SSO sample exhibits an upward average polarization $P^\uparrow$ (Section 4.6). Figure 5.7d shows a positive off-center displacement of Ti atoms throughout the top BTO unit cells. Under this situation, there would be an accumulation of positive bound charge near the surface, resulting in an upward polarization $P^\uparrow$. A compensatory negative screening charge at the surface is needed to stabilize this configuration. Large concentrations of negatively charged O species (OH^- and/or $O_2{}^-$) are visible in the O 1s XPS spectra (Figure 5.4c). According to DFT calculations [9], an upward polarization $P^\uparrow$ is favored by OH^- adsorbates and $O_2{}^-$ adatoms, which causes a greater offset of Ti atoms in the uppermost atomic plane. In comparison to deeper unit cells, our XSW data reveal a greater displacement of Ti atoms at the surface (20 pm), providing clear experimental support for this anticipated behavior.

At room temperature, single-domain BTO bulk crystals, with upward $P^\uparrow$ [downward $P^\downarrow$] polarization, have the displacement of Ti atoms of 5 pm above [below] the center of the unit cell, according to a neutron diffraction analysis [5]. In contrast, larger Ti atomic displacements are seen in the most bulk-sensitive XSW data $\Delta z_{\gamma_3}^{\mathrm{Ti}}$. Residual strain at the top sublayer can be used to explain this, since it results in larger out-of-plane lattice parameters c_0 compared to the bulk value $c_{b,\mathrm{BTO}}$, and thus larger atomic displacements. Furthermore, as demonstrated above, adsorbates have an impact on atomic positions near the surface. Depending on their kind and concentration, this might result in smaller (BTO/SRO/GSO) or higher (BTO/SRO/DSO and BTO/SRO/SSO) atomic displacements.

To sum up, the three samples under investigation differ in terms of thickness and in-plane compressive strain. However, the corresponding strain gradients

result in an average out-of-plane lattice parameter c_0 that is similar in the top sublayer of the BTO/SRO/GSO and BTO/SRO/SSO samples, and marginally smaller in the BTO/SRO/DSO sample. With the common outcome of screening the bulk polarization and stabilizing the ferroelectric thin film surface, each sample exhibits a unique distribution of ferroelectric polarization near the surface when exposed to ambient conditions. The available data indicates that the kind and concentration of adsorbates on the surface are correlated with the polarization profile at the top unit cells. The distribution of local polarization near the surface is the result of the interaction between bulk ferroelectric polarization and present adsorbates. Further research is needed to determine how much the adsorption of external species influences or is impacted by the polarization below the surface.

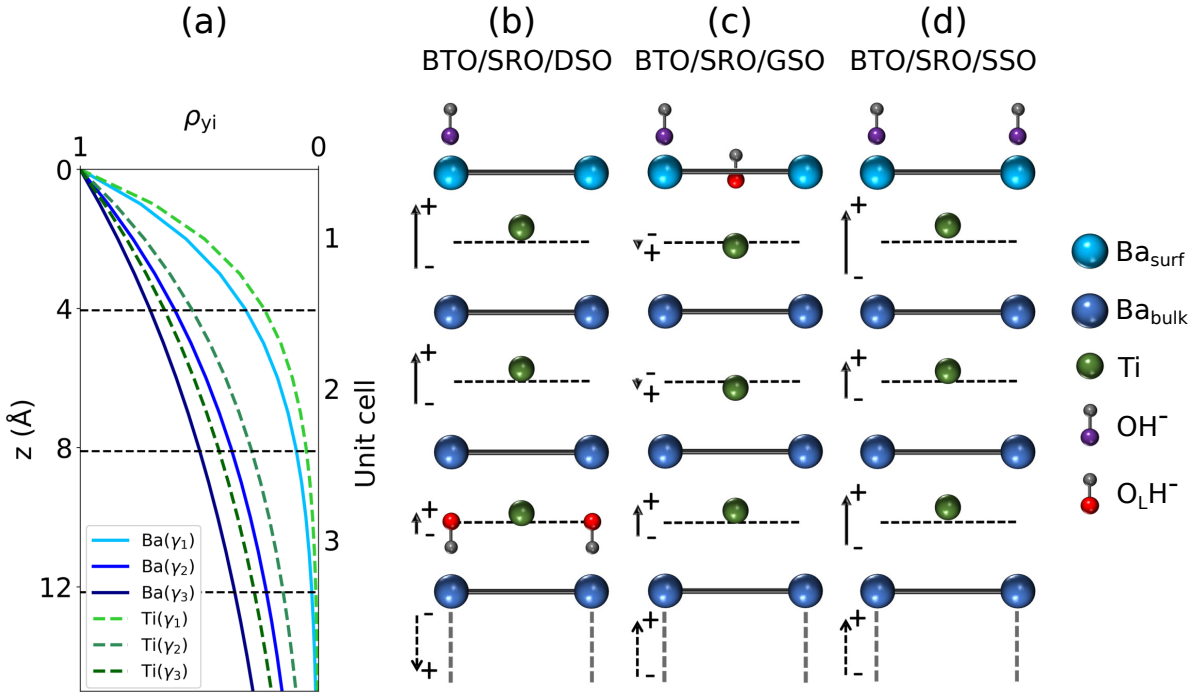

Figure 5.7.: Probability yield functions and schematic illustration of the top three unit cells of the samples under study. (a) Probability yield functions $\rho_{yi}(z)$ of Ba 4d and Ti 2p photoelectrons at $E_B = 1525\,\text{eV}$ integrated over the three exit angle ranges γ_1, γ_2 and γ_3. Schematic illustration of the top three unit cells of BTO/SRO/DSO (b), BTO/SRO/GSO (c), and BTO/SRO/SSO (d). The Ti atomic displacements Δz_γ^{Ti} shown in the scheme relate to the $\rho_{yi}(z)$-weighted average of atomic positions in various unit cells, with contributions determined in Section 2.3, rather than the atomic positions at the corresponding unit cell. Ti atomic displacements Δz_γ^{Ti} are twice as large as values in Table 5.3. The associated Δz_γ^{Ti} is proportional to the length of polarization vectors (solid arrows). Below the third unit cell, dashed arrows indicate the direction of the average ferroelectric polarization of BTO films as determined by PFM. The only external species that are sketched are OH^- and O_LH^-; O_2^- species and O_L atoms are not shown. As an illustration, the current scheme shows just BaO termination; however, our samples show mixed termination (BaO and TiO_2) (Section 4.3), and a similar scheme is valid also for TiO_2 termination.

6. Lattice and polarization dynamics in a ferroelectric thin film

When excited by optical pulses above the bandgap, both the electronic and lattice structures of a ferroelectric thin film undergo instantaneous changes. Understanding how intense optical pulses alter the photoexcited carrier density, leading to lattice distortion, enables precise control over strain and ferroelectric polarization at ultrafast timescales using light. To achieve this, we combine time-resolved XRD, SHG, and optical reflectance measurements to analyze the dynamics of lattice structure and ferroelectric polarization following the absorption of above-bandgap photons.

6.1. Results

6.1.1. Ultrafast photoinduced structural dynamics

The above-bandgap dynamics of the lattice structure in our ferroelectric thin film is probed by time-resolved XRD at the SCS Instrument of the European XFEL (Section 3.3). Our target sample is BTO/SRO*/GSO (Section 4.2), where the BTO thin film exhibits an in-plane compressive strain of $-0.63\,\%$ applied by the GSO substrate (Section 4.5), and has the ferroelectric polarization pointing outward from the sample surface. The incident X-ray photon energy is tuned between 1.5 and 1.6 keV to cover the (001) Bragg peak positions of BTO, SRO, and GSO. The (001) diffraction peaks of BTO (in the lower energy side), GSO (in the middle), and SRO (in the higher energy side) at different pump-probe delays t are shown in Figure 6.1a. Qualitatively, at larger pump-probe delays, there is an overall shift of the BTO peak to the lower energy direction, while the GSO and SRO peaks exhibit small fluctuations around their equilibrium positions.

Next, we turn our attention to the time evolution of the diffraction intensity

I_{XRD} around the BTO Bragg peak at the photon energy $E_\nu = 1525$ eV. Overall, the comparison between $I_{\mathrm{XRD}}(t > 2.6\,\mathrm{ps})$ and $I_{\mathrm{XRD}}(t < 2.6\,\mathrm{ps})$ reveals a shift toward lower photon energy, indicating an increase of the out-of-plane lattice parameter c. To clarify this observation, we calculate the average out-of-plane strain $\overline{\eta}(t)$ across the film thickness as a function of t. Specifically, $\overline{\eta}(t)$ is determined by the formula $\overline{\eta}(t) = [\overline{c}(t) - \overline{c}_0]/\overline{c}_0$, where $\overline{c}(t)$ and $\overline{c}_0$ are the lattice parameters derived from the center of mass of the (001) BTO Bragg peak (Section A.4). These parameters represent the average c at $t > 0$ and $t \leq 0$, respectively. Figure 6.1b illustrates the time evolution of $\overline{\eta}(t)$ for two incident fluences of 1.4 and 2.7 mJ cm^{-2}. At both fluences, $\overline{\eta}(t)$ exhibits a similar qualitative behavior. Initially, $\overline{\eta}(t)$ experiences a small decrease and reaches -0.024 % at around 2.6 ps for incident fluence 2.7 mJ cm^{-2} and -0.01 % at around 2.9 ps for incident fluence 1.4 mJ cm^{-2}. Second, there is a linear increase with a speed of 0.04 %/ps for 2.7 mJ cm^{-2} and 0.02 %/ps for 1.4 mJ/cm^2 between 4 ps and 10 ps. Lastly, the saturation of $\overline{\eta}(t)$ at 0.34 % and 0.2 % are observed for the incident fluences of 2.7 mJ cm^{-2} and 1.4 mJ cm^{-2}, respectively. The energy shifts of the SRO and GSO (001) Bragg peaks are significantly weaker than those of the BTO (001) Bragg peak. These energy shifts correspond to variations of average strain smaller than 0.05 % and 0.02 % for SRO and GSO, respectively.

We now focus on the dynamics of the BTO diffraction peaks. This behavior is characterized by variations in I_{XRD} near the peak and the shift of the peak's center of mass, which corresponds to changes in the lattice parameter c. To quantify this structural dynamics at the early timescale, we monitor the time evolution of $\Delta I_{XRD} = [I_{XRD}(t > 0) - \overline{I}_{XRD}(t < 0)]/\overline{I}_{XRD}(t < 0)$, with $I_{XRD}(t > 0)$ measured at the BTO peak photon energy E_ν = 1525 eV (Figure 6.1c). In the expression of ΔI_{XRD}, $\overline{I}_{XRD}(t < 0)$ is the average value of I_{XRD} measured before the arrival of the pump pulse, with $\Delta I_{XRD} = 0$ at equilibrium. In the delay range between 0 ps and 2.6 ps, two notable features are: (i) a drop of I_{XRD} near the peak, and (ii) a shift to higher photon energy, implying a decrease in c, which indicates out-of-plane lattice compression (Figure 6.2a). In the delay range from 2.6 ps to 4.9 ps, a recovery of I_{XRD} toward the equilibrium value and the onset of the out-of-plane lattice expansion are observed (Figure 6.2b). At incident fluence of 2.7 mJ cm^{-2}, a maximum drop of I_{XRD} of around 4 % ($\Delta I_{XRD} = -4\%$) is recorded at 3.18 ps. The diffraction intensity then recovers back to around 99 % ($\Delta I_{XRD} = -1\%$) at 7 ps. After 7 ps, the shift of the diffraction peak to lower photon energies leads to another decrease of I_{XRD}.

Upon the lower incident fluence of 1.4 mJ cm^{-2}, the maximum drop of I_{XRD} of around 1 % ($\Delta I_{XRD} = -1\%$) at 3.53 ps and the subsequent full recovery of I_{XRD} at around 7 ps are observed.

The initial decrease of 4 % and recovery in I_{XRD} are attributed to the displacements of atoms within the BTO unit cell (Figure 6.2c). Particularly, the dynamical theory of diffraction (Section 2.2) is employed to show that the decrease of experimental I_{XRD} at $E_\nu = 1525$ eV can be obtained by the reduction of 8 pm in the distance between the Ti atom and the center of the O octahedron, which is associated with the reduction in ferroelectric polarization (Figure 6.2a). The thermal disorder, indicated by the Debye-Waller factor, plays a negligible contribution to the decrease of I_{XRD} even at the maximum lattice temperature reached in these experiments (669 K, Section 6.1.2) (Figure 6.3). In addition, the non-monotonic decrease and increase in I_{XRD} between 0 ps and 7 ps cannot be explained by the monotonic increase of the lattice temperature due to the absorption of the optical pump energy.

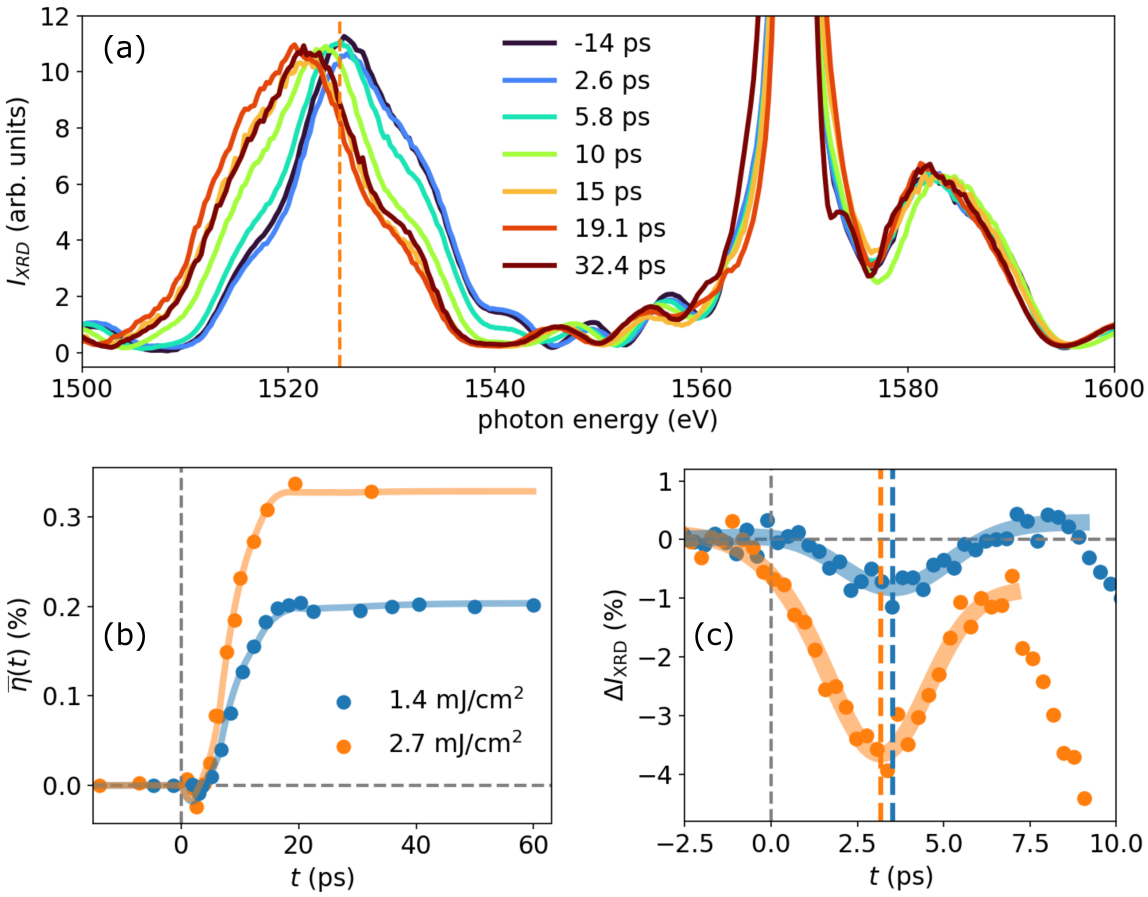

Figure 6.1.: Time-resolved XRD results of the BTO/SRO*/GSO sample. (a): Time-resolved (001) Bragg peaks of the BTO/SRO*/GSO sample at different time delays. The dashed orange line corresponds to $E_\nu = 1525\,\text{eV}$. (b): Average BTO out-of-plane strain $\overline{\eta}(t)$ as a function of pump-probe delay at the incident fluences of $1.4\,\text{mJ}\,\text{cm}^{-2}$ (blue) and $2.7\,\text{mJ}\,\text{cm}^{-2}$ (orange). The solid lines are fit curves based on the strain model discussed in Section 6.1.2. (c): Relative change of BTO peak diffraction intensity ΔI_{XRD} at $E_\nu = 1525\,\text{eV}$, with respect to the equilibrium value, measured at the incident fluences of $1.4\,\text{mJ}\,\text{cm}^{-2}$ (blue) and $2.7\,\text{mJ}\,\text{cm}^{-2}$ (orange). The dashed vertical lines refer to $t = 3.18\,\text{ps}$ and $t = 3.53\,\text{ps}$, while the solid lines are fit curves to the data.

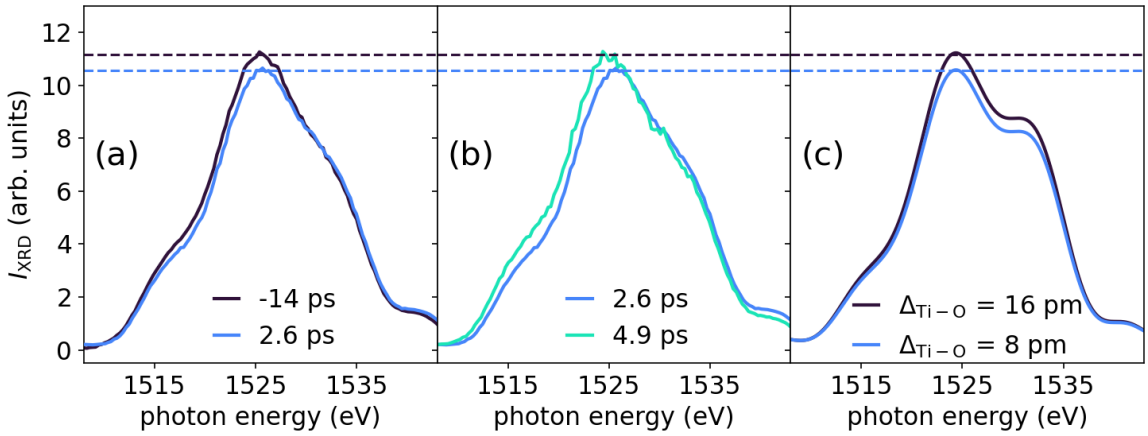

Figure 6.2.: Comparison between experimental and simulated diffraction curves with different atomic positions. (a-b): Experimental $I_{\mathrm{XRD}}(E_\nu)$ curves at fixed time delays $t = -14\,\mathrm{ps}, 2.6\,\mathrm{ps}$, and $4.9\,\mathrm{ps}$. (c): XRD simulations of BTO/SRO/GSO for $\Delta_{\mathrm{Ti}-0} = 16\,\mathrm{pm}$ and $8\,\mathrm{pm}$.

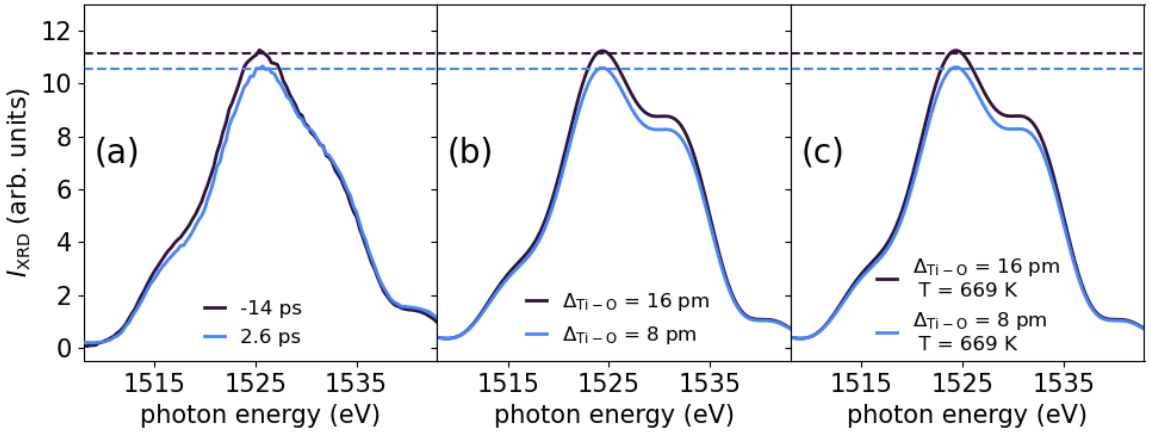

Figure 6.3.: Comparison between experimental and simulated diffraction curves at different temperatures. (a): BTO (001) diffraction peak of observed at $-14\,\mathrm{ps}$ and $2.6\,\mathrm{ps}$. (b): Simulated diffraction intensities illustrating the reduction in peak intensity with $\Delta_{\mathrm{Ti-O}} = 16\,\mathrm{pm}$ and $\Delta_{\mathrm{Ti-O}} = 8\,\mathrm{pm}$ at $T = 300\,\mathrm{K}$ (b) and $T = 669\,\mathrm{K}$ (c). Note the minimal difference between the diffraction profiles in panels b and c, indicating that the DW factor does not account for the changes in diffraction intensity shown in Figure 6.1c.

6.1.2. Strain model

To summarize, time-resolved XRD revealed an initial slight lattice compression, followed by a larger lattice expansion, which reaches the saturation after about 20 ps. This lattice dynamics is reminiscent of the change of c due to the static heating on a similar strained BTO/SRO*/GSO sample (Section 4.1.3 and [6]). In the latter experiment, the non-monotonic decrease and increase of c is associated with a sharp sign reversal of the out-of-plane linear expansion coefficient between negative $\beta_{T<T_c}$ and positive $\beta_{T>T_c}$ near the Curie temperature. Therefore, we wonder whether the photoinduced temperature increase of the lattice can explain the non-monotonic dynamics of lattice structure in our strained thin film.

When a material with bandgap E_g is exposed to an incident photon with energy $E > E_g$, this photon energy is first absorbed by the valence electrons. Subsequently, electrons are excited from the valence band to the conduction band. The electronic energy is then partially transferred to the phonon system by intraband electron-phonon coupling and partially converted to photon energy via a radiative decay process which takes a few hundred picoseconds or nanoseconds [134, 135]. The ultrafast energy transfer from electrons leads to an increase of the phonon temperature at the picosecond timescale. The mentioned energy exchange between the electron and phonon systems upon the absorption of optical laser pulses can be described by the two-temperature model (2TM), comprising of the following coupled differential equations:

$$\begin{aligned} C_e \frac{\partial T_e}{\partial t} &= -g(T_e - T_p) + S(z,t), \\ C_p \frac{\partial T_p}{\partial t} &= g(T_e - T_p). \end{aligned} \tag{6.1}$$

In these coupled equations, T_e and T_p are the temperatures of electron and phonon subsystems; C_e and C_p are volumetric heat capacities of electron and phonon subsystems; and g is the electron-phonon coupling constant. The source term $S(z,t)$ is proportional to the absorbed fluence of the pump laser. The solution of Equation (6.1) consists of the electron and phonon temperatures as a function of space and time denoted by $T_e(z,t)$ and $T_p(z,t)$. The detailed mathematical expressions of $T_e(z,t)$ and $T_p(z,t)$, as well as all used constants and parameters are reported in Section A.12.

We discuss now the validity of the two-temperature model employed here. The original coupled differential equations of the 2TM [136] contains also the

diffusion terms $K_e\partial^2 T_e/\partial z^2$ and $K_p\partial^2 T_p/\partial z^2$, where $K_e = C_e D_e$ and $K_p = C_p D_p$ are carrier and thermal conductivity, with D_e and D_p carrier and thermal diffusivity, respectively. These diffusion terms are negligible in the specific case of BTO because the parameters $D_e/(\nu\delta_{\mathrm{BTO}}) = 2.5 \times 10^{-5}$ and $D_p/(\nu\delta_{\mathrm{BTO}}) = 1.1 \times 10^{-2}$ are much smaller than unity [136]. The electron diffusion coefficient is computed from the Einstein relation $D_e = \mu k_B T/e = 2.6 \times 10^{-7}\,\mathrm{m^2\,s^{-1}}$, where $\mu = 0.1\,\mathrm{cm^2\,V^{-1}\,s^{-1}}$ is the electron mobility in BTO [137], k_B is the Boltzmann constant, T is the sample temperature and e is the elemental charge. In addition, the thermal diffusivity of BTO is $D_p = 1.11\,\mathrm{mm^2\,s^{-1}}$ [138]. Next, we discuss the volumetric heat capacities. The electron and phonon volumetric heat capacities of SRO and GSO are taken from [139, 140], assuming $T = 300\,\mathrm{K}$. This assumption is valid because GSO has nearly 0% transmittance for the 266 nm beam, and only 12% of the incident fluence is absorbed in the SRO thin film. For an absorbed fluence $F_{\mathrm{abs}} = 0.33\,\mathrm{mJ\,cm^{-2}}$, the maximum temperature increase [50] in SRO is $\Delta T = F_{\mathrm{abs}}^{\mathrm{SRO}}/(\delta_{\mathrm{SRO}} C_p^{\mathrm{SRO}}) = 55\,\mathrm{K}$, resulting in only a 2% increase in C_p. On the other hand, C_e increases by 18%, but its absolute value remains significantly smaller than C_p. The volumetric heat capacity C_p of BTO as a function of T is reported in [141]. Given its weak temperature dependence for $T > 300\,\mathrm{K}$, we use $C_p^{\mathrm{BTO}} = 2.8 \times 10^6\,\mathrm{J\,m^{-3}\,K^{-1}}$ and compute $\Delta T = F_{\mathrm{abs}}^{\mathrm{BTO}}/(\delta_{\mathrm{BTO}} C_p^{\mathrm{BTO}}) = 369\,\mathrm{K}$ and $\Delta T = 192\,\mathrm{K}$, for $F_{\mathrm{abs}}^{\mathrm{BTO}} = 1.88\,\mathrm{mJ\,cm^{-2}}$ and $F_{\mathrm{abs}}^{\mathrm{BTO}} = 0.98\,\mathrm{mJ\,cm^{-2}}$, respectively. Averaging C_p^{BTO} between 300 K and $300\,\mathrm{K} + \Delta T$ yields a consistent result of $C_p^{\mathrm{BTO}} = 2.8 \times 10^6\,\mathrm{J\,m^{-3}\,K^{-1}}$ [141]. To estimate C_e of BTO, we use data from similar titanates, e.g. $SrTiO_3$ [142] and $CaTiO_3$ [143], which show an average ratio $C_e/C_p = 0.015$ for the T ranges considered here. This results in $C_e^{\mathrm{BTO}} = 4.2 \times 10^4\,\mathrm{J\,m^{-3}\,K^{-1}}$. All other physical constants used in solving the 2TM, i.e., Equation (6.1)), are detailed in Section A.12 (Table A.2).

The photon absorption may modify the electronic system, which influences the interatomic potential, leading atomic movement and modification of E_g. The influence of the photon absorption on the lattice and electronic structure is characterized by the photoinduced stress σ with two sources: thermoelastic (TE) σ_{TE} and deformation potential (DP) σ_{DP}, respectively. The total stress experienced by the material can be written as:

$$\sigma = \rho v^2 \eta + \sigma_{TE}(T_p, \beta) + \sigma_{DP}\left(T_e, \frac{\partial E_g}{\partial p}\right), \tag{6.2}$$

where ρ is the mass density, v is the longitudinal speed of sound, and η is the mechanical strain of the material induced by the stress σ. In Equation (6.2), the dependence of the stress components on T_p, T_e, β and $\frac{\partial E_g}{\partial p}$ is reported. The pressure coefficient of bandgap $\frac{\partial E_g}{\partial p}$ denotes the modifications induced by the electronic pressure p on the bandgap E_g. In a thin film material, the propagation of strain wave, which is generated by the stress σ, along the entire thickness is governed by the following one-dimensional lattice strain wave equation:

$$\rho \frac{\partial^2 u(z,t)}{\partial t^2} = \frac{\partial \sigma(z,t)}{\partial z}, \tag{6.3}$$

where u is the atomic displacement and the relation between u and η is $\eta(z,t) = \frac{\partial u(z,t)}{\partial z}$. With the analytical solutions of $T_e(z,t)$ and $T_p(z,t)$ from Equation (6.1), Equation (6.3) provides the analytical solution of $\eta(z,t)$ (Section A.13)

In the next step, the average strain of the BTO layer $\overline{\eta}(t) = \int_0^{t_{\mathrm{BTO}}} \eta(z,t)dz/t_{\mathrm{BTO}}$, with fit parameters g, $\overline{\beta}_{T<T_c}$, and $\frac{\partial E_g}{\partial p}$, is utilized to fit the experimental data shown in Figure 6.1b, with fixed $\beta_{T>T_c}$ =1.4×10^{-5} calculated from Ref. [6]. Here, $\overline{\beta}_{T<T_c}$ is defined as the average β at $T < T_c$. The high quality of the fit in Figure 6.1b indicates that the structural dynamics observed experimentally at two different incident fluences by time-resolved XRD is well-represented by our proposed model. The full list of obtained fit parameters is reported in Table 6.1.

Table 6.1.: Results of the average strain fit. Results of the fit of the experimental $\overline{\eta}(t)$, measured at two different incident fluences F_{in}, with the strain model $\overline{\eta}(t, g, \partial E_g/\partial p, \overline{\beta}_{T<T_c})$.

F_{in} (mJ cm^{-2})	g (W m^{-3} K^{-1})	$\partial E_g/\partial p$ (J Pa^{-1})	$\overline{\beta}_{T<T_c}$ (K^{-1})
2.7 mJ cm^{-2}	1.2×10^{16}	-3.6×10^{-31}	3.0×10^{-6}
1.4 mJ cm^{-2}	5.3×10^{15}	-6.1×10^{-31}	8.7×10^{-6}

We now turn our attention to the resulting fit parameters. First, regarding the absolute values, the obtained coupling factors g are of a similar order of magnitude to those of metals [144]. In the ground state, BTO is an insulator with $E_g = 3.4$ eV, but laser absorption leads to charge transfer from the valence to the conduction band. The largest density of photoexcited carriers in the

conduction band N_e (Section A.13), corresponding to the obtained g factors (Table 6.1), are approximately $3.3 \times 10^{27}\,\mathrm{m}^{-3}$ and $1.7 \times 10^{27}\,\mathrm{m}^{-3}$, for incident fluences $2.7\,\mathrm{mJ\,cm}^{-2}$ and $1.4\,\mathrm{mJ\,cm}^{-2}$, respectively (Figure 6.4). These transient electron densities are one order of magnitude smaller than those of metals. The electron density in metal is calculated as $N_e^{metal} = n_e \rho N_A / M$ [145] where ρ is the mass density, n_e is the number of conduction electrons per atom, $N_A = 6.022 \times 10^{23}\,\mathrm{atoms/mol}$ is the Avogadro's number [146], and M is the atomic mass. As an example, for Cu ($\rho = 8.96\,\mathrm{g\,m}^{-3}$ [147], $M = 63.55\,\mathrm{g\,mol}^{-1}$ [147], and $n_e = 1$ [147]), the electron density is N_e^{Cu} $=8.49 \times 10^{28}\,\mathrm{m}^{-3}$. Additionally, a simple approximation suggests a linear dependence of the g factor on the electron number density [144], which is proportional to the incident fluence. In fact, the fit results show similar ratios between the g factors and the incident fluences. Concerning the pressure coefficient of the bandgap, $\partial E_g / \partial p$, the negative sign indicates a decrease in the bandgap with increasing electronic pressure, resulting from the increase in photoexcited carrier population [51]. This decrease in the band gap exposed to optical illumination is actually predicted by a recent RT-TDDFT computation by Chen and coworkers [148]. These fit results for $\partial E_g / \partial p$ are validated by the fluence dependence of the fast relaxation time, which is discussed later in Section 6.1.3.

Regarding the average out-of-plane linear expansion coefficient below T_c, i.e., $\overline{\beta}_{T<T_c}$, the fit of the data at the two incident fluences provides positive values, both smaller than $\beta_{T>T_c}$. To interpret this, we refer to the results of the static heating of a similar thin film performed by Choi and his colleagues [6]. Below $T_c = 420\,^\circ\mathrm{C}$, the temperature evolution of c is not monotonic and can be divided into two stages: an increase in c from room temperature to $T^* = 260\,^\circ\mathrm{C}$ and a decrease in c from T^* to T_c (Figure 6.5a). Figures 6.5b-c show the lattice temperature ranges of our BTO thin film as a function of time for incident fluences of $2.7\,\mathrm{mJ\,cm}^{-2}$ and $1.4\,\mathrm{mJ\,cm}^{-2}$, respectively. These temperature regions extend between the lattice temperatures at the BTO surface ($z = 0$) and at the BTO/SRO interface ($z = t_{\mathrm{BTO}}$). Because the temperature is not linearly distributed in the thickness, Figures 6.5b-c display curves that indicate the lattice temperatures at evenly spaced depths between $z = 0$ and $z = t_{\mathrm{BTO}}$.

For incident fluence $1.4\,\mathrm{mJ\,cm}^{-2}$, the sample does not reach T_c and more than $4/5$ of the sample is in the temperature range below T^* characterized by $\beta_{T<T_c} > 0$. As expected, our fit results provide a positive value of $\overline{\beta}_{T<T_c}$ for $1.4\,\mathrm{mJ\,cm}^{-2}$. For incident fluence $2.7\,\mathrm{mJ\,cm}^{-2}$, at time delays corresponding to

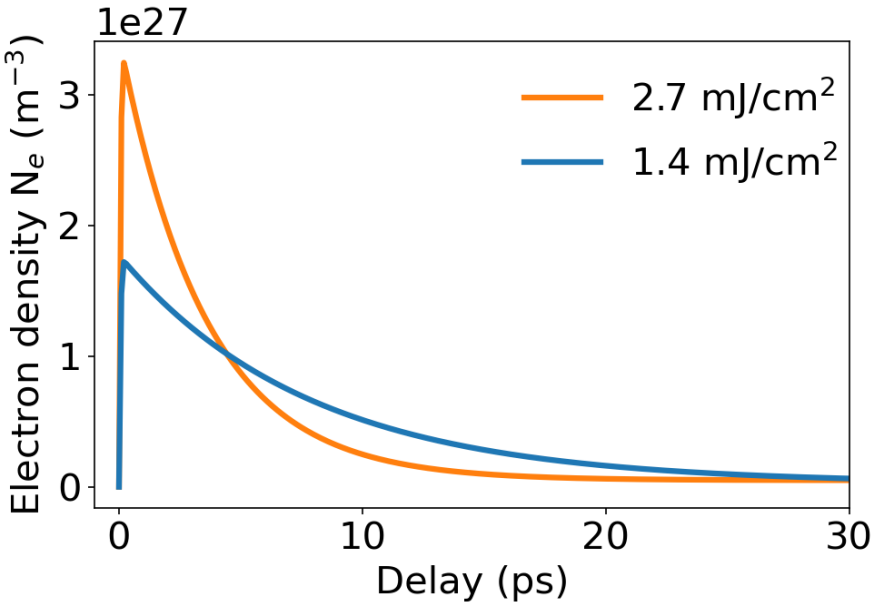

Figure 6.4.: Density of photoexcited carriers. The densities of photoexcited carriers, averaged over the BTO film thickness, at the incident fluences of 2.7 mJ cm^{-2} and 1.4 mJ cm^{-2}.

the strain saturation, i.e., $t > 20$ ps, only about 1/5 of the sample is above T_c, 1/5 at $T^* < T < T_c$ and 3/5 at $T < T^*$. Obviously, the temperature region with $\beta_{T<T_c} > 0$ is still larger than that with $\beta_{T<T_c} < 0$, but the difference between these two regions in the 2.7 mJ cm^{-2} case is smaller than the corresponding value in the 1.4 mJ cm^{-2} case. This explains why we obtain a positive average $\overline{\beta}_{T<T_c}$ for 2.7 mJ cm^{-2}. However, since it results from an average over positive and negative β, its magnitude is smaller than $\overline{\beta}_{T<T_c}$ at 1.4 mJ cm^{-2}, where only a minor contribution of negative β plays a role.

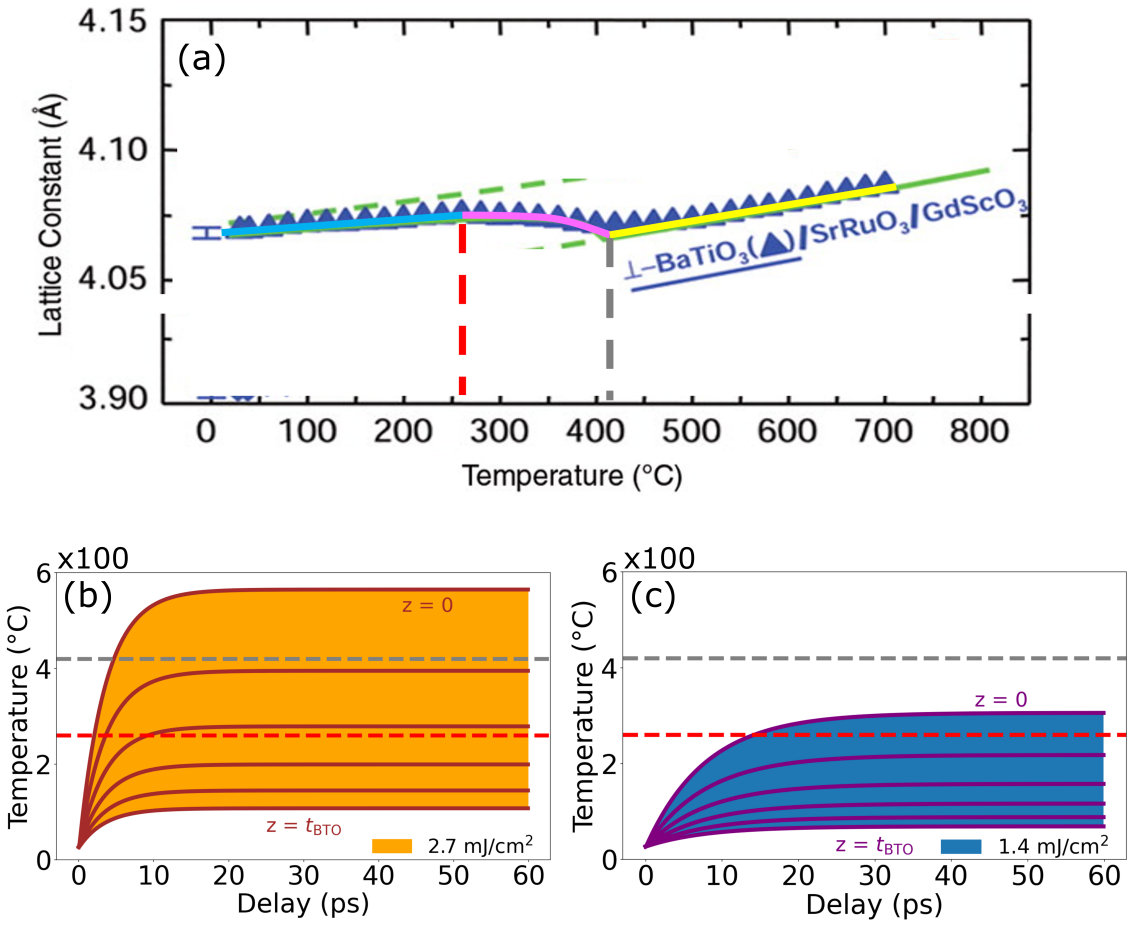

Figure 6.5.: Temperature dependence of the c parameter of a $BaTiO_3/SrRuO_3/GdScO_3$ sample and simulated lattice temperature profiles at the different incident fluences. (a): Temperature dependence of the c parameter of the $BaTiO_3/SrRuO_3/GdScO_3$ sample. This figure is re-adapted from [6]. The light blue, pink, and yellow bars indicate the temperature regions with the positive $\beta_{T<T_c}$, the negative $\beta_{T<T_c}$, and the positive $\beta_{T>T_c}$, respectively. (b): The lattice temperature range of the BTO thin film for incident fluence 2.7 mJ cm^{-2} (orange). The brown curves indicate the lattice temperature at different depths $z = 0, t_{\mathrm{BTO}}/5, 2t_{\mathrm{BTO}}/5, 3t_{\mathrm{BTO}}/5, 4t_{\mathrm{BTO}}/5, t_{\mathrm{BTO}}$, from the top to the bottom. (c): The lattice temperature range of the BTO thin film for incident fluence 1.4 mJ cm^{-2} (blue). The purple curves indicate the lattice temperature at different depths $z = 0, t_{\mathrm{BTO}}/5, 2t_{\mathrm{BTO}}/5, 3t_{\mathrm{BTO}}/5, 4t_{\mathrm{BTO}}/5, t_{\mathrm{BTO}}$, from the top to the bottom. The red and gray dashed lines indicate T^* and T_c in all panels, respectively.

The obtained fit parameters are employed to calculate the lattice temperature $T_p(z,t)$ using Equation (6.1). Figures 6.8a and 6.9a indicate the spatial profile of the lattice temperature of the BTO layer as a function of the time delay upon the optical pump fluences of 2.7 mJ cm^{-2} and 1.4 mJ cm^{-2}, respectively. After the arrival of the pump ($t > 0$), the lattice temperature increases gradually in time and space. For $F_{in} = 2.7\,\mathrm{mJ\,cm^{-2}}$, part of the BTO film near the surface hits T_c at around 5 ps, indicated by the white curve. A larger portion of the thin film reaches T_c at larger time delays. After around 20 ps, the thermal penetration saturates. At this point, 17 % of the BTO thin film is above T_c (Figure 6.8a). For $F_{in} = 1.4\,\mathrm{mJ\,cm^{-2}}$, the entire sample is heated up gradually but there is no portion of the thin film reaching T_c (Figure 6.9a).

We proceed to calculate the spatial strain profile $\eta(z,t)$ as a function of the time delay for both the fluences employed in this work (Figures 6.8b and 6.9b). As previously mentioned, the average thermal expansion coefficients below and above T_c, used to calculate $\eta(z,t)$, are both positive. This is because the majority of the sample resides in the temperature region where the thermal expansion coefficient is positive for both incident fluences [6].

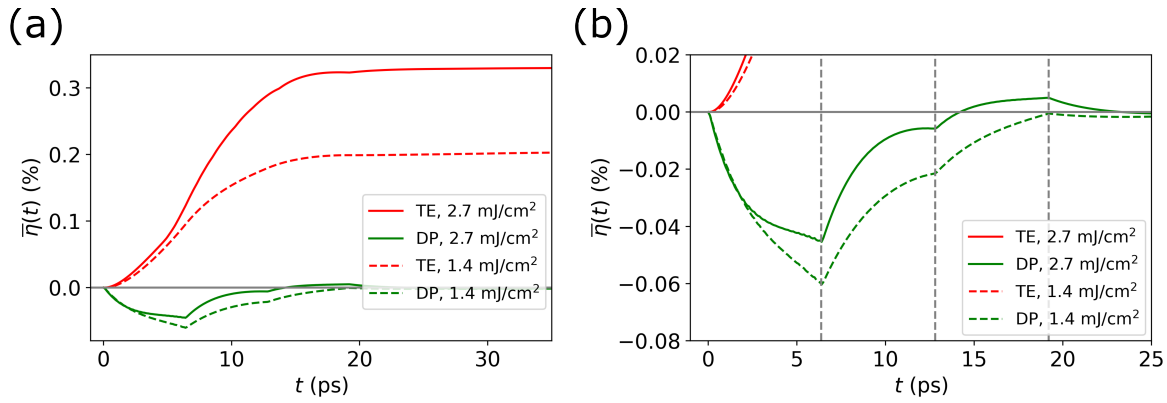

Figure 6.6.: Strain contributions from TE and DP mechanisms at different incident fluences. (a): Strain contributions from TE (red lines) and DP (green lines) mechanisms at fluences of $F_{\mathrm{in}} = 2.7\,\mathrm{mJ\,cm^{-2}}$ (solid lines) and $F_{\mathrm{in}} = 1.4\,\mathrm{mJ\,cm^{-2}}$ (dashed lines). (b): The same plot as in panel (a), but focusing on the strain range $-0.02\% < \overline{\eta}(t) < 0.01\%$ and delay range $-1\,\mathrm{ps} < t < 25\,\mathrm{ps}$. The gray dashed lines at 6.4 ps, 12.8 ps, and 19.2 ps indicate discontinuities in the DP strain profile caused by reflections of the DP strain wave at the BTO/SRO, BTO/air, and BTO/SRO interfaces, respectively. The time constants are derived from the speed of sound in BTO (A.2) and the distances traveled, corresponding to times t, $2t$, and $3t$.

At the incident fluence of 2.7 mJ cm^{-2}, the entire sample experiences a weak tensile strain $\eta > 0$ up to 5 ps due to the small positive $\overline{\beta}_{T<T_c}$ (Figure 6.8b). Around 5 ps, the near-surface part of the BTO film that crosses T_c is under higher tensile strain $\eta > 0$, resulting from the high positive $\beta_{T>T_c}$, while the deeper part of the film remains on average under weak tensile strain. The expansion of the sample region under larger tensile strain saturates after 20 ps, at which 6 nm thickness of BTO from the surface ($z = 0$) is above T_c. Figure 6.8c shows the individual strain profiles along the thickness of the BTO film at different pump-probe delays for the pump fluence of 2.7 mJ cm^{-2}. The sample region with high tensile strain is confined within the depth of 6 nm from the film surface due to the saturation of the thermal expansion. The maximum tensile strain at this fluence is around 1.6 %. Figure 6.6 indicates the simulated contributions from TE and DP to the average strain $\overline{\eta}(t)$ at fluences 2.7 mJ cm^{-2} and 1.4 mJ cm^{-2}. Due to the positive thermal expansion coefficients both below and above T_c obtained from the fit (Table 6.1), the contribution from TE is always positive. Conversely, the negative pressure coefficient of the bandgap $\partial E_g/\partial p$ results in the negative contribution from DP.

At the incident fluence of 1.4 mJ cm^{-2}, the entire thin film remains in a weak tensile strain regime (Figure 6.9b). Figure 6.9c shows the individual strain profiles along the thickness of the BTO film at different pump-probe delays for the pump fluence of 1.4 mJ cm^{-2}. The maximum tensile strain of 0.4 % achieved at this fluence is approximately a quarter of that achieved at 2.7 mJ cm^{-2} (Figures 6.8c and 6.9c). Regarding the simulated contributions from TE and DP to the average strain $\overline{\eta}(t)$, similar to the case of 2.7 mJ cm^{-2}, there are the positive contribution from TE and the negative contribution from DP for 1.4 mJ cm^{-2} (Figure 6.6). In addition, the contribution from DP for 1.4 mJ cm^{-2} is slightly larger than that for 2.7 mJ cm^{-2} (Figure 6.6a). This is attributed to a larger absolute value of $\partial E_g/\partial p$ for 1.4 mJ cm^{-2} than that for 2.7 mJ cm^{-2} (Table 6.1). In particular, the discontinuities at 6.4 ps, 12.8 ps, and 19.2 ps in the DP strain profile are due to reflections of the DP strain wave at the BTO/SRO, BTO/air, and BTO/SRO interfaces, respectively (Figure 6.6b).

Most importantly, it is evident that by adjusting the incident fluence and the thickness of the thin film, we can control the optomechanical strain profile, influencing both the maximum average strain and the strain distribution within the ferroelectric thin film. For example, Figure 6.7 indicates the average strain $\overline{\eta}$ as a function of the BTO thickness t_{BTO} for an incident fluence of 2.7 mJ cm^{-2}. A smaller thickness leads to a larger average strain.

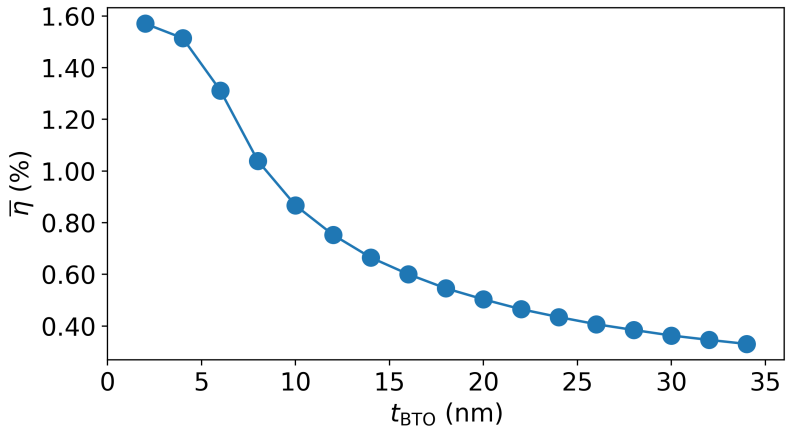

Figure 6.7.: Relation between average strain and BTO film thickness. Average strain $\overline{\eta}$ as a function of the BTO thickness t_{BTO} for the incident fluence of 2.7 mJ cm^{-2}.

The last step consists of comparing experimental diffraction curves with the simulated ones derived from the strain profiles presented above. The out-of-plane lattice constant $c(z,t)$ of each unit cell can be determined from $\eta(z,t)$. From this, the dynamical theory of diffraction (Section 2.2) is employed to calculate the individual diffraction patterns at different time delays t, as well as the time evolution of diffraction patterns $I_{XRD}(E_\nu,t)$ in a 2D map between 0 ps and 20 ps, at both incident fluences (Figures 6.8e-f and 6.9e-f). These simulated diffraction curves are then compared with the experimental ones at the corresponding time delay t (Figures 6.8d and 6.9d). The following features are well reproduced by the simulated diffraction curves: (i) the peak shift to lower photon energies, (ii) the relative modulation of I_{XRD} on the low and high energy sides of the diffraction peaks, and (iii) the ratio of the peak shift over the incident fluence (Figures 6.8e and 6.9e). These are further evidences that corroborate the validity of our proposed model.

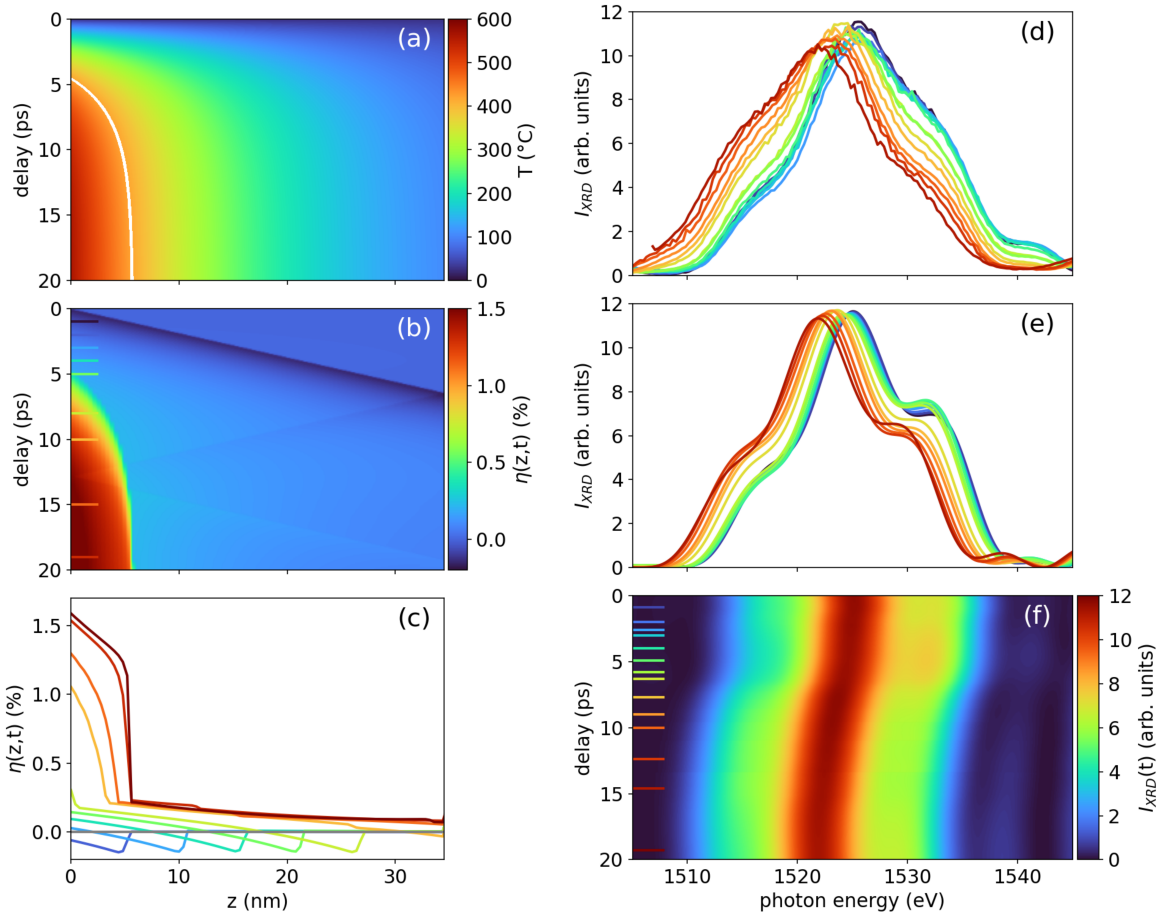

Figure 6.8.: Simulation results of $T_p(z,t)$, $\eta(z,t)$, and $I_{XRD}(E_\nu,t)$ at the incident fluence of $2.7\,\mathrm{mJ\,cm^{-2}}$ **based on the fit results of $\overline{\eta}(t)$.** (a) Simulated time evolution of $T_p(z,t)$ displayed in a 2-dimensional map. The color indicates the amplitude of the lattice temperature and the white curve indicates T_c. (b) Simulated time evolution of $\eta(z,t)$ displayed in a 2-dimensional map. The color indicates the amplitude of the strain. (c) The individual strain curves at different pump-probe delays of 1 ps, 2 ps, 3 ps, 4 ps, 5 ps, 8 ps, 10 ps, 15 ps, and 19 ps corresponding to the terminated dashed lines in (b). (d) The experimental XRD intensity around the (001) Bragg peaks of the BTO film measured at different pump-probe delays including -7.2 ps, 0.9 ps, 2 ps, 2.6 ps, 3 ps, 4 ps, 4.9 ps, 5.8 ps, 6.3 ps, 7.7 ps, 9 ps, 10 ps, 12.4 ps, 14.6 ps, and 19.3 ps. (e) The simulated XRD intensity around the (001) Bragg peaks of the BTO film measured at the corresponding pump-probe delays. (f) Simulated time evolution of the XRD patterns around the (001) Bragg peaks of the BTO film $I_{XRD}(E_\nu,t)$ displayed in a 2-dimensional map. The color indicates the XRD intensity.

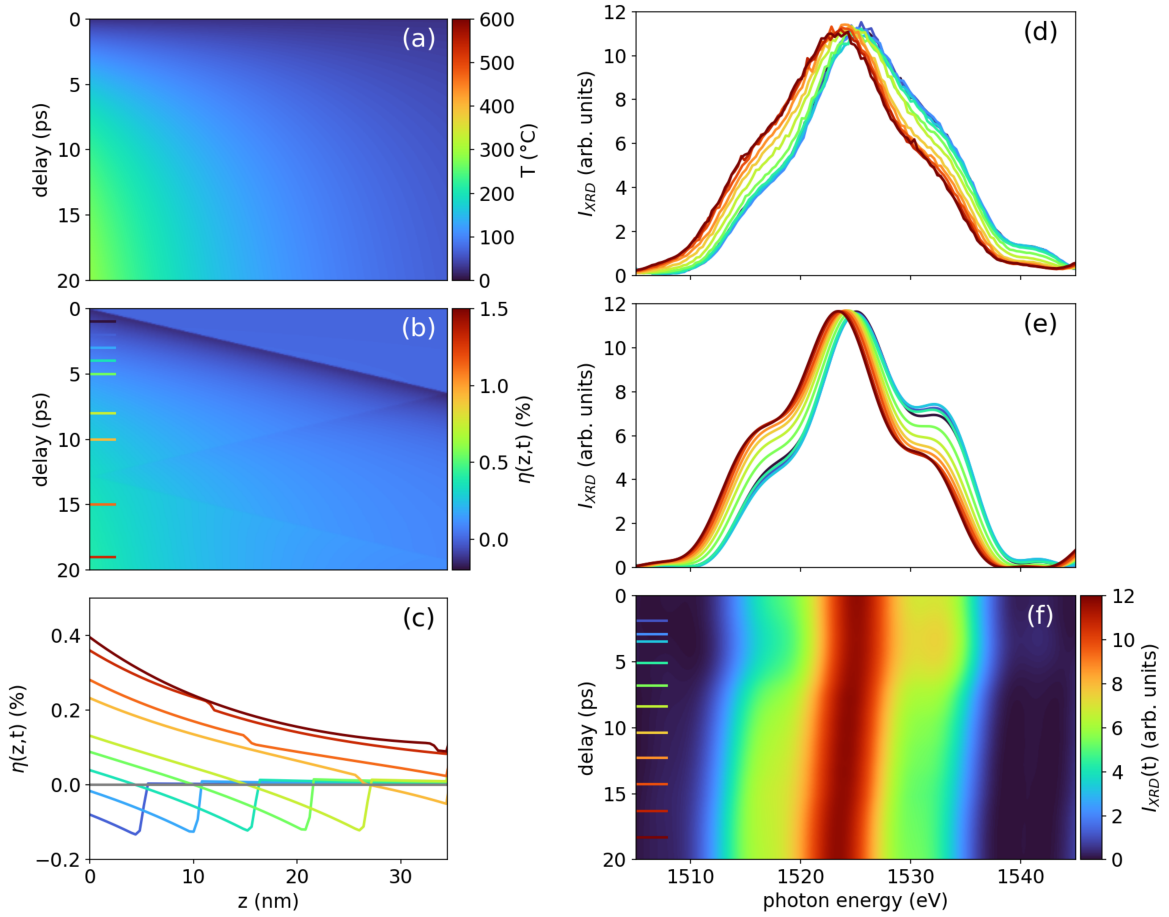

Figure 6.9.: Simulation results of $T_p(z,t)$, $\eta(z,t)$, and $I_{XRD}(E_\nu,t)$ at the incident fluence of $1.4\,\mathrm{mJ\,cm^{-2}}$ **based on the fit results of $\overline{\eta}(t)$.** (a) Simulated time evolution of $T_p(z,t)$ displayed in a 2-dimensional map. The color indicates the amplitude of the lattice temperature. (b) Simulated time evolution of $\eta(z,t)$ displayed in a 2-dimensional map. The color indicates the amplitude of the strain. (c) The individual strain curves at different pump-probe delays of 1 ps, 2 ps, 3 ps, 4 ps, 5 ps, 8 ps, 10 ps, 15 ps, and 19 ps corresponding to the terminated dashed lines in (b). (d) The experimental XRD intensity around the (001) Bragg peaks of the BTO film measured at different pump-probe delays including -4.7 ps, 1.9 ps, 2.9 ps, 3.5 ps, 5.1 ps, 6.8 ps, 8.4 ps, 10.4 ps, 12.3 ps, 14.3 ps, 16.3 ps, and 18.3 ps. (e) The simulated XRD intensity around the (001) Bragg peaks of the BTO film measured at the corresponding pump-probe delays. (f) Simulated time evolution of the XRD patterns around the (001) Bragg peaks of the BTO film $I_{XRD}(E_\nu,t)$ displayed in a 2-dimensional map. The color indicates the XRD intensity.

Although the experimental average strain $\overline{\eta}$ as a function of delay is accurately captured by our strain model (Figure 6.1), our simulations do not perfectly match the experimental data regarding the curve broadening (Figures 6.8d-e and 6.9d-e). The broadening of the diffraction curve I_{XRD}, which is associated with the strain gradient in the sample, is estimated by c_{std}, i.e., the standard deviation of c parameters (Section A.4). Because the exact strain gradient profile of our sample in the ground state is unknown, an exact match of c_{std} between experiments and simulations is not anticipated. Our simulations assume no strain gradient in the ground state, i.e., $\eta(z, t = 0\,\mathrm{ps}) = 0$, while the broader experimental I_{XRD} curve indicates an existing strain gradient profile $\eta(z, t = 0\,\mathrm{ps}) \neq 0$ (Figure 6.10). Specifically, prior to the arrival of the pump laser, $c_{\mathrm{std}}^{exp} = 1.80\,\mathrm{pm}$ for the experimental curve and $c_{\mathrm{std}}^{sim} = 1.65\,\mathrm{pm}$ for the simulated curve (Figure 6.10). Furthermore, the differences between experimental and simulated c_{std}, i.e., $\Delta c_{\mathrm{std}} = c_{\mathrm{std}}^{exp} - c_{\mathrm{std}}^{sim}$, is typically less than $0.2\,\mathrm{pm}$ and $0.1\,\mathrm{pm}$ for $F_{\mathrm{in}} = 2.7\,\mathrm{mJ\,cm^{-2}}$ and $F_{\mathrm{in}} = 1.4\,\mathrm{mJ\,cm^{-2}}$, respectively. These minor differences, coupled with the similar qualitative behavior of Δc_{std} over time, confirm the validity of our strain model.

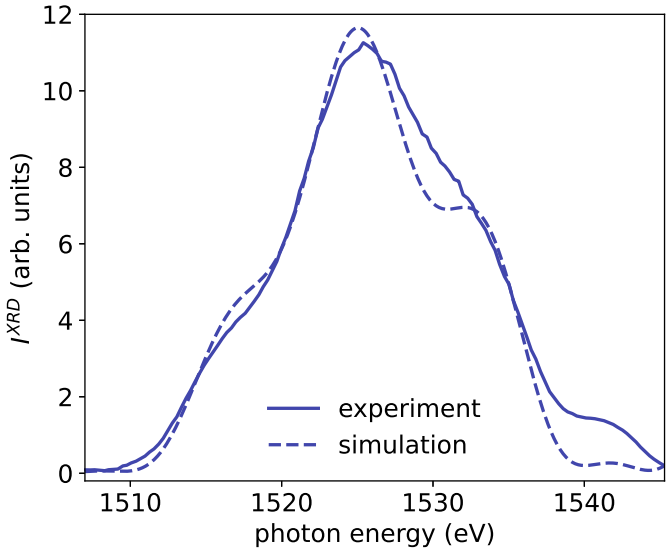

Figure 6.10.: Comparison of simulated and experimental diffraction curves before laser excitation. The broadening of I_{XRD} curves is represented by c_{std}. In this case, $c_{\mathrm{std}} = 1.80\,\mathrm{pm}$ and $1.65\,\mathrm{pm}$ for the experimental (solid line) and simulated (dashed line) curves, respectively. This results from a slightly greater broadening of the experimental I_{XRD} curve due to the presence of an initial strain profile $\overline{\eta} \neq 0$, whereas $\overline{\eta} = 0$ for the simulated I_{XRD} curve.

6.1.3. Photoinduced dynamics of electronic structure and ferroelectric polarization

The photoinduced dynamics of the lattice structure upon the 4.66 eV optical excitation has been presented in Section 6.1.1 with XRD as a probe. We now use optical reflectance and SHG as probes to characterize the dynamics of the electronic system near the Fermi level and the ferroelectric polarization. The setup of the time-resolved optical reflectance and SHG is described in details in Section 3.2. In this setup, optical reflectance and SHG can be measured simultaneously utilizing the same pump laser used in the time-resolved XRD experiments.

The transient change in the optical reflectance is calculated as $\Delta R/R = [R(t) - R_0]/R_0$, where $R(t)$ and R_0 are the optical reflectance at $t > 0$ and $t \leq 0$, respectively (Figures 6.11a-b). In addition, the polar SHG patterns in P-out and S-out configuration I^p_{SHG} and I^s_{SHG} are measured at different pump-probe delays to reveal the potential symmetry changes upon pumping. Subsequently, the transient change in the SHG intensity is calculated as $\Delta I^s_{\mathrm{SHG}}/I^s_{\mathrm{SHG}} = [I^s_{\mathrm{SHG}}(t) - I^s_{\mathrm{SHG,0}}]/I^s_{\mathrm{SHG,0}}$, where $I^s_{\mathrm{SHG}}(t)$ and $I^s_{\mathrm{SHG,0}}$ are the S-out SHG intensity at $t > 0$ and $t \leq 0$, respectively, at the incident polarization rotation $\phi = 45^\circ$ (defined in Section 2.4). The time traces of both $\Delta R/R$ and $\Delta I^s_{\mathrm{SHG}}/I^s_{\mathrm{SHG}}$ are fitted by the same function (Section A.9) characterized by one rise time τ_0, and two recovery times τ_1 and τ_2.

We first present the photoinduced dynamics of the electronic system probed by the optical reflectance. The absorption of above-bandgap optical pulses increases the photoexcited carrier density, resulting in the increase in the optical reflectance. The maximum $\Delta R/R$ of around 6 % is achieved after 150 fs at the incident fluence of 2.7 mJ cm^{-2} (Figure 6.11a). The photoexcited electrons, which are located high above the conduction band, are thermalized via electron-electron scattering within tens of femtoseconds and exchange their energy with the phonon subsystem via electron-phonon coupling in the timescale of a few hundred femtoseconds up to a few picoseconds. Consequently, these electrons experience an intraband relaxation to the bottom of the conduction band. This non-radiative relaxation is characterized by the first recovery time constant $\tau_1 = 5.5$ ps (Figure 6.11a). Subsequently, the energy transferred from the electron to the phonon subsystem during the intraband relaxation, which is equal to or smaller than the excess energy of photoexcited electrons, $E - E_g \leq 1.26$ eV [149], causes the increase of the lattice temperature. The accumulation

of photoexcited carriers near the gap edges and lattice temperature increase lead to the photoinduced stress σ characterized by the deformation potential (σ_{DP}) and thermoelastic (σ_{TE}) terms, respectively (Section 6.1.2). In other words, these instantaneous sources of stress lead to the conversion of pump photon energy into mechanical energy, generating acoustic strain waves. The propagation of acoustic pulses along the film thickness modifies the refractive index of the lattice which may cause changes and coherent oscillations in $\Delta R/R$ [50]. In the following, we discuss how these aspects relate to our data.

There have been several studies on the variation of the transient optical reflectance due to the propagation of the acoustic waves within the materials [51, 150–152]. As the acoustic pulse is partially reflected from thin film surface and interface, there may be successive echo pulses on the time trace of $\Delta R/R$, if there is a considerable acoustic reflection coefficient R_Z between two consecutive layers [50, 51] (Section A.13). However, these echoes are not observed in our case because the acoustic impedances of BTO and SRO films are very similar, with the reflection coefficient $R_Z^{BTO/SRO} \approx 10\%$ (Section A.13). In addition, the optical reflectance may experience periodic modulation, i.e., coherent oscillations, as a result of the interference between the probe light reflected from the surface of the sample and the light reflected from the strain pulse as it propagates [50, 150]. These coherent oscillations may be visible if the traveling time of the acoustic pulse within the thin film is larger than the oscillation period $T_{osc} = \lambda_{probe}/(2n(\lambda_{probe})v_{BTO})$. However, in our thin film, it takes around 6.4 ps for the strain pulse to leave the BTO film which is even less than quarter an oscillation period of the acoustic coherent phonon $T_{osc} = 31\,\mathrm{ps}$ [50]. Here, λ_{probe} = 800 nm is the probe wavelength, $n(\lambda_{probe}) = 2.4$ is the refractive index at λ_{probe} [153], and $v_{BTO} = 5399\,\mathrm{m\,s^{-1}}$ is the longitudinal sound speed in BTO film (Section A.12).

In the next step, the light induced dynamics of the ferroelectric polarization probed by SHG is presented (Figure 6.11c-d). To interpret the time evolution of I_{SHG}, we employ the relation $I_{SHG}(t) \propto \chi^2_{ijk}(t) \propto |P_s(t)|^2$ (Section 2.4), with

$$P_s(t) = \frac{1}{V}\sum_i q_i(t)\Delta z_i(t), \tag{6.4}$$

where V is the volume of the unit cell, $q_i(t)$ is the Born effective charge and $\Delta z_i(t)$ is the out-of-plane displacement of atom i.

Within the pulse duration of approximately 70 fs, the above-bandgap photoexcitation transfers electrons from occupied O 2p orbitals to unoccupied Ti

3d orbitals. This charge transfer results in the reduction in the effective charge $q_i(t)$ at both O and Ti sites. In this femtosecond timescale, the atoms have not moved yet and thus the out-of-plane atomic displacement remains unchanged. As a result, the rise time τ_0 of $\Delta R/R$ and $\Delta I^s_{\mathrm{SHG}}/I^s_{\mathrm{SHG}}$ are almost identical because those are both driven by the electronic redistribution. The maximum drop of $\Delta I^s_{\mathrm{SHG}}/I^s_{\mathrm{SHG}}$ of 10 % is achieved after 170 fs (Figure 6.11c). After the charge transfer, photoexcited electrons experience the initial relaxation from the Ti 3d to the O 2p orbitals, revealed by the decrease of $\Delta R/R$. This is associated with an increase in $q_i(t)$ in the first 2 ps. The fact that Ti and O atoms move toward each other revealed by the drop in I_{XRD} leads to the decrease in $\Delta z_i(t)$. The competition between the increase in $q_i(t)$ and the decrease in $\Delta z_i(t)$ leads to the inceptive recovery of I^s_{SHG} and the overall slight increase in P_s. From 2.6 ps to 7 ps, the partial restoration of the atomic displacement, revealed by the partial recovery of I_{XRD} near the peak, and the ongoing electron relaxation result in the increase of both $\Delta z_i(t)$ and $q_i(t)$, respectively. This increase is associated with the continuous increase of I^s_{SHG} and P_s. From a few hundred femtoseconds up to 7 ps, the optical reflectance is mainly contributed by the carrier population on the conduction band which is inversely proportional to $q_i(t)$, while the SHG intensity is driven by the interplay of the increase in $q_i(t)$ and the non-monotonic changes in atomic displacements $\Delta z_i(t)$. The latter have in general slower dynamics compared to charges. This may explain why the optical reflectance with $\tau_1 = 5.5\,\mathrm{ps}$ recovers faster than the SHG intensity with $\tau_1 = 7.3\,\mathrm{ps}$ (Figure 6.11c). Between 7 ps and 20 ps, the persistent out-of-plane lattice expansion further displaces the atoms from each other within the unit cell, leading to an average increase of $\Delta z_i(t)$. Simultaneously, the electrons are in the transition between the faster non-radiative intraband relaxation and the slower radiative interband relaxation, resulting in the reduction of the $q_i(t)$ increasing rate. After 20 ps, the lattice expansion saturates and the atomic displacement $\Delta z_i(t)$ stays constant. The electronic relaxation after 20 ps is assigned to the radiative recombination (Figure 6.11d). The significant difference in the slow recovery time τ_2 (30 ps for $\Delta R/R$ and 220 ps for $\Delta I^s_{\mathrm{SHG}}/I^s_{\mathrm{SHG}}$) may be due to the expected longer relaxation time of the atomic displacements $\Delta z_i(t)$. In fact, Figure 6.1c shows that the initial atomic displacements may not recover within a few picoseconds, in particular at larger incident fluences. While the transient changes in $\Delta R/R$ mainly come from the photoexcited carriers, the transient changes in $\Delta I^s_{\mathrm{SHG}}/I^s_{\mathrm{SHG}}$ originate from both the varying ionic charges and the atomic displacements.

We now focus on the transient change in the symmetry of our material upon optical excitation. Figures 6.11e-f show the SHG polar patterns I^p_{SHG} and I^s_{SHG} at $t < 0$ ps and $t = 250$ fs. The polar patterns obtained before the arrival of the pump confirm the symmetry point group of $4mm$, indicated by the good fit of the experimental polar patterns with Equations (2.25) and (2.26) (Section 2.4). The minor discrepancies between the data and the fit model might be attributed to the coherent strain of our BTO thin film to the substrate (Section 4.5), which results in the emergence of additional minor nonzero tensor elements [154]. The change of the symmetry of the unit cell upon photoexcitation can be revealed through the deformation of the polar SHG patterns at different time delays. At first glance, there is no evident change in the symmetry shortly after pump excitation. The patterns can always be fitted by applying a same scaling factor to all susceptibility tensor elements χ_{ijk}. However, a closer examination reveals a laser-induced change in symmetry. To visualize this, I^p_{SHG} and I^s_{SHG} polar plots were measured at time delays from -1 ps to 3 ps in 80 fs steps. Fitting each pair of polar plots using Equations (2.25) and (2.26) yielded the tensor elements χ_{zxx}, χ_{xxz}, and χ_{zzz} as a function of time. The transient change in χ_{ijk} is calculated as $\Delta\chi/\chi = [\chi(t) - \chi_0]/\chi_0$, where $\chi(t)$ and χ_0 are χ_{ijk} at $t > 0$ and $t \leq 0$, respectively (Figure 6.12). As shown in Figure 6.12a, $\chi_{zxx}(t)$ exhibits dynamics similar to $I^s_{\mathrm{SHG}}(t)$ (Figure 6.12a), as expected. In contrast, $\chi_{zxx}(t)$ and $\chi_{zzz}(t)$ experience a 0.5 % larger drop compared to $\chi_{xxz}(t)$ (Figure 6.12b). The different dynamics of the various χ_{ijk} components suggest a time-dependent, non-thermal transient change in symmetry of our sample for the following reasons. First, according to the theoretical calculation by Murgan and colleagues [155], a purely thermal effect leads to a uniform variation of all tensor elements χ_{ijk}, which is not observed in our case. Second, tensor elements χ_{zxx} and χ_{zzz} represent the amplitude of electric dipole oscillation along z axis induced by the incident light field, while χ_{xxz} represents that along x axis (in-plane direction) induced by the incident light field (Section 2.4). According to RT-TDDFT calculations in BTO [26, 148], the Ti-O bonds parallel to the spontaneous polarization (z axis) are significantly weaker than those perpendicular to the spontaneous polarization. In other words, the probability of ionic movement along the z axis is much higher than that in the xy plane. Consequently, one would expect a larger change in the electric dipole amplitude along the z axis compared to the x axis upon above-bandgap excitation. The larger changes in χ_{zxx} and χ_{zzz} compared to χ_{xxz}, demonstrate experimentally the predicted high directionality of ligh-induced

polarization changes [26].

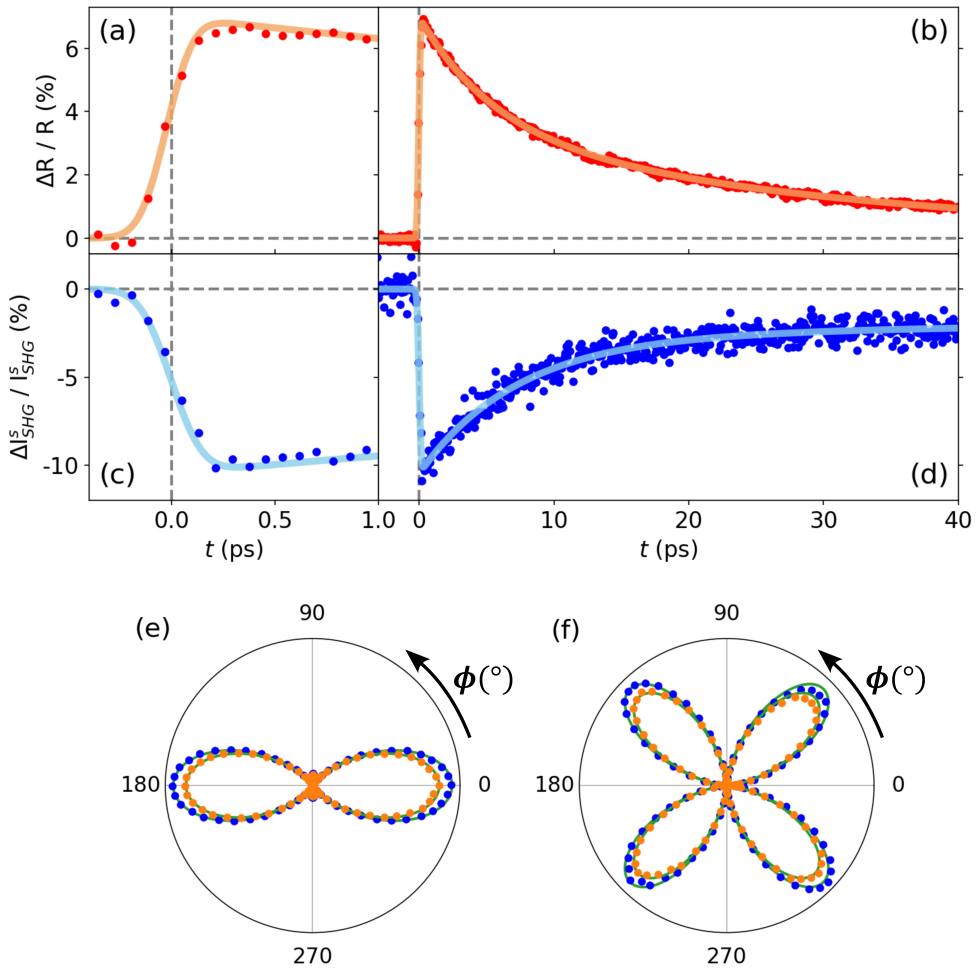

Figure 6.11.: Time evolution of $\Delta R/R$ and $\Delta I^s_{\mathrm{SHG}}/I^s_{\mathrm{SHG}}$, and polar plots at fixed delays. (a) and (b) show the time evolution of $\Delta R/R$ in the short and long timescale, respectively. (c) and (d) show the time evolution of $\Delta I^s_{\mathrm{SHG}}/I^s_{\mathrm{SHG}}$ in the short and long timescale, respectively. The time traces of both $\Delta R/R$ and $\Delta I^s_{\mathrm{SHG}}/I^s_{\mathrm{SHG}}$ are fitted by the same function characterized by one rise time τ_0, and two recovery times τ_1 and τ_2. (e) The polar SHG pattern in P-out configuration measured at $t < 0$ ps (blue) and $t = 0.25$ ps (orange). (f) The polar SHG pattern in S-out configuration measured at $t < 0$ ps (blue) and $t = 0.25$ ps (orange). The fit of both patterns are performed using Equation (2.25) and (2.26) assuming the symmetry point group of $4mm$.

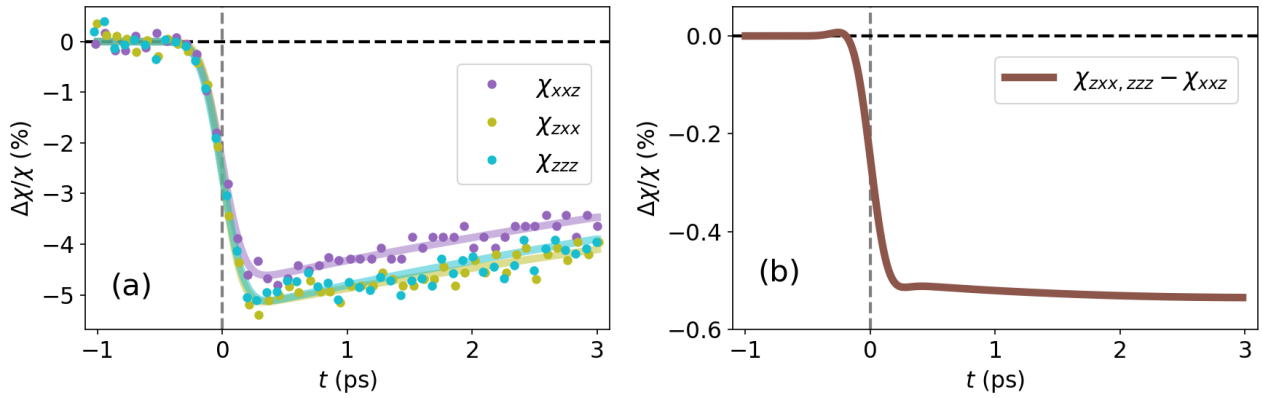

Figure 6.12.: Transient changes of the BTO tensor elements. (a): The transient changes of χ_{xxz} (purple), χ_{zxx} (olive), and χ_{zzz} (cyan) as a function of the pump-probe delay. (b): The average transient change of the difference $(\chi_{zxx} + \chi_{zzz})/2 - \chi_{xxz}$.

All the dynamics of SHG and optical reflectance described above is upon an incident pump fluence of 2.7 mJ cm^{-2}. A fluence dependence of the maximum increase in $\Delta R/R$ and maximum drop in $\Delta I^s_{\mathrm{SHG}}/I^s_{\mathrm{SHG}}$ displays a linear regime up to the fluence around 12.5 mJ cm^{-2} (Figure 6.13a). Beyond this fluence, we observe the indication of sample damage which is indicated by the ratio of the polar patterns measured after and before the delay measurement, that is smaller than 0.9, described in Section A.14 (Figure A.6). Figure 6.13b shows the ratio of the polar patterns following and preceding each delay scan, from which data in Figure 6.13a, c and d are extracted. The fact that this ratio is 0.97 ± 0.05 indicates a nearly perfect overlapping of two polar patterns before and after a pumping cycle and is representative of an undamaged sample. The rise time τ_0 remains nearly the same between 100 fs and 200 fs for all the incident fluences reported here (Figure 6.13c). The fluctuation of τ_0 by around $\pm$ 50 fs is comparable to the time resolution of $\approx$86 fs (Section 3.2). The ultrashort rise time at all fluences further confirms the fast nature of the carrier avalanche induced by above-bandgap optical pump.

Regarding the fast relaxation time τ_1 of $\Delta R/R$, it maintains the same level at around 9 ps from 1.4 to 4 mJ cm^{-2} before experiencing a decrease to about 4 ps at the incident fluence of 12.5 mJ cm^{-2} (Figure 6.13d). Young and his colleagues observed the similar effect on GaAs exposed to the 400 nm above-bandgap optical excitation [156]. In this study, the decrease in nonradiative relaxation time with increasing photoexcited density was evidenced. They assigned the increase in this non-radiative recombination rate, i.e., a shorter recovery time, to the increase of electron-hole plasma concentration upon the increasing excitation fluence. Another study on the light-induced dynamics of excitonic insulator Ta_2NiSe_5 reveals the relationship between the fast relaxation time and the electronic bandgap [157]. In this study, the decrease in the fast relaxation time is assigned to the partial closing of the bandgap, resulted from the electron-phonon scattering. Therefore, the change of τ_1, in our case, can be assigned to the bandgap deformation due to the electronic pressure generated by the accumulation of carriers near the gap edge [51]. The decrease in τ_1 is consistent with the decrease in E_g upon increasing the incident fluence and further validates the negative sign of the coefficient $\frac{\partial E_g}{\partial p}$ obtained from the fit of the average strain $\overline{\eta}(t)$ (Section A.13).

We turn now to the fast relaxation time τ_1 of $\Delta I^s_{\mathrm{SHG}}/I^s_{\mathrm{SHG}}$. We observe that τ_1 experiences an overall increase from 8 ps to 14 ps corresponding to the

incident fluence between 1.4 and 4 mJ cm^{-2} (Figure 6.13d). Subsequently, there is a saturation of τ_1 from 4 to 12.5 mJ cm^{-2}. While the relaxation dynamics of optical reflectance only involves the relaxation of ionic charge $q_i(t)$, the dynamics of SHG is the competition among the recoveries of $q_i(t)$ and $\Delta z_i(t)$ (Equation (6.1.3)). Thus, we should not expect the same behaviour of τ_1 in both data sets. An additional observation is that the sudden changes in τ_1 of $\Delta R/R$ and $\Delta I^s_{\mathrm{SHG}}/I^s_{\mathrm{SHG}}$ occur at the same pump fluence of 4 mJ cm^{-2}. According to the relative change in the BTO peak diffraction intensity ΔI_{XRD}, it takes longer to recover to the ground state at higher fluences (Figure 6.1c). This indicates that $\Delta z_i(t)$ has a longer recovery time at higher fluences. Meanwhile, we observe that the recovery time of $q_i(t)$, represented by the recovery time of $\Delta R/R$, remains unchanged for incident fluences from 1.4 to 4 mJ cm^{-2} (Figure 6.13d). Consequently, the increase in the recovery time of $\Delta z_i(t)$ and the unchanged recovery time of $q_i(t)$ result in the monotonic increase of τ_1 for $\Delta I^s_{\mathrm{SHG}}/I^s_{\mathrm{SHG}}$ at incident fluences from 1.4 to 4 mJ cm^{-2}. At fluences greater than 4 mJ cm^{-2}, the decrease in τ_1 of $\Delta R/R$ implies a reduction in the recovery time of $q_i(t)$, while the recovery time of $\Delta z_i(t)$ continues to increase. This interplay between $q_i(t)$ and $\Delta z_i(t)$ could result in the approximately constant τ_1 for $\Delta I^s_{\mathrm{SHG}}/I^s_{\mathrm{SHG}}$ at the incident fluences larger than 4 mJ cm^{-2}.

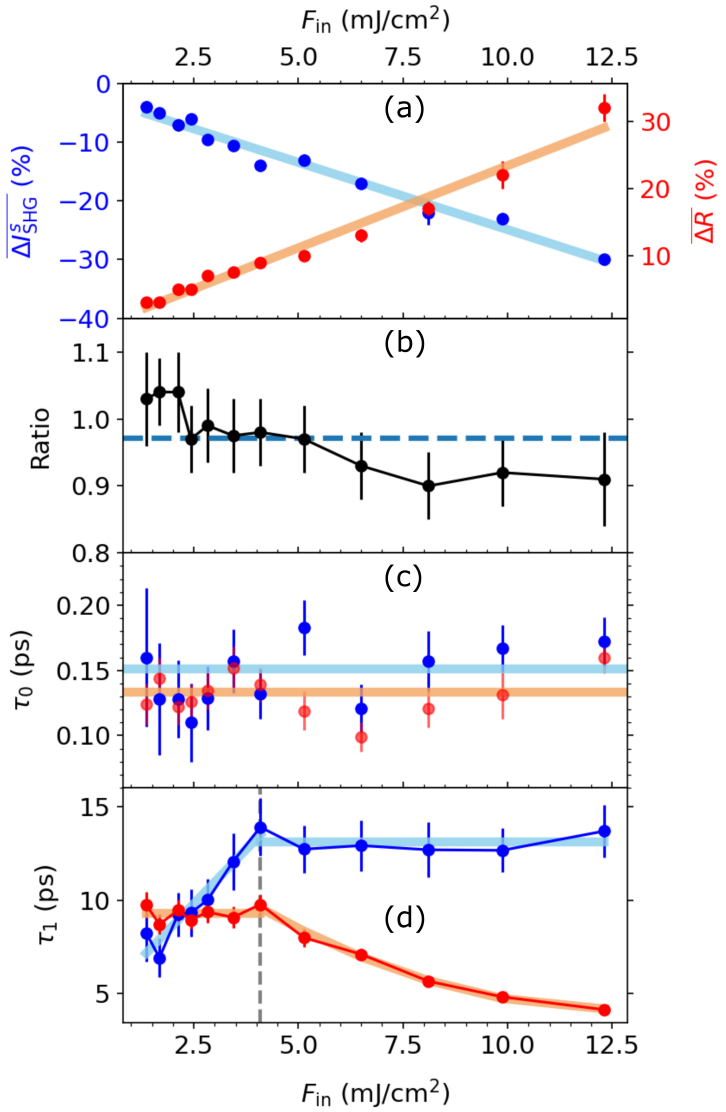

Figure 6.13.: Fluence dependence of $\overline{\Delta R}$, $\overline{\Delta I^s_{SHG}}$ and the time constants τ_0 and τ_1. (a): Fluence dependence of the maximum increase of $\Delta R/R$ (red) and the maximum decrease of $\Delta I^s_{SHG}/I^s_{SHG}$ (blue) and their corresponding linear fits (light red for $\Delta R/R$ and light blue for $\Delta I^s_{SHG}/I^s_{SHG}$). (b): The ratio of the polar patterns measured after and before the delay scan measurement (black). The blue dashed line indicates the average of all data points 0.97 ± 0.05. (c): Fluence dependence of the rise time τ_0 of $\Delta R/R$ (red) and $\Delta I^s_{SHG}/I^s_{SHG}$ (blue). The red and blue solid lines indicate the average values of the rise times of $\Delta R/R$ and $\Delta I^s_{SHG}/I^s_{SHG}$, respectively. (d): Fluence dependence of the fast recovery time τ_1 of $\Delta R/R$ (red) and $\Delta I^s_{SHG}/I^s_{SHG}$ (blue) and their corresponding fits (light red for $\Delta R/R$ and light blue for $\Delta I^s_{SHG}/I^s_{SHG}$). The vertical dashed line indicates the fluence at which the trend of τ_1 shows a discontinuity.

6.2. Discussion

The combination of time-resolved XRD, SHG, and optical reflectance reveals the dynamics of lattice structure and ferroelectric polarization under above-bandgap optical excitation. The dynamics can be divided into four stages, along with the equilibrium stage before the arrival of the pump $t \leq 0$ ps (Figure 6.14a). In the first few hundred femtoseconds, the charge transfer from the occupied O 2p to the unoccupied Ti 3d orbitals leads to: (i) a reduction in ionic charge $q_i(t)$ (Equation (6.1.3)), which causes a reduction in ferroelectric polarization, resulting in the reduction of the SHG intensity, and (ii) an increase in photoexcited carrier density, which increases the optical reflectance (Figure 6.14b). Up to 3 ps from the arrival of the pump, a decrease of ≈ 8 pm in the relative displacement between Ti atom and the center of the O octahedron is revealed by the drop in the diffraction intensity I_{XRD} near the peak (Figure 6.14c). In addition, the pump energy, that is initially transferred to the electrons, is exchanged to the lattice via electron-phonon coupling during the intraband relaxation of photoexcited electrons from the top to the bottom of the conduction band. This energy heats the lattice, resulting in a deformation of the c parameter. This deformation is influenced by the out-of-plane linear thermal expansion coefficient, which is dependent on the lattice temperature, and the deformation potential of the electronic structure near the Fermi level, which depends on the electron temperature (Section 6.1.2). At time delays $3\,\text{ps} < t < 7\,\text{ps}$, the relative displacement of atoms within the unit cell recovers to its initial state, as the diffraction intensity I_{XRD} near the peak partially recovers (Figure 6.14d). At time delays $t > 7$ ps, we observe the partial recovery of SHG intensity and optical reflectance as the result of the non-radiative recombination of photoexcited carriers associated with the intraband relaxation up to $t = 20$ ps (Figure 6.14e). More importantly, while the SHG intensity does not return to the ground state after a few tens of picoseconds, as indicated by the second relaxation time $\tau_2 = 220$ ps, the out-of-plane strain initially decreases over the first few picoseconds and then increases beyond its ground state, eventually stabilizing around 20 ps. This demonstrates that the dynamics of SHG intensity, i.e., ferroelectric polarization, is not solely driven by the lattice, but also by the electron dynamics.

In this study, we demonstrate that the observed lattice deformation can be accurately described by the combination of ultrafast heating of the lattice and deformation potential, both induced by the above-bandgap optical excitation.

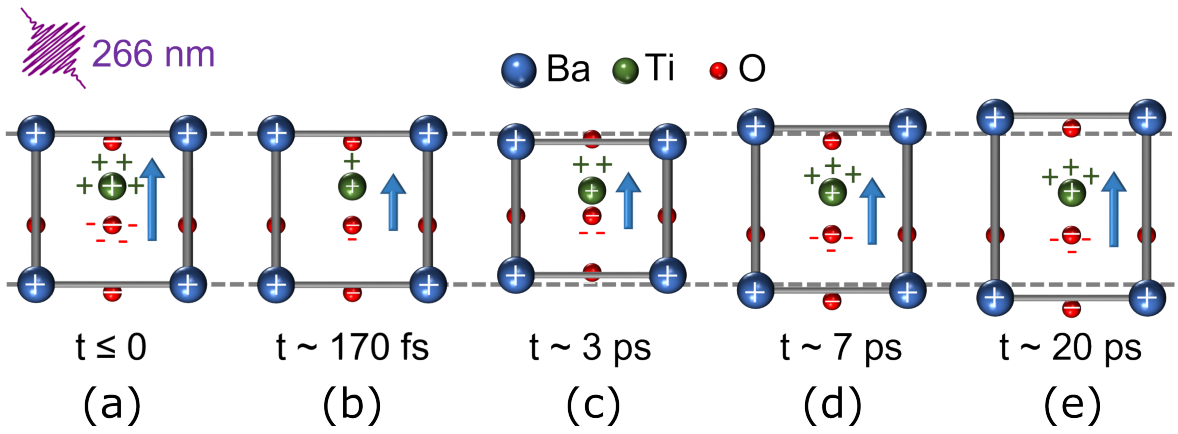

Figure 6.14.: Summary sketch of the BTO c parameter and charge distribution resulting from time-resolved XRD, SHG and optical reflectance data. This process includes an equilibrium stage and four stages of non-equilibrium dynamics. (a): At $t \leq 0$, the system is at equilibrium before the arrival of the pump. (b): At $t \approx 170$ fs, charge transfer occurs, resulting in a decrease of the net charges at Ti and O sites, thus a decrease in polarization. (c): At $t \approx 3$ ps, there is partial recovery of the electronic distribution and compression of the c parameter, due to the dominance of the DP contribution over the TE contribution. (d): At $t \approx 7$ ps, further but incomplete recovery of the electronic distribution is observed, along with expansion of the c parameter, because the TE contribution becomes dominant over the DP contribution. (e): At $t \approx 20$ ps, the electronic distribution is not yet completely relaxed to the ground state, and lattice expansion saturates. The light blue arrow denotes the orientation of the spontaneous polarization. The green plus and red minus signs represent the ionic charges of Ti and O atoms, respectively. For clarity, charges are shown only around one O atom. The gray dashed lines indicate the bottom and top (001) lattice planes of the unit cell at equilibrium.

However, there are other mechanisms that may drive the lattice deformation [27–29]. Among these mechanisms, the bulk photovoltaic effect is well-known to be the main driving forces for the photoinduced lattice deformation in a ferroelectric system. The bulk photovoltaic effect is defined as a high voltage, significantly larger than the band gap energy, which is generated when a material with broken inversion symmetry is illuminated [158]. This photovoltage results in the mechanical strain within the material due to the inverse piezoelectric effect [5, 51]. We now discuss the negligible contribution of the bulk photovoltaic effect to the observed lattice deformation in our BTO thin film, under our experimental conditions.

First, the bulk photovoltaic effect within the BTO thin film is negligibly small at the pump energy (4.66 eV) employed in this experiment. According to the first principle calculation of the shift current in ferroelectrics, the current density response from transverse light field with the wavelength of 266 nm is minimal in BTO [159]. In the same material, the shift current amplitude induced by a transverse 266 nm pump is of the order of 10^{-13} A in both experiment and calculation [159, 160]. In addition, a similar calculation is employed to determine the ballistic current, which is another dominant mechanism for the bulk photovoltaic effect in BTO [161]. The ballistic current response to the either transverse or longitudinal light field with the wavelength of 266 nm is minimal at around 10^{-6} A/V^2 for the tetragonal BTO.

Moreover, the bulk photovoltaic effects can be revealed through the light polarization dependence of the photovoltaic signal. In the study conducted by Ref. [158], the bulk photovoltaic currents were both experimentally measured and theoretically calculated as a function of incident light polarization, demonstrating the dependence of these currents on the light polarization. However, this phenomenon is not observed in our study. In our particular setup, the incident polarization of the pump pulse is nearly perpendicular to the out-of-plane polarization. We measure the maximum drop in the SHG intensity as a function of incident polarization (Figure 6.15a). As a result, the SHG drop, i.e., the decrease in ferroelectric polarization, remains unchanged regardless of the rotation of the linear pump polarization (Figure 6.15b). This observation contradicts the theoretical calculations by Ref. [158], which revealed a dependence of bulk photovoltaic currents on the polarization of the incident light.

Now, we are going to compare our results with other studies relevant to our research. The dynamics of lattice structure and ferroelectric polarization under optical excitation have been studied extensively. Time-resolved XRD experiments, as documented in several works [151, 162–169], have particularly revealed lattice deformation resulting from the propagation of acoustic waves. The materials investigated are primarily ferroelectrics, multiferroics and semiconductors, including $PbTiO_3$, $SrTiO_3$, $BiFeO_3$, $SrRuO_3$, $PbZr_xTi_{1-x}O_3$, and GaAs. In particular, Daranciang and his colleagues [162] employed femtosecond time-resolved XRD to investigate the interaction between light and $PbTiO_3$ ferroelectric thin films, grown on $DyScO_3$ and $SrTiO_3$ substrates, which are very similar to our thin film. They assigned the large-amplitude structural changes in $PbTiO_3$ thin films to the direct coupling of light to the bulk photovoltaic response of the ferroelectrics. The key difference between our study and

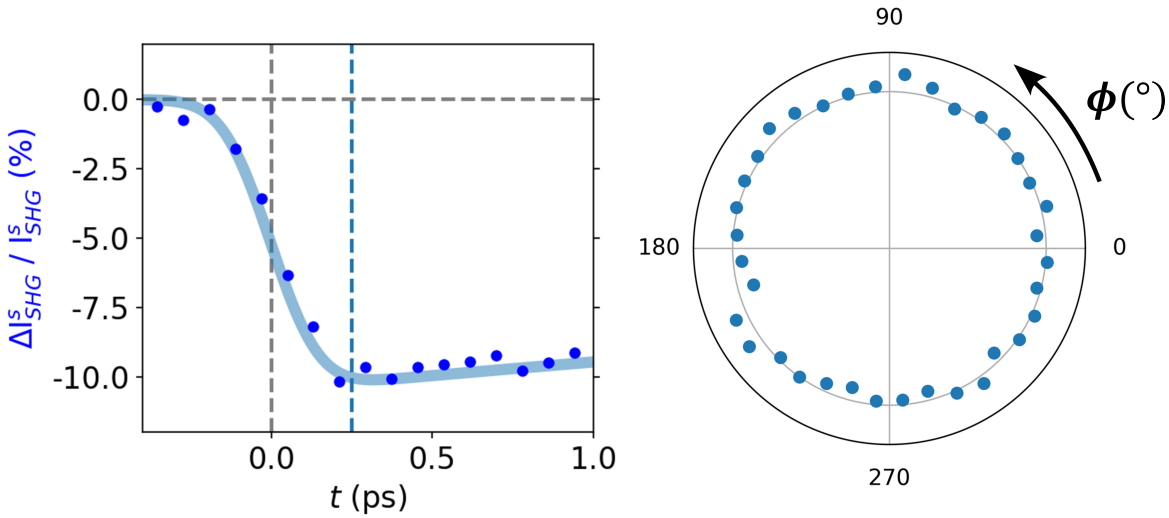

Figure 6.15.: Dependence of the SHG intensity drop on the pump polarization. (a): Time evolution of the differential SHG intensity $\Delta I^s_{\mathrm{SHG}} / I^s_{\mathrm{SHG}}$ measured at $\phi = 45°$ in a short timescale. Gray horizontal and vertical dashed lines indicate 0 in the corresponding axes. Blue dashed line indicates the time delay where the differential SHG intensity is measured as a function of the incident polarization. (b): Dependence of the maximum decrease in $\Delta I^s_{\mathrm{SHG}} / I^s_{\mathrm{SHG}}$ measured at $t = 0.25\,\mathrm{ps}$ on the polarization of 266 nm optical pulses.

theirs is the pump photon energy. While our incident photon energy (4.66 eV) is far larger than the bandgap of the target material (3.4 eV), their excitation energy (3.1 eV) was quite close to but below the bandgap of $PbTiO_3$ (3.6 eV) [170]. As a result, the our photoexcited carrier density ($\approx 1 \times 10^{27}\,\mathrm{m}^{-3}$) (Figure 6.4) is an order of magnitude larger than their calculated carrier density ($\approx 1 \times 10^{26}\,\mathrm{m}^{-3}$). In addition, their calculated temperature increase in $PbTiO_3$ thin film was about 50 K which was around one fourth of our lattice temperature jump (192 K) at the fluence of $1.4\,\mathrm{mJ\,cm}^{-2}$ (Section 6.1.2). Lastly, their XRD performed with 266nm optical excitation resulted in the similar maximum structural change as with 400 nm optical excitation, but at a very low fluence around $10\,\mu\mathrm{J\,cm}^{-2}$, which was more than two orders of magnitude lower than our fluences.

Another recent study conducted by Sarott and his coworkers [30] used the continuous-wave UV light to transiently enhance or suppress the ferroelectric polarization, depending on the initial polarization direction, of epitaxial

$PbZr_xTi_{1-x}O_3$ thin film. This phenomenon was linked to the separation of photoexcited charge carriers at the Schottky interface between the ferroelectric film and the bottom electrode. As mentioned previously, they also excluded the dominant contribution of the bulk photovoltaic effect based on the independence of the light-induced polarization change of the thin film on the incident polarization direction of the continuous-wave UV laser [30]. In this study, the peak power was a few tens of $\mathrm{mW\,cm^{-2}}$ and the transient SHG variation was independent of the UV-laser power. In our case, we used the pulsed laser with extremely higher peak power around $20\,\mathrm{GW\,cm^{-2}}$, at the lower fluence of $1.4\,\mathrm{mJ\,cm^{-2}}$, and observed a linear fluence dependence of the SHG decrease (Figure 6.13). This striking difference in the dependence of the ferroelectric polarization on different types of the pump pulses shows that, in our experimental conditions, ultrafast heating cannot be ignored and has a significant contribution to the observed structural changes.

In previous studies, polarization dynamics were often inferred directly from lattice dynamics without a direct measurement [151, 162, 169]. On the other hand, other studies directly measured the dynamics of ferroelectric polarization [30, 171], without probing the structural dynamics of the same sample [171]. In our study, by performing the time-resolved XRD, SHG, and optical refectance, we measure both lattice deformations and polarization, closely examining their relationship out of equilibrium. Additionally, the time-resolved SHG polarimetry reveals transient changes not only in the spontaneous polarization but also in the symmetry of the material.

7. Summary and conclusion

In this thesis, we have achieved significant progress in understanding the structural and polarization properties of ferroelectric thin films and in employing a range of spectroscopic techniques to elucidate these properties in both static and optically excited regimes.

First, the XSW technique has been effectively applied to BTO thin films to determine the displacement profile of Ti atoms near the surface, relative to the Ba atomic positions that define the center of the unit cell. Previous research has utilized the XSW technique in combination with XPS to ascertain the polarization orientation of the entire film ($P^{\uparrow}$ or $P^{\downarrow}$) [43, 44, 46, 91, 172–175]. In our work, we measured the photoelectron yield to independently determine the near-surface displacement of Ti atoms. Initially, modeling of XRD data revealed the distribution of out-of-plane lattice parameters due to epitaxial strain in our thin films. The structural sensitivity of the XSW technique, along with the chemical specificity, surface sensitivity, and depth selectivity of XPS, allowed us to determine the positions of Ti and Ba atoms at various depths along the out-of-plane direction with picometer spatial resolution. Since the Ba position defines the unit cell center, measuring the Ti position provides direct access to the local ferroelectric polarization. To understand the ferroelectric polarization profiles at the surface of our BTO samples, we analyzed the distribution of O adsorbates using depth-dependent O 1s XPS spectra.

A detailed examination of oxygen species adsorbed on the surface suggested possible charge compensation mechanisms consistent with the ferroelectric polarization distributions derived from XSW data. We identified three distinct scenarios: (i) a polarization reversal from downward $P^{\downarrow}$ to upward $P^{\uparrow}$, resulting in a tail-to-tail polarization configuration near the third unit cell, possibly stabilized by H^{+} atoms diffused below the surface (Figure 5.7b); (ii) a minor polarization reversal from upward $P^{\uparrow}$ to downward $P^{\downarrow}$ above the third unit cell, leading to vanishing polarization due to the competing presence of $O_L H^{-}$ favoring downward polarization $P^{\downarrow}$ and OH^{-} or O_2^{-} favoring upward polarization $P^{\uparrow}$ (Figure 5.7c); (iii) a uniform upward polarization $P^{\uparrow}$ through-

out the BTO film up to the surface, accompanied by a high concentration of compensating negatively charged chemisorbed oxygen species (Figure 5.7d).

The diversity of observed ferroelectric configurations highlights the complexity of these systems and underscores the importance of studying them from multiple perspectives to better understand the mechanisms shaping the ferroelectric polarization profile at the surface. This work is novel in combining structural and spectroscopic information provided by the XSW technique to offer a comprehensive picture of the surface ferroelectric polarization profile. Such studies can be extended to other interesting oxides and technologically relevant materials, including multiferroics [175]. Furthermore, in the context of catalytic reactions at ferroelectric surfaces, understanding and controlling the surface polarization and its interaction with adsorbates is crucial. In operando XSW investigations can guide material engineering toward more efficient catalysts [21, 22]. Notably, the few-picometer structural accuracy of the XSW technique offers a rigorous benchmark for testing theoretical models, thereby enhancing their predictive power [9, 10].

Second, we combine time-resolved XRD, SHG, and optical reflectance to investigate the light-induced dynamics of lattice structure and ferroelectric polarization in BTO ferroelectric thin films. Previous studies have employed femtosecond time-resolved XRD and optical reflectance to examine the transient structural transformation upon optical excitation [51, 150–152, 156, 162–169] and deduced the dynamics of the spontaneous polarization without a direct measurement. Conversely, there have been works that directly measured the dynamics of the ferroelectric polarization [30, 171], but failed to interpret it due to the lack of data on the structural dynamics [171]. In our research, we investigate both lattice deformations and polarization, thoroughly analyzing their interrelation. By applying the two-temperature model and the one-dimensional strain wave equation to fit the average strain $\overline{\eta}(t)$, we gain a detailed understanding of the contributions from electronic and lattice subsystems to the lattice deformation. In the initial few hundred femtoseconds after the absorption of above-bandgap optical pulses, charge transfer from the occupied O 2p to the unoccupied Ti 3d orbitals leads to two main effects: (i) a reduction in ionic charge $q_i(t)$, resulting in a decreased amplitude of the ferroelectric polarization, and (ii) an increase in photoexcited carrier density. The instantaneous change in electronic distribution drives the atomic movements of Ti and O towards higher symmetry positions, reducing the distance between the Ti atom and the center of the O octahedron. Additionally,

the pump energy initially transferred to electrons is subsequently transferred to the lattice through electron-phonon coupling, during the intraband relaxation of photoexcited electrons from the top to the bottom of the conduction band. This causes the lattice to heat up, leading to a deformation in the c parameter. After the first few hundred femtoseconds, a partial recovery of the ferroelectric polarization is observed due to the non-radiative recombination of photoexcited carriers associated with intraband relaxation. However, while the ferroelectric polarization does not fully return to the ground state within a few tens of picoseconds, the out-of-plane strain first decreases in a few picoseconds and then continues increasing past its ground state until it saturates after around 20 ps. This observation confirms that the dynamics of the ferroelectric polarization is not simply proportional to the lattice dynamics; instead, it is influenced by both lattice and electronic dynamics. Furthermore, the observed changes in the nonlinear optical susceptibility tensor elements upon optical excitation indicate a non-thermal transient change of the sample symmetry, which is linked to a highly directional instability in light-induced polarization.

The variation in lattice and polarization dynamics with different incident fluences highlights the importance of simultaneously measuring these parameters to better understand the physical mechanisms driving the transformation of electronic distribution near the Fermi level, which results in the lattice deformation and spontaneous polarization modification. While light-induced lattice deformation is generally attributed to the bulk photovoltaic effect and inverse piezoelectricity, it is crucial to also account for thermal effects at relatively high pump fluences and above-bandgap excitation. Our findings demonstrate that tuning the incident fluence allows for control over changes in ferroelectric polarization, mechanical strain, and strain distribution within the ferroelectric thin film, as well as electronic and polarization recovery times. As noted in the introduction, this is particularly significant for remote and wireless optomechanical and optoelectronic applications based on ferroelectrics [27–29].

We anticipate that the combination of multiple pump-probe techniques (XSW, XPS, SHG, and optical reflectance) at X-ray free-electron laser facilities will be crucial to investigate the dynamics of the ferroelectric polarization and track simultaneously atomic displacements and electronic changes in real-time.

A. Appendix

A.1. Solution of Takagi-Taupin equation

In this section, we present the solution of Takagi-Taupin Equation (2.4) given in Section 2.2. The X-ray diffracted intensity from the sublayer L_i with thickness t_i at photon energy E_v and $z_i < z < z_i + t_i$ is calculated as [100]:

$$R(E_v, z) = \beta |Y|^2 |r(E_v, z)|^2 = \beta |Y|^2 \left| \frac{x_1 - x_2 x_3 \exp(-\sigma \Delta z_i)}{1 - x_3 \exp(-\sigma \Delta z_i)} \right|^2, \tag{A.1}$$

where $x_1 = -\left(b + \sqrt{b^2 - C_1^2}\right)/C_1$, $x_2 = -\left(b - \sqrt{b^2 - C_1^2}\right)/C_1$, and $x_3 = (x_1 - r_{t_i}) \exp(\sigma t_i)/(x_2 - r_{t_i})$, $\sigma = 2\mathrm{i}\sqrt{b^2 - C_1^2}/L_{ex}$, and $\Delta z_i = z - z_i$. The geometry factor β is defined as $\beta = \Gamma_{\mathbf{0}}/|\Gamma_{\boldsymbol{h}}|$, where $\Gamma_{\mathbf{0}} = k_{\mathbf{0}z}/K$ and $\Gamma_{\boldsymbol{h}} = k_{\boldsymbol{h}z}/K$ are the direction parameters with $K = 2\pi/\lambda_B$ and λ_B is the Bragg wavelength.

The parameter C_1 is expressed as $C_1 = C(1 - \mathrm{i}p)\exp(-W(z))$, where $p = -X_{\mathrm{i}}/X_{\mathrm{r}}$ and C is the polarization factor, which equals 1 for σ polarization and $\cos 2\theta_B$ for π polarization, with θ_B being the Bragg angle. The parameters $Y = \sqrt{\chi_{\boldsymbol{h}}/\chi_{\bar{\boldsymbol{h}}}} = |Y| \exp(\mathrm{i}\Phi_Y)$, $X_{\mathrm{r}} = Re\left[\sqrt{\chi_{\boldsymbol{h}}\chi_{\bar{\boldsymbol{h}}}}\right]$, and $X_{\mathrm{i}} = Im\left[\sqrt{\chi_{\boldsymbol{h}}\chi_{\bar{\boldsymbol{h}}}}\right]$ are derived from the crystal susceptibilities χ_0, $\chi_{\boldsymbol{h}}$, $\chi_{\bar{\boldsymbol{h}}}$ corresponding to the vectors $\mathbf{0} * \boldsymbol{h}$, $\boldsymbol{h}$, and $-\boldsymbol{h}$ with $\boldsymbol{h} = 2\pi \boldsymbol{H}$. The crystal susceptibility $\chi_{\boldsymbol{h}}$ is in general a complex number, given by $\chi_{\boldsymbol{h}} = \chi_{\boldsymbol{h}\mathrm{r}} + \mathrm{i}\chi_{\boldsymbol{h}\mathrm{i}}$, where $\chi_{\boldsymbol{h}\mathrm{r}} = -\left(\mathrm{e}^2\lambda_B^2/mc^2\pi\Omega\right)F_{\boldsymbol{h}\mathrm{r}}$ represents X-ray elastic scattering, and $\chi_{\boldsymbol{h}\mathrm{i}} = \left(\mathrm{e}^2\lambda_B^2/mc^2\pi\Omega\right)F_{\boldsymbol{h}\mathrm{i}}$ accounts for X-ray absorption. The structure factor $F_{\mathrm{h}} = \sum_j f_j \exp(-W_j)\exp(-\mathrm{i}\boldsymbol{h}\boldsymbol{\rho}_j)$ is computed from the atomic scattering factor f_j of the jth atom at position vector $\boldsymbol{\rho}_j$ in the unit cell. The atomic scattering factor $f_j = f_0(\theta_B, \lambda_B, Z) - Z + f_1(0, \lambda_B, Z) + \mathrm{i}f_2(0, \lambda_B, Z)$ describes the interaction between X-rays and atoms, where Z is the atomic number, and f_0, f_1, and f_2 are tabulated in [176, 177]. In addition to the reflection amplitude, solving the Takagi-Taupin equations also

provides the transmission amplitude through the sublayer L_i [100]:

$$T(E_\nu, z) = \exp[i\Phi(E_\nu)\Delta z_i/2]\left(\frac{1 - x_3\exp(-\sigma\Delta z_i)}{1 - x_3}\right), \tag{A.2}$$

where $\Phi(E_\nu) = (2\pi\chi_\mathbf{0})/(\lambda_B\Gamma_\mathbf{0}) - 2C_1x_1/L_{ex}$.

A.2. Deformation phase calculation

The deformation phase φ_0 in Equation (2.3), originates from the bicrystal model [100] and is expressed as $\varphi_0 = 2\pi(c_0 - \bar{c})t_0/\bar{c}^2$. The bicrystal model presumes a crystal, where the XSW is generated, along with a deformed overlayer of thickness t_l that causes a shift in the diffraction planes, given by $\varphi_0 = 2\pi(c_l - c_c)t_l/c_c^2$, with c_l and c_c representing the out-of-plane lattice parameters of the deformed layer and the crystal, respectively. In our samples, the XSW is generated within the BTO film itself, experiencing deformation due to inhomogeneous strain. Consequently, the deformation phase cannot be associated with the c parameter of an underlying single crystal. Alternatively, φ_0 corresponds to the average out-of-plane lattice parameter $\bar{c}$, which is determined from the experimental diffraction curves (Section 5.1.1). This approach is akin to modeling the thin film as a crystal with an average out-of-plane parameter $\bar{c}$ and a deformation phase that increases towards the interface with SRO and decreases towards the surface. This choice is validated by the coherent position of the Ba atoms (Table 5.3), which is close to 1, indicating proximity to the diffraction planes. In contrast, if the deformation phase were instead referenced to the bottom sublayer L_{n-1}, it would result in the Ba atoms in the top unit cells being positioned unphysically 1 Å away from the diffraction planes.

A.3. Calculation of the inelastic mean free path

The mathematical expression of the inelastic mean free path $\lambda_l(E_\nu)$, according to Ref. [178], is:

$$\lambda_l(E_\nu) = \frac{\mathcal{A}(E)(E_\nu - \mathrm{BE})}{E_p^2\left\{\mathcal{B}\left[ln(\mathcal{Y}\mathcal{A}(E_\nu)(E_\nu - \mathrm{BE}))\right] - \mathcal{C}/(E_\nu - \mathrm{BE}) + \mathcal{D}/(E_\nu - \mathrm{BE})^2\right\}}. \tag{A.3}$$

In Equation (A.3): $\mathcal{A}(E_\nu) = \left[1 + (E_\nu - \mathrm{BE})/(2m_e c^2)\right] / \left[1 + (E_\nu - \mathrm{BE})/(m_e c^2)\right]^2$, $\mathcal{B} = -1.0 + 9.44/(E_p^2 + E_g^2)^{0.5} + 0.69\rho^{0.1}$, $\mathcal{C} = 19.7 - 9.1\mathcal{U}$, $\mathcal{D} = 534 - 208\mathcal{U}$, $\mathcal{Y} = 0.191\rho^{-0.5}$, and $\mathcal{U} = N_v\rho/M$. In these equations, BE is the binding energy of photoelectrons from core level l, m_e is the rest mass of electron, c is the speed of light, N_v is the total number of valence electrons per molecule, ρ is bulk density, M is the molecular weight, $E_p = 28.816(N_v.\rho/M)^{0.5}$ is the free-electron plasmon energy and E_g is the band gap energy in eV. In the case of BTO: $N_v = 24$, $M = 233.19\,\mathrm{g\,mol^{-1}}$ [179], $\rho = 6.02\,\mathrm{g\,cm^{-3}}$ [179] and $E_g = 3.76\,\mathrm{eV}$ [180]. For Ba and Ti we use BE close to the center of the Ba 4d and Ti 2p PE spectra (Figure 5.2), which are 90 eV and 461 eV, respectively. The incident photon energy considered is $E_\nu = 1527\,\mathrm{eV}$, near the Bragg energy E_B of BTO. Therefore, Equation (A.3) yields values of $\lambda_{\mathrm{Ba4d}}(1527\,\mathrm{eV}) = 25.3\,\text{Å}$ and $\lambda_{\mathrm{Ti2p}}(1527\,\mathrm{eV}) = 20.1\,\text{Å}$.

A.4. Calculation of the average out-of-plane lattice parameter and its standard deviation

The average out-of-plane parameters $\bar{c}$ of BTO and SRO layers are computed from the positions of their respective (001) Bragg peaks using the Bragg condition $\bar{c} = (12\,400\,\mathrm{eV\,Å})/(2\overline{E}_\nu \sin\theta_B)$. $\overline{E}_\nu$ represents the weighted average of the energy values E_ν around the (001) Bragg peak, with weights proportional to the diffraction intensity at each corresponding energy E_ν. The broadening of the diffraction curves is determined using the formula $c_{\mathrm{std}} = (1\,240\,000\,\mathrm{eV})/(2E_{\nu,\mathrm{std}} \sin\theta)$, where $E_{\nu,\mathrm{std}}$ represents the standard deviation of the energy values around the (001) BTO peak, weighted by $I_{\mathrm{XRD}}(E_\nu)$. The energy ranges for calculating $\overline{E}_\nu$ of BTO and SRO are varied in the region where the $R_0(E_\nu)$ has finite values. Table A.1 indicates the energy ranges for calculating $\overline{E}_\nu$ of BTO and SRO in the absence of optical pump and at the negative delay.

Table A.1.: The energy ranges for calculating $\overline{E}_\nu$ of BTO and SRO.

Sample	E_ν around BTO (eV)	E_ν around SRO (eV)
BTO/SRO/DSO	1510 - 1547.5	1587 - 1624
BTO/SRO/GSO	1510 - 1547.5	1587 - 1624
BTO/SRO/SSO	1510 - 1547.5	1587 - 1624
BTO/SRO*/GSO	1508.3 - 1545.5	1576.1 -1595.1

A.5. Comparison of fits based on different depth distribution of the out-of-plane lattice parameter

In this section, we compare the fits of (001) Bragg reflectivity $R_0(E_\nu)$ based on the exponential and linear distribution of the out-of-plane lattice parameter c of the BTO thin film in the BTO/SRO/DSO sample. A slightly better fit is provided by the linear distribution of c with residuals less than 5×10^{-3}%. The central offsets of Ti atoms at γ_1, γ_2, and γ_3 obtained based on two models are: $\Delta z_\gamma^{\mathrm{Ti}}$ = 20 pm, 16 pm, 8 pm (exponential model), and $\Delta z_\gamma^{\mathrm{Ti}}$ = 16 pm, 12 pm, 8 pm (linear model). The same trend is reproduced by both models with the difference of only 4 pm in the absolute value for γ_1 and γ_2. This validates the obtained XSW results and supports their robustness to slight modifications in the structural model.

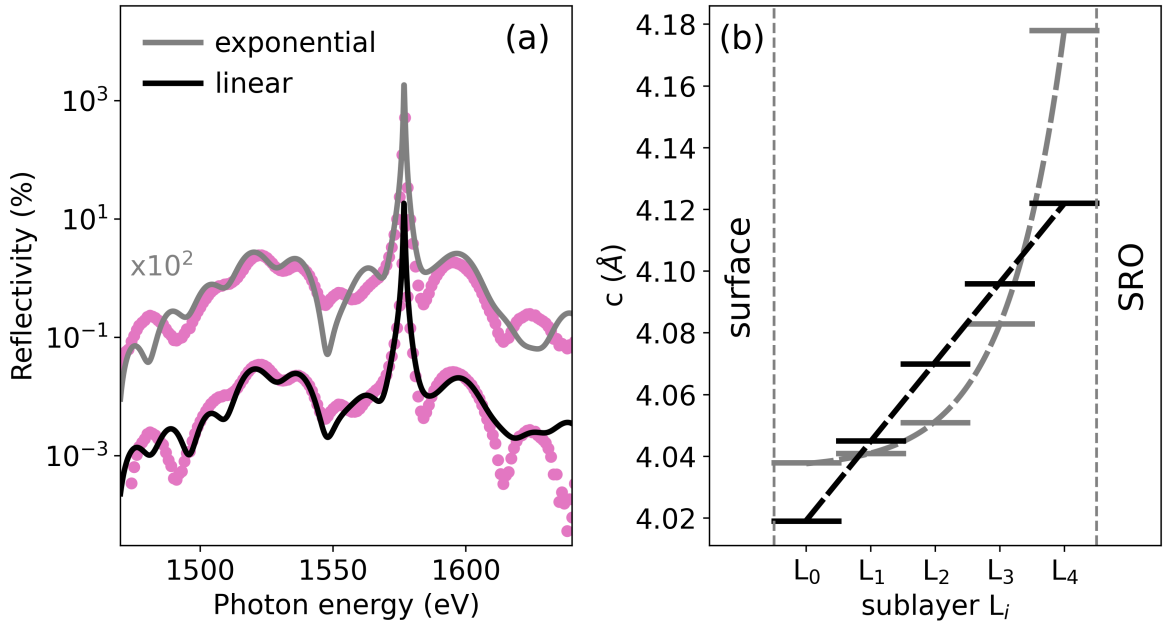

Figure A.1.: Comparison of (001) Bragg reflectivity fits. The BTO/SRO/DSO sample's (001) Bragg reflectivity $R_0(E_\nu)$ (pink dots) and its fit curves based on the exponential (gray) and linear (black) distributions of the out-of-plane lattice parameters c. (b) BTO out-of-plane lattice parameter c_i (solid bars) in sublayers L_i and $c(z)$ (dotted lines) in the exponential (gray) and linear (black) model.

A.6. Photoelectron yield normalization

The PE yield undergoes two stages of normalization: (i) normalization by the incident X-ray intensity, and (ii) normalization by the photoionization cross section.

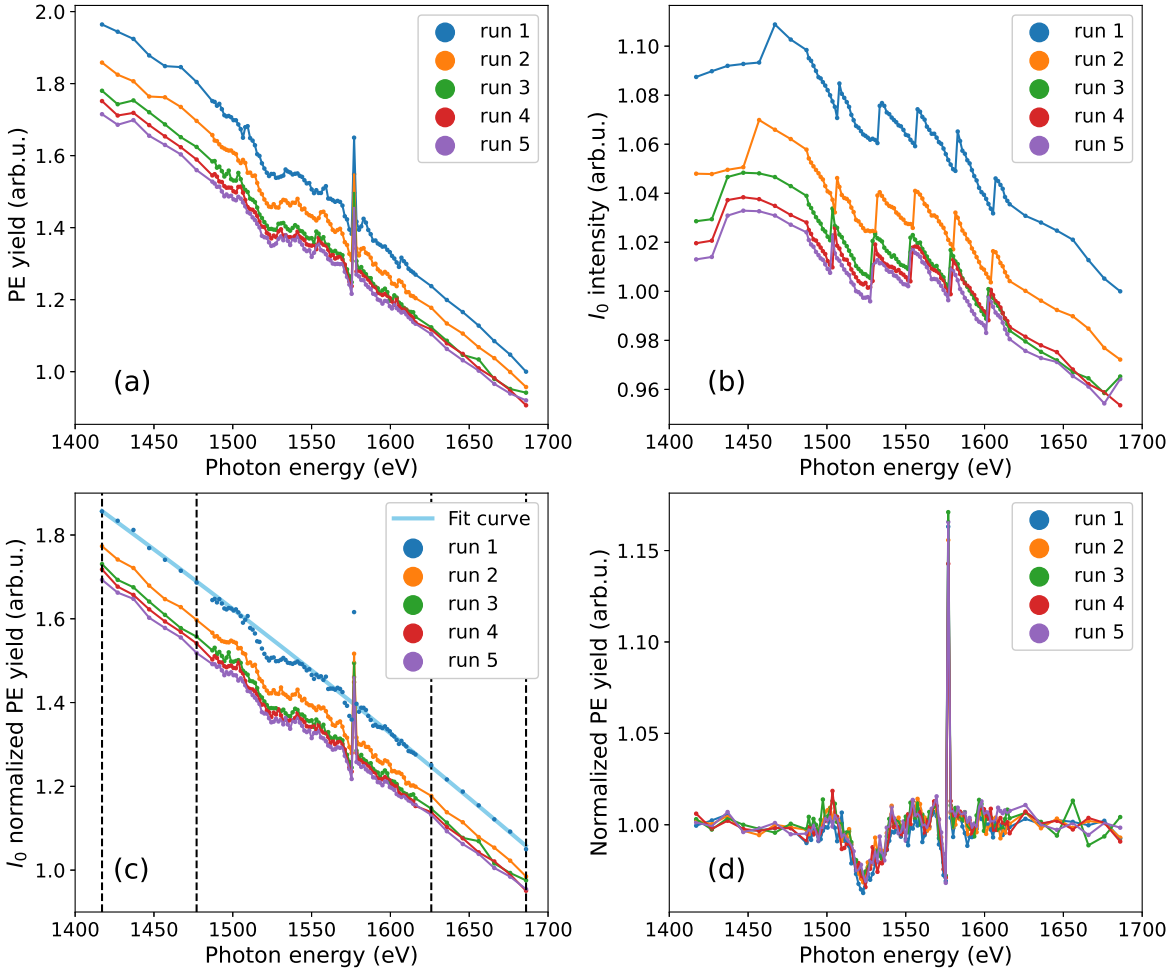

Figure A.2.: Photoelectron yield normalization. (a) Ba 4d PE yield raw data of the BTO/SRO/DSO sample measured in 5 consecutive photon energy scan (run). (b) Incident X-ray beam intensity I_0. (c) PE yield raw data normalized by I_0. (d) PE yield raw data normalized by I_0 and photoionization cross section.

First, the incident X-ray intensity I_0 is measured as the drain current from the last mirror before the sample. The intensity I_0 decreases by about 10 % in the energy range from 1400 to 1700 eV (Figure A.2b) due to the reduced efficiency of the monochromator grating. Additionally, the sawtooth pattern observed in I_0 between 1480 and 1620 eV is caused by top-up electron injection at the Diamond Light Source. The PE yield data normalized by I_0 are presented in Figure A.2c. This normalization reveals a decrease in the PE yield by a factor of approximately 1.8 across the entire photon energy range, attributed to variations in the photoionization cross section [130, 131]. The second normalization step involves dividing the PE yield data by a second-order polynomial fitted to seven points at each end of the yield curve in Figure A.2c, where no XSW effect is evident. An example of this fitting curve is shown in Figure A.2c (blue solid line), and the normalized PE yield curves are presented in Figure A.2d. Finally, for each photon energy I_0, the average and standard deviation of the PE yield data (measured under identical conditions) are computed to obtain the PE yield values and error bars reported in Figure 5.6.

A.7. The uncertainty of Ba and Ti atomic positions

The precision in determining the average atomic positions is ultimately limited by the error bars of the PE yield profiles, which are governed by Poisson statistics. We find that the error bars for the BTO/SRO/SSO sample ($1\% < \sigma_\kappa < 7\%$) are generally larger compared to those of the other two samples ($\sigma_\kappa < 2\%$). This increased uncertainty arises from the higher amount of adsorbates on the BTO/SRO/SSO surface, which reduces the measured PE intensity (see Section 5.1.2). Additionally, lower PE intensity is also associated with a decreasing γ or a smaller $\lambda_{l,\gamma}$, which accounts for the observed increase in σ_κ as γ decreases and the greater uncertainty in Ti positions relative to Ba (see Table 5.3). This greater uncertainty for Ti is further attributed to the lower photoionization cross section of Ti 2p compared to Ba 4d core levels [130, 131].

A.8. Fluence characterization of optical laser

Fluence characterization is essential for a pump-probe experiment. To determine the incident fluences, knife-edge scans are performed to measure the

beam sizes. From these scans, the laser intensity as a function of knife-edge position is obtained and fitted to extract the beam radii, where the beam intensity is $1/e^2$ of the intensity at the beam axis, at the sample surface along the x and y directions (with the xy plane representing the sample surface). The fit function used to determine the beam radius along the x direction, for example, is as follows:

$$I = \mathcal{A}\,\mathrm{erfc}(\sqrt{2}(x - x_0)/w_{0,x}) + \mathcal{B}, \tag{A.4}$$

where $\mathcal{A}$, $\mathcal{B}$, x_0, and $w_{0,x}$ are fit parameters. x_0 represents the position of kinfe edge when it cuts through the center of beam spot, and $w_{0,x}$ is defined as the distance from the beam axis where the intensity drops to $1/e^2$ of the value on the beam axis. Subsequently, the peak fluence is calculated as $F_0 = 2E_p/(\pi w_{0,x} w_{0,y})$ where $E_p = P_L/(f_{train} N_p)$ is the pulse energy with laser power P_L measured by a power meter, the pulse train repetition rate f_{train}, and number of pulses per train N_p; $w_{0,x}$ and $w_{0,y}$ are the beam radii acquired from the knife-edge measurement.

A.9. Time 0 determination

The time delay t_0, which indicates the temporal overlap of the FEL and optical laser during the tr-XRD measurements, was established by fitting I_{XRD} at $E_\nu = 1525\,\mathrm{eV}$ according to the following equation:

$$I_{\mathrm{XRD}}(t) = c_1 \left[-1 + \mathrm{erf}\left(\frac{t - t_0}{\tau_1}\right)\right] \left[c_2 + \exp\left(\frac{t - t_0}{\tau_2}\right)\right] + c_3. \tag{A.5}$$

In Eq. (A.5), τ_1 and τ_2 represent the time constants of the error function and the exponential function, while c_1, c_2 c_3 are normalization factors and offsets. The experimental data shown in Figure A.3 refer to I_{XRD} measurements with high statistics around t_0.

A.10. Bunch arrival time monitor and time resolution of XFEL experiments

The bunch arrival time monitor (BAM) at the European XFEL tracks the timing of electron bunches within each pulse train, offering critical information to enhance the time resolution of pump-probe experiments [181, 182]. In

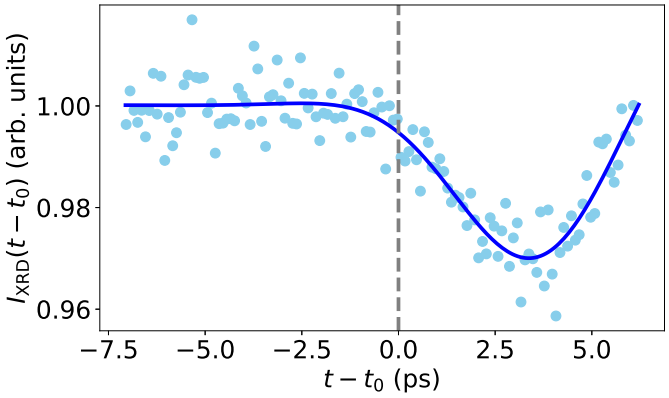

Figure A.3.: Time 0 determination. I_{XRD} data measured at $E_\nu = 1525\,\text{eV}$ in the delay range $-7\,\text{ps} < t - t_0 < 6.2\,\text{ps}$.

our study, the standard deviation of the BAM within a single pulse train was $\approx 10\,\text{fs}$, while the variation between different pulse trains was $\approx 84\,\text{fs}$. Notably, there were slow drifts in the arrival times of FEL pulses over hours, as illustrated in Figure A.4 for each acquired run. Without BAM correction, the time resolution of our experiments would be constrained to approximately $\approx 600\,\text{fs}$. To enhance the time resolution, we corrected the time delays in our data, indicating the relative timing between FEL and optical laser pulses, by using the average BAM value for each pulse train. Consequently, the improved time resolution is expected to be $\Delta t = \sqrt{\Delta t_{\text{FEL}}^2 + \sigma_{t_{\text{FEL}}}^2 + \Delta t_{\text{OL}}^2 + \sigma_{t_{\text{OL}}}^2} \approx 70\,\text{fs}$. This calculation assumes an FEL pulse duration of $\Delta t_{\text{FEL}} = 30\,\text{fs}$, which includes a nominal pulse duration of 25 fs [77] plus 5 fs due to pulse stretching at the monochromator [78], a pulse-to-pulse jitter of $\sigma_{t_{\text{FEL}}} = 10\,\text{fs}$, an optical laser pulse duration of $\Delta t_{\text{OL}} = 50\,\text{fs}$ and a temporal jitter of $\sigma_{t_{\text{OL}}} \approx 30\,\text{fs}$.

A.11. Penetration depth, reflectance at interfaces and transmittance profile

The absorption coefficient α of the 266 nm pump laser in our BTO thin film was derived from the relationship between α and strain described in Ref. [149]. For a compressive strain of -0.63%, the penetration depth is given by $\delta_{\text{BTO}} = 1/\alpha_{\text{BTO}} = 18.2\,\text{nm}$. The penetration depths in the SRO thin film

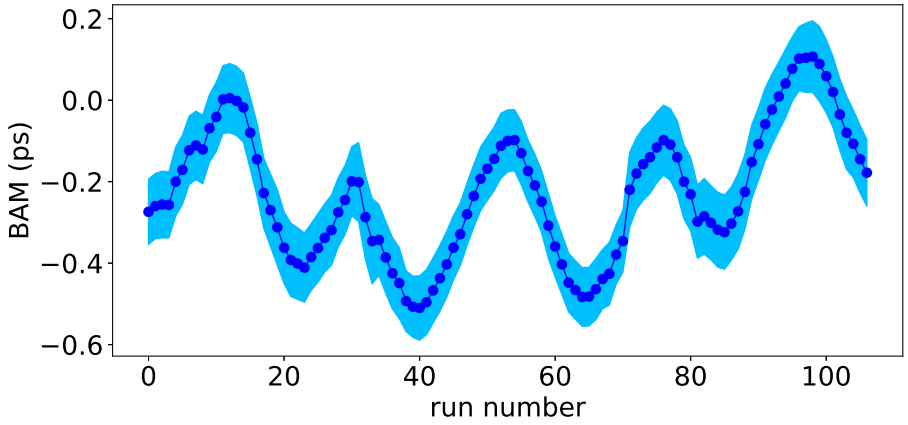

Figure A.4.: Beam arrival monitor data. Mean and standard deviation of the BAM values of runs acquired within 60 h.

($\delta_{\mathrm{SRO}} = 21.5\,\mathrm{nm}$) and in the GSO substrate ($\delta_{\mathrm{GSO}} = 26.1\,\mathrm{nm}$) were obtained using the dielectric constants ϵ_1 and ϵ_2 reported in [183]. Particularly, the penetration depth δ is calculated as $\delta = 1/\alpha = \lambda/(4\pi k)$, where $\lambda = 266\,\mathrm{nm}$ is the wavelength of the pump laser, and k is the imaginary part of the complex index of refraction $n^* = n + ik$. Here, n and k are given by $n = \sqrt{(|\epsilon^*| + \epsilon_1)/2}$ and $k = \sqrt{(|\epsilon^*| - \epsilon_1)/2}$ with $|\epsilon^*| = \sqrt{\epsilon_1^2 + \epsilon_2^2}$.

The reflections at the air/BTO interface $R_p^{\mathrm{BTO}} = 0.178$, at the BTO/SRO interface $R_p^{\mathrm{SRO}} = 0.022$ and at the SRO/GSO interface $R_p^{\mathrm{GSO}} = 0.018$ were computed employing Snell's law $n_1 \sin\theta_i = n_2 \sin\theta_t$ and Fresnel equation for p-polarized light $R_p = |(n_1 \cos\theta_t - n_2 \cos\theta_i)/(n_1 \cos\theta_t + n_2 \cos\theta_i)|^2$. In this context, n_1 and n_2 represent the real parts of the complex refractive index n^* on either side of the interface, while θ_i and θ_t are the angles of incidence and the transmission relative to the surface normal. The refractive indices for SRO and GSO are derived from [183], as previously detailed, whereas the refractive index of the BTO thin film was obtained from ellipsometry measurements at 266 nm [149]. Specifically, the complex dielectric function is given by $\epsilon^* = \epsilon_1 + i\epsilon_2 = \sin\theta_i^2[1 + \tan\theta_i^2(\frac{1-\rho}{1+\rho})^2]$, where $\rho = \tan\Psi \exp(i\Delta)$, with Ψ and Δ provided in [149].

Using the parameters mentioned above, the transmittance of the 266 nm beam through our sample, as shown in Figure A.5, is determined by the following calculation:

$$T_{\mathrm{BTO}}(z) = \exp\left(-\frac{z}{\delta_{\mathrm{BTO}}\cos\theta_t^{\mathrm{BTO}}}\right), \quad 0 < z < t_{\mathrm{BTO}}, \tag{A.6}$$

$$\begin{aligned} T_{\mathrm{SRO}}(z) = {} & T_{\mathrm{BTO}}(t_{\mathrm{BTO}})\left(1 - R_p^{\mathrm{SRO}}\right) \\ & \times \exp\left(-\frac{z - t_{\mathrm{BTO}}}{\delta_{\mathrm{SRO}}\cos\theta_t^{\mathrm{SRO}}}\right), \quad t_{\mathrm{BTO}} < z < t_{\mathrm{BTO}} + t_{\mathrm{SRO}}, \end{aligned} \tag{A.7}$$

$$\begin{aligned} T_{\mathrm{GSO}}(z) = {} & T_{\mathrm{SRO}}(t_{\mathrm{BTO}} + t_{\mathrm{SRO}})\left(1 - R_p^{\mathrm{GSO}}\right) \\ & \times \exp\left(-\frac{z - (t_{\mathrm{BTO}} + t_{\mathrm{SRO}})}{\delta_{\mathrm{GSO}}\cos\theta_t^{\mathrm{GSO}}}\right), \quad z > t_{\mathrm{BTO}} + t_{\mathrm{SRO}}. \end{aligned} \tag{A.8}$$

As a result, the absorbed fluences in the BTO and SRO thin films are:

$$\begin{aligned} F_{\mathrm{abs}}^{\mathrm{BTO}} &= F_{\mathrm{in}}(1 - R_p^{\mathrm{BTO}})\left(1 - \exp\left(-\frac{t_{\mathrm{BTO}}}{\delta_{\mathrm{BTO}}\cos\theta_t^{\mathrm{BTO}}}\right)\right) \\ &= 0.7\, F_{\mathrm{in}}, \end{aligned} \tag{A.9}$$

$$\begin{aligned} F_{\mathrm{abs}}^{\mathrm{SRO}} &= F_{\mathrm{in}}(1 - R_p^{\mathrm{BTO}})\exp\left[-\frac{t_{\mathrm{BTO}}}{\delta_{\mathrm{BTO}}\cos\theta_t^{\mathrm{BTO}}}\right] \\ &\quad \times \left[1 - \exp\left(-\frac{t_{\mathrm{SRO}}}{\delta_{\mathrm{SRO}}\cos\theta_t^{\mathrm{SRO}}}\right)\right] \\ &= 0.12\, F_{\mathrm{in}}. \end{aligned} \tag{A.10}$$

For $F_{\mathrm{in}} = 2.7\,\mathrm{mJ\,cm^{-2}}$, $F_{\mathrm{abs}}^{\mathrm{BTO}} = 1.88\,\mathrm{mJ\,cm^{-2}}$ and $F_{\mathrm{abs}}^{\mathrm{SRO}} = 0.33\,\mathrm{mJ\,cm^{-2}}$, while for $F_{\mathrm{in}} = 1.4\,\mathrm{mJ\,cm^{-2}}$, $F_{\mathrm{abs}}^{\mathrm{BTO}} = 0.98\,\mathrm{mJ\,cm^{-2}}$ and $F_{\mathrm{abs}}^{\mathrm{SRO}} = 0.17\,\mathrm{mJ\,cm^{-2}}$.

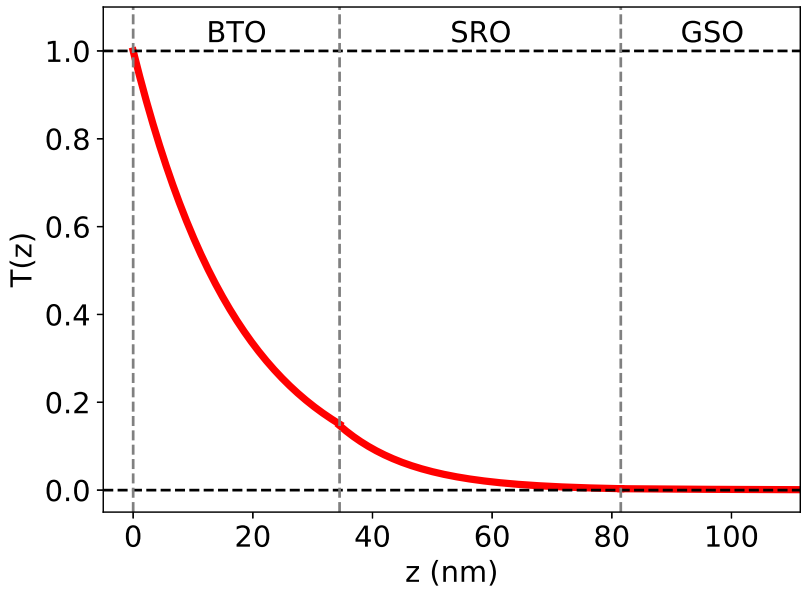

Figure A.5.: Transmittance profile $T(z)$ of the 266 nm pump laser in the BTO/SRO*/GSO sample. The dashed gray lines denote the BTO surface, the BTO/SRO and the SRO/GSO interfaces.

A.12. Analytical solutions of two-temperature model

In this section, we outline the parameters utilized in the 2TM model and then proceed to the analytical solution. In Equation (6.1), the source term, which denotes the absorbed fluence of the optical laser as a function of t and z and is expressed as $S(z,t) = F_{\text{abs}} \exp\left(-z/(\delta \cos\theta_t)\right) \exp\left(-t^2/(2\Delta t_{\text{OL}}^2)\right)/(\delta \Delta t_{\text{OL}})$. We now turn our attention to solving the 2TM. The second equation in Equation (6.1) can be formulated as follows:

$$T_e = \frac{C_p}{g}\frac{\partial T_p}{\partial t} + T_p, \tag{A.11}$$

which is then substituted into the first equation of Equation (6.1), resulting in the following second-order differential equation for T_p:

$$\frac{C_e C_p}{g}\frac{\partial^2 T_p}{\partial t^2} + (C_e + C_p)\frac{\partial T_p}{\partial t} = S(z,t). \tag{A.12}$$

Using the initial and boundary conditions $T_e(z,0) = T_p(z,0) = T_0 = 300\,\text{K}$, $\frac{\partial T_p}{\partial z}(0,t) = 0$, $\frac{\partial T_p}{\partial t}(z,0) = 0$, we can derive the lattice temperature $T_p(z,t)$ as the analytical solution of Equation (A.12):

$$\begin{aligned} T_p(z,t) = T_0 \\ &+ \frac{\sqrt{\pi}\mathcal{C}\Delta t_{\text{OL}}}{\sqrt{2}\mathcal{B}} \exp\left(\frac{\Delta t_{\text{OL}}^2 \mathcal{B}^2}{2\mathcal{A}^2}\right) \\ &\times \text{erf}\left(\frac{\mathcal{B}\Delta t_{\text{OL}}}{\sqrt{2}\mathcal{A}} - \frac{t}{\sqrt{2}\Delta t_{\text{OL}}}\right) \exp\left(-\frac{z}{\delta}\right) \exp\left(-\frac{\mathcal{B}}{\mathcal{A}}t\right) \\ &+ \frac{\sqrt{\pi}\mathcal{C}\Delta t_{\text{OL}}}{\sqrt{2}\mathcal{B}} \exp\left(-\frac{z}{\delta}\right) \text{erf}\left(\frac{t}{\sqrt{2}\Delta t_{\text{OL}}}\right) \\ &- \frac{\sqrt{\pi}\mathcal{C}\Delta t_{\text{OL}}}{\sqrt{2}\mathcal{B}} \exp\left(\frac{\Delta t_{\text{OL}}^2 \mathcal{B}^2}{2\mathcal{A}^2}\right) \\ &\times \text{erf}\left(\frac{\mathcal{B}\Delta t_{\text{OL}}}{\sqrt{2}\mathcal{A}}\right) \exp\left(-\frac{z}{\delta}\right) \exp\left(-\frac{\mathcal{B}}{\mathcal{A}}t\right). \end{aligned} \tag{A.13}$$

where $\mathcal{A} = C_e C_p/g$, $\mathcal{B} = C_e + C_p$, and $\mathcal{C} = (1/\delta)F_a$. By inserting Equation (A.13) into Equation (A.11), we derive the electron temperature $T_e(z,t)$:

$$
\begin{aligned}
T_e(z,t) = T_0 & \\
& - \frac{\sqrt{\pi}\mathcal{C}\Delta t_{\mathrm{OL}}}{\sqrt{2}\mathcal{B}} \frac{C_p}{C_e} \exp\left(\frac{\Delta t_{\mathrm{OL}}^2 \mathcal{B}^2}{2\mathcal{A}^2}\right) \\
& \times \operatorname{erf}\left(\frac{\mathcal{B}\Delta t_{\mathrm{OL}}}{\sqrt{2}\mathcal{A}} - \frac{t}{\sqrt{2}\Delta t_{\mathrm{OL}}}\right) \exp\left(-\frac{z}{\delta}\right) \exp\left(-\frac{\mathcal{B}}{\mathcal{A}} t\right) \\
& + \frac{\sqrt{\pi}\mathcal{C}\Delta t_{\mathrm{OL}}}{\sqrt{2}\mathcal{B}} \exp\left(-\frac{z}{\delta}\right) \operatorname{erf}\left(\frac{t}{\sqrt{2}\Delta t_{\mathrm{OL}}}\right) \\
& + \frac{\sqrt{\pi}\mathcal{C}\Delta t_{\mathrm{OL}}}{\sqrt{2}\mathcal{B}} \frac{C_p}{C_e} \exp\left(\frac{\Delta t_{\mathrm{OL}}^2 \mathcal{B}^2}{2\mathcal{A}^2}\right) \\
& \times \operatorname{erf}\left(\frac{\mathcal{B}\Delta t_{\mathrm{OL}}}{\sqrt{2}\mathcal{A}}\right) \exp\left(-\frac{z}{\delta}\right) \exp\left(-\frac{\mathcal{B}}{\mathcal{A}} t\right).
\end{aligned}
\tag{A.14}
$$

A.13. Analytical solution of the 1D strain wave equation

The thermoelastic and deformation potential contributions to the stress in Equation (6.2) can be expressed explicitly as:

$$\sigma_{TE} = -3B\beta(T_p - T_0) \tag{A.15}$$

and

$$\sigma_{DP} = -N_e B \frac{\partial E_g}{\partial p}, \tag{A.16}$$

where $E_g = 3.4\,\mathrm{eV}$ represents the equilibrium bandgap [149], $N_e = C_e(T_e - T_0)/(E - E_g)$ denotes the carrier density (with unit m^{-3}), E is the photon energy of the optical laser, and $\delta E = N_e(E - E_g)$ indicates the total energy imparted to the electronic subsystem [51]. By substituting Equation (A.15) and A.16 into Equation (6.2), we derive:

$$\sigma(z,t) = \rho v^2 \eta(z,t) - 3B\beta(T_p(z,t) - T_0) - \frac{C_e(T_e(z,t) - T_0)}{E - E_g} B \frac{\partial E_g}{\partial p}. \tag{A.17}$$

Table A.2.: Physical constants used in the calculations of the two-temperature model and strain wave propagation. The film thicknesses t are obtained from theta-2-theta measurements (Section 4.4). The penetration depth δ and the reflectance R_p are detailed in A.11. The volumetric heat capacities C_e and C_p for SRO and GSO are derived from [139] and [140], respectively, while for BTO, they are discussed in Section 6.1.2 . The mass density ρ, the bulk modulus B, and the Poisson ratio ν are sourced from [184]. The longitudinal sound velocity v is calculated using $v = \sqrt{3B(1-\nu)/[\rho(1+\nu)]}$ [50]. The linear expansion coefficient β of SRO and GSO is taken from [139] and [185], respectively, while β_{BTO} is determined as a fitting parameter as discussed in the Section 6.1.2.

constants	unit	BTO	SRO	GSO
t	nm	34.5	47	0.5×10^6
δ	nm	18.2	21.5	26.1
R_p	-	0.178	0.022	0.018
C_p	$\mathrm{J\,m^{-3}\,K^{-1}}$	2.8×10^6	2.8×10^6 [139]	2.1×10^6 [140]
C_e	$\mathrm{J\,m^{-3}\,K^{-1}}$	4.2×10^4	2.3×10^5 [139]	9×10^4 [140]
g	$\mathrm{W\,m^{-3}\,K^{-1}}$	-	5×10^{17}	5×10^{17}
ρ [184]	$\mathrm{g\,cm^{-3}}$	5.93	6.46	6.6
m [186]	$\mathrm{g\,mol^{-1}}$	233.19	236.69	250.2
β	$\mathrm{K^{-1}}$	-	1.03×10^{-5} [139]	1.09×10^{-5} [187]
K_p	$\mathrm{W\,m^{-1}\,K^{-1}}$	2.73 [138]	5.72 [139]	2.53 [140]
D_p	$\mathrm{mm^2\,s^{-1}}$	1.11 [138]	2.05 [139]	1.22 [140]
B [184]	GPa	107	166	163
ν [184]	-	0.3	0.31	0.29
v [50]	$\mathrm{m\,s^{-1}}$	5399	6372	6386

Equation (6.3) can be reformulated in terms of $\eta(z,t) = \partial u(z,t)/\partial z$:

$$\frac{\partial^2 \eta(z,t)}{\partial t^2} = \frac{1}{\rho}\frac{\partial^2 \sigma(z,t)}{\partial z^2}. \tag{A.18}$$

By substituting Equation (A.17) into Equation A.18, we obtain:

$$\frac{\partial^2 \eta(z,t)}{\partial t^2} = v^2\frac{\partial^2 \eta(z,t)}{\partial z^2} - \frac{3B\beta}{\rho\delta^2}(T_p(z,t) - T_0) - \frac{C_e}{\rho(E-E_g)\delta^2}B\frac{\partial E_g}{\partial p}(T_e(z,t) - T_0). \tag{A.19}$$

With the initial conditions $\eta(z,0) = 0, \frac{\partial \eta}{\partial t}(z,0) = 0, \sigma(0,t) = 0$ [50], the out-of-plane strain profile $\eta(z,t)$ can be determined by solving the analytical integrals

provided in Equation (A.19) [188]:

$$\eta(z,t) = \begin{cases} \frac{1}{2v}\int_0^t \int_{z-v(t-\tau)}^{z+v(t-\tau)} \mathfrak{F}(\xi,\tau)d\xi d\tau, & \text{for } t < \frac{z}{v} \\ \frac{1}{2v}\int_0^{t-\frac{z}{v}} \int_{v(t-\tau)-z}^{z+v(t-\tau)} \mathfrak{F}(\xi,\tau)d\xi d\tau & \\ +\frac{1}{2v}\int_{t-\frac{z}{v}}^t \int_{z-v(t-\tau)}^{z+v(t-\tau)} \mathfrak{F}(\xi,\tau)d\xi d\tau + \mathfrak{F}(0,t-z/v)\frac{\delta^2}{v^2}, & \text{for } t > \frac{z}{v}, \end{cases} \tag{A.20}$$

where $\mathfrak{F}(z,t) = -3B\beta(T_p(z,t)-T_0)/(\rho\delta^2) - C_eB\frac{\partial E_g}{\partial p}(T_e(z,t)-T_0)/(\rho(E-E_g)\delta^2)$.

For a strain pulse originating from the BTO surface, it undergoes partial reflection at the BTO/SRO interface due to the difference in acoustic impedance $Z = \rho * v$. The reflection coefficient is given by $R_Z^{BTO/SRO} = (Z_{SRO} - Z_{BTO})/(Z_{BTO} + Z_{SRO})$. This reflected strain wave is subsequently partially reflected at the BTO surface and then propagates back towards the BTO/SRO interface. A similar process occurs for a strain pulse starting at the BTO/SRO interface, which is partially reflected at the SRO/GSO interface with a reflection coefficient $R_Z^{SRO/GSO} = (Z_{GSO} - Z_{SRO})/(Z_{SRO} + Z_{GSO})$. This reflected wave is then partially reflected at the SRO/BTO interface and propagates forward towards the SRO/GSO interface. For strain pulses starting at the SRO/GSO interface, they continue moving toward the bottom of the system without reflecting within the time frame considered in this study, due to the large thickness of 0.5 mm. The reflection coefficients are $R_Z^{BTO/SRO} = -R_Z^{SRO/BTO} = 0.13$, $R_Z^{BTO/air} = -1$, and $R_Z^{SRO/GSO} = 0.01$.

In general, within the time frame of our analysis, the total out-of-plane strain in the BTO region is the sum of the following strain waves:

- a strain wave starting at the BTO surface, moving towards the BTO/SRO interface: $\eta_{BTO}(z,t)$;
- a strain wave starting at the BTO surface, reflected at the BTO/SRO interface, and moving back towards the BTO surface: $R_Z^{BTO/SRO} * \eta_{BTO}(z,t)$;
- a strain wave starting at the BTO surface, reflected at the BTO/SRO interface, reflected again at the BTO surface, and moving towards the BTO/SRO interface: $R_Z^{BTO/air} * R_Z^{BTO/SRO} * \eta_{BTO}(z,t)$;
- a strain wave starting at the BTO surface, reflected at the BTO/SRO interface, reflected at the BTO surface, and reflected once more at the BTO/SRO interface before moving back towards the BTO surface: $R_Z^{BTO/SRO} * R_Z^{BTO/air} * R_Z^{BTO/SRO} * \eta_{BTO}(z,t)$;

- a strain wave starting at the BTO/SRO interface, reflected at the SRO/GSO interface, transmitted through the BTO/SRO interface, and moving towards the BTO surface: $(1 - R_Z^{SRO/BTO}) * R_Z^{SRO/GSO} * \eta_{SRO}(z,t)$.

In the SRO region, the total out-of-plane strain is the sum of the following strain waves:

- a strain wave starting at the BTO/SRO interface, moving towards the SRO/GSO interface: $\eta_{SRO}(z,t)$;
- a strain wave starting at the BTO/SRO interface, reflected at the SRO/GSO interface, and moving back towards the BTO/SRO interface: $R_Z^{SRO/GSO} * \eta_{SRO}(z,t)$;
- a strain wave starting at the BTO surface, transmitted through the BTO/SRO interface, and moving towards the SRO/GSO interface: $(1 - R_Z^{BTO/SRO}) * \eta_{BTO}(z,t)$;
- a strain wave starting at the BTO surface, transmitted through the BTO/SRO interface, reflected at the SRO/GSO interface, and moving back towards the SRO/BTO interface: $R_Z^{SRO/GSO} * (1 - R_Z^{BTO/SRO}) * \eta_{BTO}(z,t)$;
- a strain wave starting at the BTO surface, reflected at the BTO/SRO interface, reflected again at the BTO surface, transmitted through the BTO/SRO interface, and moving towards the SRO/GSO interface: $(1 - R_Z^{BTO/SRO}) * R_Z^{BTO/air} * R_Z^{BTO/SRO} * \eta_{BTO}(z,t)$.

In the GSO region, the total out-of-plane strain is the sum of the following strain waves:

- a strain wave starting at the SRO/GSO interface, moving towards the bottom: $\eta_{GSO}(z,t)$;
- a strain wave starting at the BTO/SRO interface, transmitted through the SRO/GSO interface, and moving towards the bottom: $(1 - R_Z^{SRO/GSO}) * \eta_{SRO}(z,t)$;
- a strain wave starting at the BTO surface, transmitted through the BTO/SRO interface, transmitted through the SRO/GSO interface, and moving towards the bottom: $(1 - R_Z^{SRO/GSO}) * (1 - R_Z^{BTO/SRO}) * \eta_{BTO}(z,t)$;

- a strain wave starting at the BTO surface, reflected at the BTO/SRO interface, reflected again at the BTO surface, transmitted through the BTO/SRO interface, and transmitted through the SRO/GSO interface before moving towards the bottom: $(1 - R_Z^{SRO/GSO}) * (1 - R_Z^{BTO/SRO}) * R_Z^{BTO/air} * R_Z^{BTO/SRO} * \eta_{BTO}(z,t)$.

When considering the superposition of multiple strain waves in a given region, we disregard terms with the negligibly small product $R_Z^{SRO/GSO} * R_Z^{SRO/BTO} = 0.0009$. Consequently, we use the piecewise function $\eta_{tot}(z,t)$ to simulate the propagation of strain pulses within the sample.

$$\eta_{tot}(z,t) = \begin{cases} \eta_{BTO}(z,t) + R_Z^{BTO/SRO}\eta_{BTO}(z,t) \\ +R_Z^{BTO/air}R_Z^{BTO/SRO}\eta_{BTO}(z,t) \\ +R_Z^{BTO/SRO}R_Z^{BTO/air}R_Z^{BTO/SRO}\eta_{BTO}(z,t) \\ +(1 - R_Z^{SRO/BTO})R_Z^{SRO/GSO}\eta_{SRO}(z,t), \\ \text{for } 0 < z < t_{BTO} \\ \eta_{SRO}(z,t) + R_Z^{SRO/GSO}\eta_{SRO}(z,t) \\ +(1 - R_Z^{BTO/SRO})\eta_{BTO}(z,t) \\ +R_Z^{SRO/GSO}(1 - R_Z^{BTO/SRO})\eta_{BTO}(z,t) \\ +(1 - R_Z^{BTO/SRO})R_Z^{BTO/air}R_Z^{BTO/SRO}\eta_{BTO}(z,t), \\ \text{for } t_{BTO} < z < t_{BTO} + t_{SRO} \\ \eta_{GSO}(z,t) + (1 - R_Z^{SRO/GSO})\eta_{SRO}(z,t) \\ +(1 - R_Z^{SRO/GSO})(1 - R_Z^{BTO/SRO})\eta_{BTO}(z,t) \\ +(1 - R_Z^{SRO/GSO})(1 - R_Z^{BTO/SRO})R_Z^{BTO/air}R_Z^{BTO/SRO}\eta_{BTO}(z,t), \\ \text{for } t_{BTO} + t_{SRO} < z < t_{BTO} + t_{SRO} + t_{GSO} \end{cases}$$

A.14. Damage threshold of $BaTiO_3$ thin film

The damage of the sample is revealed by a decrease in the ratio of the polar patterns, measured after and before a delay scan measurement, below 0.9 (Figure A.6b). Beyond the fluence threshold, the maximum increase in $\Delta R/R$ and the maximum drop in $\Delta I^s_{\mathrm{SHG}}/I^s_{\mathrm{SHG}}$ deviate from the linear regime (Figure A.6a).

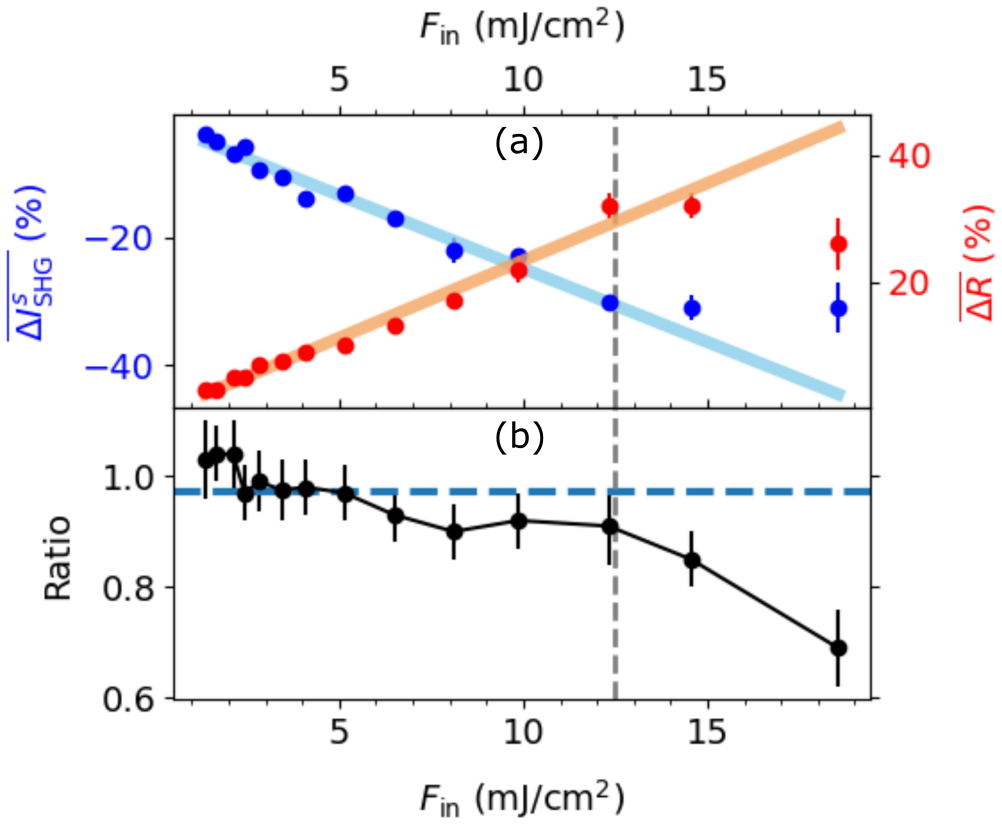

Figure A.6.: Fluence dependence of the changes in the optical reflectance and the SHG intensity. (a): Fluence dependence of the maximum increase of $\Delta R/R$ (red) and the maximum decrease of $\Delta I^s_{SHG}/I^s_{SHG}$ (blue) and their corresponding linear fits (light red for $\Delta R/R$ and light blue for $\Delta I^s_{SHG}/I^s_{SHG}$). (b): The ratio of the polar patterns measured after and before the delay scan measurement (black). The blue dashed line indicates the average of all data points below 12.5 mJ cm^{-2}.

List of Figures

List of Tables

Bibliography

1. Fernandez, A. *et al.* Thin-Film Ferroelectrics. *Adv. Mater.* **34,** 2108841 (2022).doi:10.1002/adma.202108841
2. Khan, A. I., Keshavarzi, A. & Datta, S. The future of ferroelectric field-effect transistor technology. *Nat. Electron.* **3,** 588–597 (2020).doi:10.1038/s41928-020-00492-7
3. Qi, L., Ruan, S. & Zeng, Y.-J. Review on Recent Developments in 2D Ferroelectrics: Theories and Applications. *Adv. Mater.* **33,** 2005098 (2021).doi:10.1002/adma.202005098
4. Han, X., Ji, Y. & Yang, Y. Ferroelectric Photovoltaic Materials and Devices. *Adv. Funct. Mater.* **32,** 2109625 (2022).doi:10.1002/adfm.202109625
5. Jona, F. & Shirane, G. *Ferroelectric crystals* (Dover Publications, Inc., New York, 1993).
6. Choi, K. J. *et al.* Enhancement of Ferroelectricity in Strained $BaTiO_3$ Thin Films. *Science* **306,** 1005–1009 (2004).doi:10.1126/science.1103218
7. Schlom, D. G. *et al.* Strain Tuning of Ferroelectric Thin Films. *Annu. Rev. Mater. Res.* **37,** 589–626 (2007).doi:10.1146/annurev.matsci.37.061206.113016
8. Catalan, G., Noheda, B., McAneney, J., Sinnamon, L. J. & Gregg, J. M. Strain gradients in epitaxial ferroelectrics. *Phys. Rev. B* **72,** 020102 (2005).doi:10.1103/PhysRevB.72.020102
9. Gattinoni, C. *et al.* Interface and surface stabilization of the polarization in ferroelectric thin films. *Proc. Natl. Acad. Sci.* **117,** 28589–28595 (2020).doi:10.1073/pnas.2007736117
10. Deleuze, P.-M., Domenichini, B. & Dupont, C. Ferroelectric polarization switching induced from water adsorption in $BaTiO_3$ ultrathin films. *Phys. Rev. B* **101,** 075410 (2020).doi:10.1103/PhysRevB.101.075410

11. Shin, J. *et al.* Atomistic Screening Mechanism of Ferroelectric Surfaces: An In Situ Study of the Polar Phase in Ultrathin $BaTiO_3$ Films Exposed to H_2O. *Nano Lett.* **9,** 3720–3725 (2009).doi:10.1021/nl901824x
12. Wang, J. L. *et al.* Chemistry and Atomic Distortion at the Surface of an Epitaxial $BaTiO_3$ Thin Film after Dissociative Adsorption of Water. *J. Phys. Chem. C* **116,** 21802–21809 (2012).doi:10.1021/jp305826e
13. Lee, H. *et al.* Imprint Control of $BaTiO_3$ Thin Films via Chemically Induced Surface Polarization Pinning. *Nano Lett.* **16,** 2400–2406 (2016).doi:10.1021/acs.nanolett.5b05188
14. Park, C. H. & Chadi, D. J. Effect of Interstitial Hydrogen Impurities on Ferroelectric Polarization in $PbTiO_3$. *Phys. Rev. Lett.* **84,** 4717–4720 (2000).doi:10.1103/PhysRevLett.84.4717
15. Tian, Y. *et al.* Water printing of ferroelectric polarization. *Nat. Commun.* **9,** 3809 (2018).doi:10.1038/s41467-018-06369-w
16. Shin, J. *et al.* Polar distortion in ultrathin $BaTiO_3$ films studied by *in situ* LEED IV. *Phys. Rev. B* **77,** 245437 (2008).doi:10.1103/PhysRevB.77.245437
17. Gao, P. *et al.* Atomic mechanism of polarization-controlled surface reconstruction in ferroelectric thin films. *Nat. Commun.* **7,** 11318 (2016).doi:10.1038/ncomms11318
18. Domingo, N. *et al.* Surface charged species and electrochemistry of ferroelectric thin films. *Nanoscale* **11,** 17920–17930 (2019).doi:10.1039/c9nr05526f
19. Wang, R. V. *et al.* Reversible Chemical Switching of a Ferroelectric Film. *Phys. Rev. Lett.* **102,** 047601 (2009).doi:10.1103/PhysRevLett.102.047601
20. Garrity, K., Kolpak, A. M., Ismail-Beigi, S. & Altman, E. I. Chemistry of Ferroelectric Surfaces. *Adv. Mater.* **22,** 2969–2973 (2010).doi:https://doi.org/10.1002/adma.200903723
21. Kakekhani, A. & Ismail-Beigi, S. Ferroelectric-Based Catalysis: Switchable Surface Chemistry. *ACS Catal.* **5,** 4537–4545 (2015).doi:10.1021/acscatal.5b00507
22. Kakekhani, A. & Ismail-Beigi, S. Polarization-driven catalysis via ferroelectric oxide surfaces. *Phys. Chem. Chem. Phys.* **18,** 19676–19695 (2016).doi:10.1039/C6CP03170F

23. Vonrüti, N. & Aschauer, U. Catalysis on oxidized ferroelectric surfaces-Epitaxially strained $LaTiO_2N$ and $BaTiO_3$ for photocatalytic water splitting. *J. Chem. Phys.* **152,** 024701 (2020).doi:10.1063/1.5135751

24. Wan, T. L. *et al.* Catalysis based on ferroelectrics: controllable chemical reaction with boosted efficiency. *Nanoscale* **13,** 7096–7107 (2021).doi:10.1039/D1NR00847A

25. Lan, Z. *et al.* Enhancing Oxygen Evolution Reaction Activity by Using Switchable Polarization in Ferroelectric $InSnO_2N$. *ACS Catal.* **11,** 12692–12700 (2021).doi:10.1021/acscatal.1c03737

26. Lian, C., Ali, Z. A., Kwon, H. & Wong, B. M. Indirect but Efficient: Laser-Excited Electrons Can Drive Ultrafast Polarization Switching in Ferroelectric Materials. *The Journal of Physical Chemistry Letters* **10,** 3402–3407 (2019).doi:10.1021/acs.jpclett.9b01046

27. Chen, C. & Yi, Z. Photostrictive Effect: Characterization Techniques, Materials, and Applications. *Advanced Functional Materials* **31,** 2010706 (2021).doi:https://doi.org/10.1002/adfm.202010706

28. Kundys, B. Photostrictive materials. *Applied Physics Reviews* **2,** 011301 (2015).doi:10.1063/1.4905505

29. Poosanaas, P., Tonooka, K. & Uchino, K. Photostrictive actuators. *Mechatronics* **10,** 467–487 (2000).doi:https://doi.org/10.1016/S0957-4158(99)00073-2

30. Sarott, M. F. *et al.* Reversible Optical Control of Polarization in Epitaxial Ferroelectric Thin Films. *Advanced Materials* **36,** 2312437 (2024).doi:https://doi.org/10.1002/adma.202312437

31. Rubio-Marcos, F., Del Campo, A., Marchet, P. & Fernández, J. F. Ferroelectric domain wall motion induced by polarized light. *Nature Communications* **6,** 6594 (2015).doi:10.1038/ncomms7594

32. Rubio-Marcos, F. *et al.* Reversible optical control of macroscopic polarization in ferroelectrics. *Nature Photonics* **12,** 29–32 (2018).doi:10.1038/s41566-017-0068-1

33. Rubio-Marcos, F. *et al.* Light-induced strain and its correlation with the optical absorption at charged domain walls in polycrystalline ferroelectrics. *Applied Materials Today* **32,** 101838 (2023).doi:https://doi.org/10.1016/j.apmt.2023.101838

34. Tsai, H. *et al.* Light-induced lattice expansion leads to high-efficiency perovskite solar cells. *Science* **360,** 67–70 (2018).doi:10.1126/science.aap8671

35. Li, W. *et al.* Light-activated interlayer contraction in two-dimensional perovskites for high-efficiency solar cells. *Nature Nanotechnology* **17,** 45–52 (2022).doi:10.1038/s41565-021-01010-2

36. Ishikawa, T. Accelerator-based X-ray sources: synchrotron radiation, X-ray free electron lasers and beyond. *Philosophical Transactions of the Royal Society A: Mathematical, Physical and Engineering Sciences* **377,** 20180231 (2019).doi:10.1098/rsta.2018.0231

37. Batterman, B. W. & Cole, H. Dynamical Diffraction of X Rays by Perfect Crystals. *Rev. Mod. Phys.* **36,** 681–717 (1964).doi:10.1103/RevModPhys.36.681

38. Materlik, G. & Zegenhagen, J. X-ray standing wave analysis with synchrotron radiation applied for surface and bulk systems. *Phys. Lett. A* **104,** 47–50 (1984).doi:10.1016/0375-9601(84)90587-5

39. Zegenhagen, J. Surface structure determination with X-ray standing waves. *Surf. Sci. Rep.* **18,** 202–271 (1993).doi:10.1016/0167-5729(93)90025-K

40. Woodruff, D. P. Surface structure determination using x-ray standing waves. *Rep. Prog. Phys.* **68,** 743 (2005).doi:10.1088/0034-4885/68/4/R01

41. Zegenhagen, J. & Kazimirov, A. *The X-ray Standing Wave Technique: Principles and Applications* (World Scientific, 2013).

42. Trucano, P. Use of dynamical diffraction effects on x-ray fluorescence to determine the polarity of GaP single crystals. *Phys. Rev. B* **13,** 2524–2531 (1976).doi:10.1103/PhysRevB.13.2524

43. Kazimirov, A. *et al.* Polarity determination of a GaN thin film on sapphire (0001) with x-ray standing waves. *J. Appl. Phys.* **84,** 1703–1705 (1998).doi:10.1063/1.368240

44. Kazimirov, A. *et al.* High-resolution x-ray study of thin GaN film on SiC. *J. Appl. Phys.* **89,** 6092–6097 (2001).doi:10.1063/1.1364644

45. Bedzyk, M. J. *et al.* Probing the polarity of ferroelectric thin films with x-ray standing waves. *Phys. Rev. B* **61,** R7873–R7876 (2000).doi:10.1103/PhysRevB.61.R7873

46. Marasco, D. L. *et al.* Atomic-scale observation of polarization switching in epitaxial ferroelectric thin films. *Appl. Phys. Lett.* **79,** 515–517 (2001).doi:10.1063/1.1385349

47. Boyd, R. W. *Nonlinear Optics* 3rd (Academic Press, 2003).

48. Fiebig, M., Pavlov, V. V. & Pisarev, R. V. Second-harmonic generation as a tool for studying electronic and magnetic structures of crystals: review. *J. Opt. Soc. Am. B* **22,** 96–118 (2005).doi:10.1364/JOSAB.22.000096

49. Fiebig, M. in *Nonlinear Optics on Ferroic Materials* (John Wiley & Sons, Ltd, 2023). doi:https://doi.org/10.1002/9783527822812.ch4.doi:https://doi.org/10.1002/9783527822812.ch4

50. Thomsen, C., Grahn, H. T., Maris, H. J. & Tauc, J. Surface generation and detection of phonons by picosecond light pulses. *Phys. Rev. B* **34,** 4129–4138 (1986).doi:10.1103/PhysRevB.34.4129

51. Ruello, P. & Gusev, V. E. Physical mechanisms of coherent acoustic phonons generation by ultrafast laser action. *Ultrasonics* **56,** 21–35 (2015).doi:https://doi.org/10.1016/j.ultras.2014.06.004

52. Jablonski, A. & Powell, C. Relationships between electron inelastic mean free paths, effective attenuation lengths, and mean escape depths. *Journal of Electron Spectroscopy and Related Phenomena* **100,** 137–160 (1999).doi:10.1016/S0368-2048(99)00044-4

53. Jablonski, A. & Powell, C. J. The electron attenuation length revisited. *Surf. Sci. Rep.* **47,** 33–91 (2002).doi:10.1016/S0167-5729(02)00031-6

54. Bragg, W. H. & Bragg, W. L. The reflection of X-rays by crystals. *Proceedings of the Royal Society of London. Series A, Containing Papers of a Mathematical and Physical Character* **88,** 428–438 (1913).doi:10.1098/rspa.1913.0040

55. Seeck, O. H. & Murphy, B. *X-Ray Diffraction: Modern Experimental Techniques* Boca Raton, 2014.

56. Eckert, M. Max von Laue and the discovery of X-ray diffraction in 1912. *Annalen der Physik* **524,** A83–A85 (2012).doi:https://doi.org/10.1002/andp.201200724

57. Takagi, S. Dynamical theory of diffraction applicable to crystals with any kind of small distortion. *Acta Crystallogr.* **15,** 1311–1312 (1962).doi:10.1107/S0365110X62003473

58. Takagi, S. A Dynamical Theory of Diffraction for a Distorted Crystal. *J. Phys. Soc. Japan* **26,** 1239–1253 (1969).doi:10.1143/JPSJ.26.1239

59. Taupin, D. Théorie dynamique de la diffraction des rayons X par les cristaux déformés. *Bull. Soc. Fr. Mineral. Cristallogr.* **87,** 469 (1964).

60. Pinsker, Z. *Dynamical Scattering of X-rays in Crystals* (Springer-Verlag, 1978).

61. Hofmann, S. *Auger-and X-ray photoelectron spectroscopy in materials science: a user-oriented guide* (Springer Science & Business Media, 2012).

62. Hüfner, S. *Photoelectron spectroscopy: principles and applications* (Springer Science & Business Media, 2013).

63. Fadley, C. X-ray photoelectron spectroscopy: Progress and perspectives. *Journal of Electron Spectroscopy and Related Phenomena* **178-179.** Trends in X-ray Photoelectron Spectroscopy of solids (theory, techniques and applications), 2–32 (2010).doi:https://doi.org/10.1016/j.elspec.2010.01.006

64. Bagus, P. S., Ilton, E. S. & Nelin, C. J. The interpretation of XPS spectra: Insights into materials properties. *Surface Science Reports* **68,** 273–304 (2013).doi:https://doi.org/10.1016/j.surfrep.2013.03.001

65. Powell, C. J. Improvements in the Reliability of X-ray Photoelectron Spectroscopy for Surface Analysis. *Journal of Chemical Education* **81,** 1734 (2004).doi:10.1021/ed081p1734

66. Steinhardt, R. & Serfass, E. X-Ray Photoelectron Spectrometer for Chemical Analysis. *Analytical Chemistry* **23,** 1585–1590 (1951).doi:10.1021/ac60059a019

67. Nordling, C., Sokolowski, E. & Siegbahn, K. Precision Method for Obtaining Absolute Values of Atomic Binding Energies. *Phys. Rev.* **105,** 1676–1677 (1957).doi:10.1103/PhysRev.105.1676

68. Wobrauschek, P., Kregsamer, P., Streli, C. & Aiginger, H. Recent Developments and Results in Total Reflection X-ray Fluorescence Analysis. *Advances in X-ray Analysis* **34,** 1–12 (1990).doi:10.1154/S0376030800014282

69. Castle, J. E. Practical surface analysis by Auger and X-ray photoelectron spectroscopy. D. Briggs and M. P. Seah (Editors). John Wiley and Sons Ltd, Chichester, 1983, 533 pp., £44.50. *Surface and Interface Analysis* **6,** 302–302 (1984).doi:https://doi.org/10.1002/sia.740060611

70. Birss, R. R. *Symmetry and Magnetism* 252 (North-Holland Pub. Co., 1966).

71. Torchinsky, D. H. & Hsieh, D. in *Magnetic Characterization Techniques for Nanomaterials* (ed Kumar, C. S.) 1–49 (Springer Berlin Heidelberg, Berlin, Heidelberg, 2017). doi:10.1007/978-3-662-52780-1_1.doi:10.1007/978-3-662-52780-1_1

72. Zhao, L., Torchinsky, D., Harter, J., de la Torre, A. & Hsieh, D. in *Encyclopedia of Modern Optics (Second Edition)* (eds Guenther, B. D. & Steel, D. G.) Second Edition, 207–226 (Elsevier, Oxford, 2018). doi:https://doi.org/10.1016/B978-0-12-803581-8.09533-3.doi:https://doi.org/10.1016/B978-0-12-803581-8.09533-3

73. Denev, S. A., Lummen, T. T. A., Barnes, E., Kumar, A. & Gopalan, V. Probing Ferroelectrics Using Optical Second Harmonic Generation. *Journal of the American Ceramic Society* **94,** 2699–2727 (2011).doi:https://doi.org/10.1111/j.1551-2916.2011.04740.x

74. Gallego, S. V., Etxebarria, J., Elcoro, L., Tasci, E. S. & Perez-Mato, J. M. Automatic calculation of symmetry-adapted tensors in magnetic and non-magnetic materials: a new tool of the Bilbao Crystallographic Server. *Acta Crystallographica Section A* **75,** 438–447 (2019).doi:10.1107/S2053273319001748

75. Maltezopoulos, T. *et al.* Operation of X-ray gas monitors at the European XFEL. *Journal of Synchrotron Radiation* **26,** 1045–1051 (2019).doi:10.1107/S1600577519003795

76. Mercurio, G. *et al.* Real-time spatial characterization of micrometer-sized X-ray free-electron laser beams focused by bendable mirrors. *Opt. Express* **30,** 20980–20998 (2022).doi:10.1364/OE.455948

77. Schneidmiller, E. A. & Yurkov, M. V. Photon beam properties at the European XFEL (December 2010 revision). *TESLA-FEL 2010-06,* 127 (2010).

78. Gerasimova, N. *et al.* The soft X-ray monochromator at the SASE3 beamline of the European XFEL: from design to operation. *J Synchrotron Rad* **29.** Publisher: International Union of Crystallography, 1299–1308 (2022).doi:10.1107/S1600577522007627

79. Balaraman, A. A. & Dutta, S. Inorganic dielectric materials for energy storage applications: a review. *Journal of Physics D: Applied Physics* **55,** 183002 (2022).doi:10.1088/1361-6463/ac46ed

80. Feng, M. *et al.* Recent Advances in Multilayer-Structure Dielectrics for Energy Storage Application. *Advanced Science* **8,** 2102221 (2021).doi:https://doi.org/10.1002/advs.202102221

81. Kholkin, A. L., Pertsev, N. A. & Goltsev, A. V. in *Piezoelectric and Acoustic Materials for Transducer Applications* (eds Safari, A. & Akdoğan, E. K.) 17–38 (Springer US, Boston, MA, 2008). doi:10.1007/978-0-387-76540-2_2.doi:10.1007/978-0-387-76540-2_2

82. Cohen, R. E. Origin of ferroelectricity in perovskite oxides. *Nature* **358,** 136–138 (1992).doi:10.1038/358136a0

83. Ihlefeld, J. F. in *Ferroelectricity in Doped Hafnium Oxide: Materials, Properties and Devices* (eds Schroeder, U., Hwang, C. S. & Funakubo, H.) 1–24 (Woodhead Publishing, 2019). doi:https://doi.org/10.1016/B978-0-08-102430-0.00001-2.doi:https://doi.org/10.1016/B978-0-08-102430-0.00001-2

84. Karvounis, A., Timpu, F., Vogler-Neuling, V. V., Savo, R. & Grange, R. Barium Titanate Nanostructures and Thin Films for Photonics. *Advanced Optical Materials* **8,** 2001249 (2020).doi:https://doi.org/10.1002/adom.202001249

85. Jahn, H. A., Teller, E. & Donnan, F. G. Stability of polyatomic molecules in degenerate electronic states - I-Orbital degeneracy. *Proceedings of the Royal Society of London. Series A - Mathematical and Physical Sciences* **161,** 220–235 (1937).doi:10.1098/rspa.1937.0142

86. Paillard, C., Torun, E., Wirtz, L., Íñiguez, J. & Bellaiche, L. Photoinduced Phase Transitions in Ferroelectrics. *Phys. Rev. Lett.* **123,** 087601 (2019).doi:10.1103/PhysRevLett.123.087601

87. Devonshire, A. XCVI. Theory of barium titanate. *The London, Edinburgh, and Dublin Philosophical Magazine and Journal of Science* **40,** 1040–1063 (1949).doi:10.1080/14786444908561372

88. Yamada, T. Electromechanical Properties of Oxygen-Octahedra Ferroelectric Crystals. *Journal of Applied Physics* **43,** 328–338 (1972).doi:10.1063/1.1661117

89. Berlincourt, D. & Jaffe, H. Elastic and Piezoelectric Coefficients of Single-Crystal Barium Titanate. *Phys. Rev.* **111,** 143–148 (1958).doi:10.1103/PhysRev.111.143

90. Vailionis, A. *et al.* Misfit strain accommodation in epitaxial ABO_3 perovskites: Lattice rotations and lattice modulations. *Phys. Rev. B* **83,** 064101 (2011).doi:10.1103/PhysRevB.83.064101

91. Kleibeuker, J. E. *et al.* Atomically defined rare earth scandate crystal surfaces. *Adv. Funct. Mater.* **20,** 3490–3496 (2010).doi:10.1002/adfm.201000889

92. Everhardt, A. *Novel phases in ferroelectric $BaTiO_3$ thin films: Enhanced piezoelectricity and low hysteresis* PhD thesis (University of Groningen, 2017).

93. Rijnders, G., Blank, D. H. A., Choi, J. & Eom, C.-B. Enhanced surface diffusion through termination conversion during epitaxial $SrRuO_3$ growth. *Appl. Phys. Lett..* **84,** 505–507 (2004).doi:10.1063/1.1640472

94. Shin, Y. J. *et al.* Oxygen Partial Pressure during Pulsed Laser Deposition: Deterministic Role on Thermodynamic Stability of Atomic Termination Sequence at $SrRuO_3/BaTiO_3$ Interface. *ACS Appl. Mater. Interfaces* **9,** 27305–27312 (2017).doi:10.1021/acsami.7b07813

95. Shin, Y. J. *et al.* Interface Control of Ferroelectricity in an $SrRuO_3/BaTiO_3/SrRuO_3$ Capacitor and its Critical Thickness. *Adv. Mater.* **29,** 1602795 (2017).doi:10.1002/adma.201602795

96. Parratt, L. G. Surface Studies of Solids by Total Reflection of X-Rays. *Phys. Rev.* **95,** 359–369 (1954).doi:10.1103/PhysRev.95.359

97. Als-Nielsen, J. & McMorrow, D. *Element of Modern X-Ray Physics* (John Wiley & Sons, Ltd, Chichester, 2001).

98. Pietsch Ullrich, 1., Holý Václav, 1. & Baumbach Tilo, 1. *High-resolution X-ray scattering : from thin films to lateral nanostructures* 2nd ed. doi:10.1007/978-1-4757-4050-9 (Springer, New York, 2004).doi:10.1007/978-1-4757-4050-9

99. Vignaud, G. *et al.* Ordering of diblock PS-PBMA thin films: An X-ray reflectivity study. *Phys. B: Condens. Matter* **248,** 250–257 (1998).doi:10.1016/S0921-4526(98)00243-9

100. Vartanyants, I. A. & Kovalchuk, M. V. Theory and applications of x-ray standing waves in real crystals. *Rep. Prog. Phys.* **64,** 1009 (2001).doi:10.1088/0034-4885/64/9/201

101. Fewster, P. F. X-ray diffraction from low-dimensional structures. *Semiconductor Science and Technology* **8,** 1915 (1993).doi:10.1088/0268-1242/8/11/001

102. Fewster, P. F. High-resolution diffraction-space mapping and topography. *Applied Physics A* **58,** 121–127 (1994).doi:10.1007/BF00324366

103. Birkholz, M. *Thin Film Analysis by X-Ray Scattering* (Wiley-VCH, Weinheim, 2005).

104. Van der Sluis, P., Binsma, J. J. M. & van Dongen, T. High resolution x-ray diffraction of periodic surface gratings. *Applied Physics Letters* **62,** 3186–3188 (1993).doi:10.1063/1.109124

105. Young, R. A. & Wiles, D. B. Profile shape functions in Rietveld refinements. *J. Appl. Crystallogr.* **15,** 430–438 (1982).doi:10.1107/S002188988201231X

106. Setter, N. *et al.* Ferroelectric thin films: Review of materials, properties, and applications. *J. Appl. Phys.* **100,** 051606 (2006).doi:10.1063/1.2336999

107. Jia, C. L. *et al.* Lattice strain and lattice expansion of the $SrRuO_3$ layers in $SrRuO_3/PbZr_{0.52}Ti_{0.48}O_3/SrRuO_3$ multilayer thin films. *J. Appl. Phys.* **92,** 101–105 (2002).doi:10.1063/1.1483369

108. Binnig, G., Quate, C. F. & Gerber, C. Atomic Force Microscope. *Phys. Rev. Lett.* **56,** 930–933 (1986).doi:10.1103/PhysRevLett.56.930

109. Butt, H.-J., Cappella, B. & Kappl, M. Force measurements with the atomic force microscope: Technique, interpretation and applications. *Surface Science Reports* **59,** 1–152 (2005).doi:https://doi.org/10.1016/j.surfrep.2005.08.003

110. Rodriguez, B. J., Callahan, C., Kalinin, S. V. & Proksch, R. Dual-frequency resonance-tracking atomic force microscopy. *Nanotechnology* **18,** 475504 (2007).doi:10.1088/0957-4484/18/47/475504

111. Yu, P. *et al.* Interface control of bulk ferroelectric polarization. *Proc. Natl. Acad. Sci.* **109,** 9710–9715 (2012).doi:10.1073/pnas.1117990109

112. De Luca, G. *et al.* Nanoscale design of polarization in ultrathin ferroelectric heterostructures. *Nat. Commun.* **8,** 1419 (2017).doi:10.1038/s41467-017-01620-2

113. Kim, H. J., Oh, S. H. & Jang, H. M. Thermodynamic theory of stress distribution in epitaxial $Pb(Zr,Ti)O_3$ thin films. *Appl. Phys. Lett.* **75,** 3195–3197 (1999).doi:10.1063/1.125275

114. Lichtensteiger, C. *InteractiveXRDFit* : a new tool to simulate and fit X-ray diffractograms of oxide thin films and heterostructures. *J. Appl. Crystallogr.* **51,** 1745–1751 (2018).doi:10.1107/S1600576718012840

115. Weymann, C. *et al.* Full Control of Polarization in Ferroelectric Thin Films Using Growth Temperature to Modulate Defects. *Adv. Electron. Mater.* **6,** 2000852 (2020).doi:10.1002/aelm.202000852

116. Wu, H. *et al.* Direct Observation of Large Atomic Polar Displacements in Epitaxial Barium Titanate Thin Films. *Adv. Mater. Interfaces* **7,** 2000555 (2020).doi:10.1002/admi.202000555

117. Borisevich, A. Y. *et al.* Suppression of Octahedral Tilts and Associated Changes in Electronic Properties at Epitaxial Oxide Heterostructure Interfaces. *Phys. Rev. Lett.* **105,** 087204 (2010).doi:10.1103/PhysRevLett.105.087204

118. Kim, Y.-M. *et al.* Direct observation of ferroelectric field effect and vacancy-controlled screening at the $BiFeO_3/La_xSr_{1-x}MnO_3$ interface. *Nat. Mater.* **13,** 1019–1025 (2014).doi:10.1038/nmat4058

119. Wang, J. L. *et al.* Chemistry and structure of $BaTiO_3$ ultra-thin films grown by different O_2 plasma power. *Chem. Phys. Lett.* **592,** 206–210 (2014).doi:10.1016/j.cplett.2013.12.030

120. Domingo, N. *et al.* Water adsorption, dissociation and oxidation on $SrTiO_3$ and ferroelectric surfaces revealed by ambient pressure X-ray photoelectron spectroscopy. *Phys. Chem. Chem. Phys.* **21,** 4920–4930 (2019).doi:10.1039/C8CP07632D

121. Spasojevic, I., Sauthier, G., Caicedo, J. M., Verdaguer, A. & Domingo, N. Oxidation processes at the surface of $BaTiO_3$ thin films under environmental conditions. *Appl. Surf. Sci.* **565,** 150288 (2021).doi:10.1016/j.apsusc.2021.150288

122. Deleuze, P.-M. *et al.* Nature of the Ba 4d Splitting in $BaTiO_3$ Unraveled by a Combined Experimental and Theoretical Study. *J. Phys. Chem. C* **126,** 15899–15906 (2022).doi:10.1021/acs.jpcc.2c02510

123. Landoulsi, J. *et al.* Organic adlayer on inorganic materials: XPS analysis selectivity to cope with adventitious contamination. *Appl. Surf. Sci.* **383,** 71–83 (2016).doi:10.1016/j.apsusc.2016.04.147

124. Geneste, G. & Dkhil, B. Adsorption and dissociation of H_2O on in-plane-polarized $BaTiO_3$ (001) surfaces and their relation to ferroelectricity. *Phys. Rev. B* **79,** 235420 (2009).doi:10.1103/PhysRevB.79.235420

125. Fadley, C. S. Angle-resolved x-ray photoelectron spectroscopy. *Prog. Surf. Sci.* **16,** 275–388 (1984).doi:10.1016/0079-6816(84)90001-7

126. Bedzyk, M. J. & Materlik, G. Two-beam dynamical diffraction solution of the phase problem: A determination with x-ray standing-wave fields. *Phys. Rev. B* **32,** 6456 (1985).

127. Zhang, F. *et al.* Correlations between polarization and structural information of supertetragonal $PbTiO_3$. *Phys. Rev. B* **105,** 024106 (2022).doi:10.1103/PhysRevB.105.024106

128. Abrahams, S. C., Kurtz, S. K. & Jamieson, P. B. Atomic Displacement Relationship to Curie Temperature and Spontaneous Polarization in Displacive Ferroelectrics. *Phys. Rev.* **172,** 551–553 (1968).doi:10.1103/PhysRev.172.551

129. Vartanyants, I., Lee, T.-L., Thiess, S. & Zegenhagen, J. Non-dipole effects in X-ray standing wave photoelectron spectroscopy experiments. *Nucl. Instrum. Methods Phys.* **547,** 196–207 (2005).doi:10.1016/j.nima.2005.05.025

130. Trzhaskovskaya, M., Nefedov, V. & Yarzhemsky, V. Photoelectron angular distribution parameters for elements Z=1 to Z=54 in the photoelectron energy range 100–5000 eV. *At. Data Nucl. Data Tables* **77,** 97–159 (2001).doi:https://doi.org/10.1006/adnd.2000.0849

131. Trzhaskovskaya, M., Nefedov, V. & Yarzhemsky, V. Photoelectron angular distribution parameters for elements Z=55 to Z=100 in the photoelectron energy range 100–5000 eV. *At. Data Nucl. Data Tables* **82,** 257–311 (2002).doi:https://doi.org/10.1006/adnd.2002.0886

132. Woodruff, D. P. & Bradshaw, A. M. Adsorbate structure determination on surfaces using photoelectron diffraction. *Reports on Progress in Physics* **57,** 1029 (1994).doi:10.1088/0034-4885/57/10/003

133. Vartanyantz, I. A., Kovalchuk, M. V. & Beresovsky, V. M. Theoretical investigations of secondary emission yield and standing waves in curved crystals under dynamical Bragg diffraction of X-rays (Taupin problem). *Journal of Physics D: Applied Physics* **26,** A197 (1993).doi:10.1088/0022-3727/26/4A/041

134. Wright, O. B. & Gusev, V. E. Acoustic generation in crystalline silicon with femtosecond optical pulses. *Applied Physics Letters* **66,** 1190–1192 (1995).doi:10.1063/1.113853

135. Grimaldi, M. G., Baeri, P. & Rimini, E. Laser-induced free-carrier absorption in Si single crystal. *Applied Physics A* **33,** 107–111 (1984).doi:10.1007/BF00617616

136. Akhmanov, S. A. & Gusev, V. É. Laser excitation of ultrashort acoustic pulses: New possibilities in solid-state spectroscopy, diagnostics of fast processes, and nonlinear acoustics. *Soviet Physics Uspekhi* **35,** 153 (1992).doi:10.1070/PU1992v035n03ABEH002221

137. Müller, A. & Härdtl, K. H. Ambipolar diffusion phenomena in $BaTiO_3$ and $SrTiO_3$. *Appl. Phys. A* **49,** 75–82 (1989).doi:10.1007/BF00615468

138. He, Y. Heat capacity, thermal conductivity, and thermal expansion of barium titanate-based ceramics. *Thermochimica Acta* **419,** 135–141 (2004).doi:10.1016/j.tca.2004.02.008

139. Yamanaka, S. *et al.* Thermophysical properties of SrHfO3 and $SrRuO_3$. *Journal of Solid State Chemistry* **177,** 3484–3489 (2004).doi:https://doi.org/10.1016/j.jssc.2004.05.039

140. Hidde, J., Guguschev, C., Ganschow, S. & Klimm, D. Thermal conductivity of rare-earth scandates in comparison to other oxidic substrate crystals. *Journal of Alloys and Compounds* **738,** 415–421 (2018).doi:https://doi.org/10.1016/j.jallcom.2017.12.172

141. Wang, Z., Yang, M. & Zhang, H. Strain engineering on electrocaloric effect in $PbTiO_3$ and $BaTiO_3$. *Adv Compos Hybrid Mater* **4,** 1239–1247 (2021).doi:10.1007/s42114-021-00257-6

142. De Ligny, D. & Richet, P. High-temperature heat capacity and thermal expansion of $SrTiO_3$ and $SrZrO_3$ perovskites. *Phys. Rev. B* **53,** 3013–3022 (1996).doi:10.1103/PhysRevB.53.3013

143. Guyot, F., Richet, P., Courtial, P. & Gillet, P. High-temperature heat capacity and phase transitions of $CaTiO_3$ perovskite. *Phys Chem Minerals* **20** (1993).doi:10.1007/BF00200116

144. Lin, Z., Zhigilei, L. V. & Celli, V. Electron-phonon coupling and electron heat capacity of metals under conditions of strong electron-phonon nonequilibrium. *Phys. Rev. B* **77,** 075133 (2008).doi:10.1103/PhysRevB.77.075133

145. Kittel, C. *Introduction to Solid State Physics* 8th ed. (Wiley, 2004).

146. National Institute of Standards and Technology (NIST). *NIST Reference on Constants, Units, and Uncertainty* https://physics.nist.gov/cuu/Constants/. Accessed: 2024-08-03. 2024.

147. *CRC Handbook of Chemistry and Physics* 104th (ed Rumble, J. R.) (CRC Press, 2023).

148. Chen, J., Hong, L., Huang, B. & Xiang, H. Ferroelectric switching assisted by laser illumination. *Phys. Rev. B* **109,** 094102 (2024).doi:10.1103/PhysRevB.109.094102

149. Chernova, E. *et al.* Strain-controlled optical absorption in epitaxial ferroelectric $BaTiO_3$ films. *Applied Physics Letters* **106** (2015).doi:10.1063/1.4921083

150. Fu, J. *et al.* Strain propagation in layered two-dimensional halide perovskites. *Science Advances* **8,** eabq1971 (2022).doi:10.1126/sciadv.abq1971

151. Gu, R. *et al.* Temporal and spatial tracking of ultrafast light-induced strain and polarization modulation in a ferroelectric thin film. *Science Advances* **9,** eadi1160 (2023).doi:10.1126/sciadv.adi1160

152. Mudiyanselage, R. R. H. H. *et al.* Coherent acoustic phonons and ultrafast carrier dynamics in hetero-epitaxial $BaTiO_3$–$BiFeO_3$ films and nanorods. *J. Mater. Chem. C* **7,** 14212–14222 (2019).doi:10.1039/C9TC01584A

153. Palik, E. D. & Prucha, E. J. *Handbook of optical constants of solids* (Academic Press, Boston, MA, 1997).

154. Jeong, J.-W., Shin, S.-C., Lyubchanskii, I. L. & Varyukhin, V. N. Strain-induced three-photon effects. *Phys. Rev. B* **62,** 13455–13463 (2000).doi:10.1103/PhysRevB.62.13455

155. Murgan, R., Tilley, D. R., Ishibashi, Y., Webb, J. F. & Osman, J. Calculation of nonlinear-susceptibility tensor components in ferroelectrics: cubic, tetragonal, and rhombohedral symmetries. *J. Opt. Soc. Am. B* **19,** 2007–2021 (2002).doi:10.1364/JOSAB.19.002007

156. Young, E. S. K., Akimov, A. V., Campion, R. P., Kent, A. J. & Gusev, V. Picosecond strain pulses generated by a supersonically expanding electron-hole plasma in GaAs. *Phys. Rev. B* **86,** 155207 (2012).doi:10.1103/PhysRevB.86.155207

157. Werdehausen, D. *et al.* Photo-excited dynamics in the excitonic insulator Ta_2NiSe_5. *Journal of Physics: Condensed Matter* **30,** 305602 (2018).doi:10.1088/1361-648X/aacd76

158. Fridkin, V. M. Bulk photovoltaic effect in noncentrosymmetric crystals. *Crystallography Reports* **46,** 654–658 (2001).doi:10.1134/1.1387133

159. Young, S. M. & Rappe, A. M. First Principles Calculation of the Shift Current Photovoltaic Effect in Ferroelectrics. *Phys. Rev. Lett.* **109,** 116601 (2012).doi:10.1103/PhysRevLett.109.116601

160. Koch, W. T. H., Munser, R., Ruppel, W. & Würfel, P. P. D. Anomalous photovoltage in $BaTiO_3$. *Ferroelectrics* **13,** 305–307 (1976).

161. Dai, Z., Schankler, A. M., Gao, L., Tan, L. Z. & Rappe, A. M. Phonon-Assisted Ballistic Current from First-Principles Calculations. *Phys. Rev. Lett.* **126,** 177403 (2021).doi:10.1103/PhysRevLett.126.177403

162. Daranciang, D. *et al.* Ultrafast Photovoltaic Response in Ferroelectric Nanolayers. *Phys. Rev. Lett.* **108,** 087601 (2012).doi:10.1103/PhysRevLett.108.087601

163. Nicoul, M., Shymanovich, U., Tarasevitch, A., von der Linde, D. & Sokolowski-Tinten, K. Picosecond acoustic response of a laser-heated gold-film studied with time-resolved x-ray diffraction. *Applied Physics Letters* **98,** 191902 (2011).doi:10.1063/1.3584864

164. Schick, D. *et al.* Following Strain-Induced Mosaicity Changes of Ferroelectric Thin Films by Ultrafast Reciprocal Space Mapping. *Phys. Rev. Lett.* **110,** 095502 (2013).doi:10.1103/PhysRevLett.110.095502

165. Schick, D. *et al.* Ultrafast lattice response of photoexcited thin films studied by X-ray diffraction. *Structural Dynamics* **1,** 064501 (2014).doi:10.1063/1.4901228

166. Schick, D. *et al.* Localized Excited Charge Carriers Generate Ultrafast Inhomogeneous Strain in the Multiferroic $BiFeO_3$. *Phys. Rev. Lett.* **112,** 097602 (2014).doi:10.1103/PhysRevLett.112.097602

167. Lee, H. J. *et al.* Structural Evidence for Ultrafast Polarization Rotation in Ferroelectric/Dielectric Superlattice Nanodomains. *Phys. Rev. X* **11,** 031031 (2021).doi:10.1103/PhysRevX.11.031031

168. Lee, H. J. *et al.* Subpicosecond Optical Stress Generation in Multiferroic $BiFeO_3$. *Nano Letters* **22,** 4294–4300 (2022).doi:10.1021/acs.nanolett.1c04831

169. Korff Schmising, C. v. *et al.* Coupled Ultrafast Lattice and Polarization Dynamics in Ferroelectric Nanolayers. *Phys. Rev. Lett.* **98,** 257601 (2007).doi:10.1103/PhysRevLett.98.257601

170. Sando, D. *et al.* Epitaxial ferroelectric oxide thin films for optical applications. *Applied Physics Reviews* **5,** 041108 (2018).doi:10.1063/1.5046559

171. Ron, A. *et al.* Transforming a strain-stabilized ferroelectric into an intrinsic polar metal with light. *Phys. Rev. B* **108,** 224308 (2023).doi:10.1103/PhysRevB.108.224308

172. Bedzyk, M. J. *et al.* Probing the polarity of ferroelectric thin films with x-ray standing waves. *Phys. Rev. B* **61,** R7873–R7876 (2000).doi:10.1103/PhysRevB.61.R7873

173. Kazimirov, A. *et al.* X-ray standing-wave analysis of the rare-earth atomic positions in $RBa_2Cu_3O_{7-\delta}$ thin films. *Solid State Commun.* **114,** 271–276 (2000).

174. Kazimirov, A. *et al.* X-ray Standing Waves in Epitaxial Thin Films. *Synchrotron Radiat. News* **17,** 17–23 (2004).doi:10.1080/08940880408603090

175. Spaldin, N. A. & Ramesh, R. Advances in magnetoelectric multiferroics. *Nat. Mater.* **18,** 203–212 (2019).doi:10.1038/s41563-018-0275-2

176. Maslen, E., Fox, A. G. & O'Keefe, M. A. *International tables for crystallography, Volume C* (International Union of Crystallography, Chester, 2006).

177. Henke, B., Gullikson, E. & Davis, J. X-Ray Interactions: Photoabsorption, Scattering, Transmission, and Reflection at E = 50-30,000 eV, Z = 1-92. *At. Data Nucl. Data Tables* **54,** 181–342 (1993).doi:https://doi.org/10.1006/adnd.1993.1013

178. Shinotsuka, H., Tanuma, S., Powell, C. J. & Penn, D. R. Calculations of electron inelastic mean free paths. XII. Data for 42 inorganic compounds over the 50 eV to 200 keV range with the full Penn algorithm. *Surf. Interface Anal.* **51,** 427–457 (2019).doi:https://doi.org/10.1002/sia.6598

179. Patnaik, P. *Handbook of Inorganic Chemicals* (McGraw-Hill, 2002).

180. Ahadi, K., Mahdavi, S.-M., Nemati, A., Tabesh, M. & Ranjbar, M. Electronic structure and morphological study of $BaTiO_3$ film grown by pulsed-laser deposition. *Mater. Lett.* **72,** 107–109 (2012).doi:https://doi.org/10.1016/j.matlet.2011.12.081

181. Löhl, F. *et al.* Electron Bunch Timing with Femtosecond Precision in a Superconducting Free-Electron Laser. *Phys. Rev. Lett.* **104.** Publisher: American Physical Society, 144801 (2010).doi:10.1103/PhysRevLett.104.144801

182. Czwalinna, M. *et al.* Beam Arrival Stability at the European XFEL. *Proceedings of the 12th International Particle Accelerator Conference* **IPAC2021,** 6 pages, 0.921 MB (2021).doi:10.18429/JACOW-IPAC2021-THXB02

183. Thompson, J. *et al.* Enhanced metallic properties of $SrRuO_3$ thin films via kinetically controlled pulsed laser epitaxy. *Applied Physics Letters* **109,** 161902 (2016).doi:10.1063/1.4964882

184. De Jong, M. *et al.* Charting the complete elastic properties of inorganic crystalline compounds. *Scientific Data* **2,** 150009 (2015).doi:10.1038/sdata.2015.9

185. Uecker, R. *et al.* Properties of rare-earth scandate single crystals (Re=Nd-Dy). *Journal of Crystal Growth* **310,** 2649–2658 (2008).doi:https://doi.org/10.1016/j.jcrysgro.2008.01.019

186. *Quantities, units, and symbols in physical chemistry* 2nd ed (eds Mills, I., International Union of Pure and Applied Chemistry & International Union of Pure and Applied Chemistry) (Blackwell Scientific Publications, 1993).

187. Biegalski, M. D. *et al.* Thermal expansion of the new perovskite substrates $DyScO_3$ and $GdScO_3$. *Journal of Materials Research* **20,** 952–958 (2005).doi:10.1557/JMR.2005.0126

188. *A Collection of Problems on the Equations of Mathematical Physics* (ed Vladimirov, V. S.) doi:10.1007/978-3-662-05558-8 (Springer Berlin Heidelberg, Berlin, Heidelberg, 1986).doi:10.1007/978-3-662-05558-8